Title
Westerly Jet and Seasonal Transitions of the East Asian Summer Monsoon

Author
Kong, Wenwen

Publication Date
2020

Peer reviewed|Thesis/dissertation

Westerly Jet and Seasonal Transitions of the East Asian Summer Monsoon

By

Wenwen Kong

A dissertation submitted in partial satisfaction of the

requirements for the degree of

Doctor of Philosophy

in

Geography

in the

Graduate Division

of the

University of California, Berkeley

Committee in charge:

Professor John C. H. Chiang, Chair
Professor Inez Y. Fung
Professor William R. Boos
Professor Kurt M. Cuffey

Summer 2020

Westerly Jet and Seasonal Transitions of the East Asian Summer Monsoon

Abstract

Westerly Jet and Seasonal Transitions of the East Asian Summer Monsoon

by

Wenwen Kong

Doctor of Philosophy in Geography

University of California, Berkeley

Professor John C. H. Chiang, Chair

This dissertation explores the dynamical linkage between the orographic forcing of the Tibetan Plateau on the westerlies, and the seasonal migration of the East Asian summer monsoonal rainfall.

Chapter 2 focuses on evolution of the East Asian summer monsoon (EASM) from early to late Holocene. The Holocene EASM was previously characterized as a trend toward weaker monsoon intensity paced by orbital insolation. It is demonstrated here that this evolution is more accurately characterized as changes in the transition timing and duration of the EASM seasonal stages (spring, pre-mei-yu, mei-yu, midsummer), and tied to the north–south displacement of the westerlies relative to Tibet. To this end, time-slice simulations across the Holocene are employed using an atmospheric general circulation model. Self-organizing maps are used to objectively identify the transition timing and duration of the EASM seasonal stages. Compared to the late Holocene, an earlier onset of mei-yu and an earlier transition from mei-yu to midsummer in the early to mid-Holocene are found, resulting in a shortened mei-yu and prolonged midsummer stage. These changes are accompanied by an earlier northward positioning of the westerlies relative to Tibet. Invoking changes to seasonal transitions also provides a more satisfactory explanation for two key observations of Holocene East Asian climate: the "asynchronous Holocene optimum" and changes to dust emissions. A mechanism is proposed to explain the altered EASM seasonality in the simulated early to mid-Holocene. The insolation increase over the boreal summer reduces the pole–equator temperature gradient, leading to northward-shifted and weakened westerlies. The meridional position of the westerlies relative to the Tibetan Plateau determines the onset of mei-yu and possibly the onset of the midsummer stage. The northward shift in the westerlies triggers earlier seasonal rainfall transitions and, in particular, a shorter mei-yu and longer midsummer stage.

Chapter 3 explores how the termination of the mei-yu is dynamically linked to the westerlies impinging on the Tibetan Plateau. It is found that the mei-yu stage terminates when the maximum upper-tropospheric westerlies shift beyond the northern edge of the plateau,

around 40° N. This termination is accompanied by the disappearance of tropospheric northerlies over northeastern China. The link between the transit of the jet axis across the northern edge of the plateau, the disappearance of northerlies, and termination of the mei-yu holds on a range of time scales from interannual through seasonal and pentad. Diagnostic analysis indicates that the weakening of the meridional moisture contrast and meridional wind convergence, mainly resulting from the disappearance of northerlies, causes the demise of the mei-yu front. We propose that the westerlies migrating north of the plateau and consequent weakening of the extratropical northerlies triggers the mei-yu termination. Model simulations are employed to test the causality between the jet and the orographic downstream northerlies by repositioning the northern edge of the plateau. As the plateau edge extends northward, orographic forcing on the westerlies strengthens, leading to persistent strong downstream northerlies and a prolonged mei-yu. Idealized simulations with a dry dynamical core further demonstrate the dynamical link between the weakening of orographically forced downstream northerlies with the positioning of the jet from south to north of the plateau. Changes in the magnitude of orographically forced stationary waves are proposed to explain why the downstream northerlies disappear when the jet axis migrates beyond the northern edge of the plateau.

Chapter 4 proposes an interpretation on the teleconnection between El Niño and East Asian early summer rainband. An intensification of East Asian rainfall usually occurs summers following El Niño. We propose that this teleconnection is mediated via the westerlies impinging on the Tibetan Plateau, through El Niño's control on tropical tropospheric temperature. This is distinct from previous studies that attribute the El Niño's influence to changes in the Western Pacific subtropical anticyclone. The warming in the eastern equatorial Pacific leads to uniform warming of the entire tropical troposphere, which sharpens the temperature gradient between the tropics and the subtropics and shifts the westerlies southward. The westerlies impinge over the Tibetan Plateau for longer and, through interaction with the topography, induce intense and persistent extratropical northerlies downstream of the plateau that in turn intensifies the East Asian rainband. The rainband has previously been shown to intensify in a similar manner in a warming climate, suggesting that the El Niño response provides an analog for future changes.

To my parents and my husband

Contents

List of Figures

List of Tables

Acknowledgments

The past seven years has been a fabulous journey in my life. I would not have achieved so far without the support, encouragement, and companion from my mentors, colleagues, family, and friends. They all have participated and witnessed my growth.

My greatest thanks go to my advisor, John Chiang. John has been extremely well-organized, responsive, patient, and caring during his mentoring. With his gentle push, support, and encouragement, John guided me through uncharted waters and helped me grow and mature as a scholar. He taught me to ask fundamental questions, to go deep, to write clearly and think for the readers, to have a sense of humor when things do not work out, and to be brave to work on problems that interest me. John always encourages me to explore independently in my next projects, and he showed me that good science could only be produced with persistence, creativity, and rigorous thinking. John also cares very much about my professional development, including sending me to meetings and summer schools and showing full support when I was teaching in Spring 2019 and applying for postdoctoral positions. Like family and friends, John offers candid advice when I am distracted and reminds me to take breaks and enjoy life. There are not enough words to express my gratitude. Thank you, John.

Thanks to my dissertation committee Inez Fung, Bill Boos, and Kurt Cuffey. Inez greatly influenced my scholarly growth and taste. Inez is very generous about spending time providing career advice to me and discussing science with me. Every chat with her inspires me because of her contagious passion and genuine interest in how the Earth System works. Inez, I will miss those group dinners in your house, and thank you for being a role model for life-long learning. Interacting with Bill deepened my understanding of the tropical meteorology, and joining his group meetings has been a delightful experience. Bill is also a careful reader of my work. He raised many interesting questions that inspired several discussions in the final chapter. Kurt encouraged me to explore teaching opportunities during graduate school. I appreciate Kurt's career advice and his emphasis on thinking beyond the dissertation and seeing the big picture.

Several role models outside Berkeley have also influenced and helped me. I gained more appreciation of the landscape-climate interactions since the Plateau summer school led by Peter Molnar and colleagues. I thank Peter for selflessly sharing his knowledge and for always writing informative emails to answer my questions. Thanks to David Battisti for his interest in my work and helpful conversations. Thanks to Lorenzo Polvani, Michela Biasutti,

Wei Cheng, and Dargan Frierson for their generous help and guidance during my fellowship applications.

I am grateful for all the faculty, postdoctoral scholars, and students in McCone that I have interacted with during my graduate school. Geographers have made my day to day life in McCone enjoyable. Special thanks to the staff of our department. Thanks to Nat (Natalia Vonnegut) and Marjorie for making the start of my life here so smooth. Thanks to Eron and Alicia for helping with my technical questions. Thanks to Dan for his infectious laugh and for creating a safe workplace. Thank Sarah, Bobby, and Josh for always being there to answer my questions.

Thanks to my past and current office mates: Yuwei, Andrew, Yoshi, Jelena, Leif, Alyssa, Johannes, Zhenning, Jinlin, Mike, Sol, and Pierre. Thanks also to members of Fung group and Boos group: David, Jesse, Jiabin, Meghan, Michail, Stephanie, Mark, Alex, Xiaojuan, Eren, Vishnu, Michael, Nandini, Quentin, and Marysa. Thank you all for your friendship and support. Special thanks to Jelena, who accompanied me through the most stressful period before my qualification exam. Thanks to Leif for collaborating on my first paper. Thanks to Mike for asking sharp questions during our weekly EASM meetings. Andrew, Jelena, and Mike provided valuable advice and proofreading during my postdoctoral application. I am always grateful for that.

My family has been a constant source of love and support. I am fortunate to be born and raised in a loving family. My parents always believe in me and encourage me to pursue higher education. They instilled in me the courage to face challenges and cultivated my ability to appreciate things. I attribute the original cultivation of my appreciation to nature to my older brother, who took me to many adventures in our hometown's rural area during childhood. Thanks to my brother and his family for their care and love while I am far from home. And I am very grateful that they and my parents are taking good care of each other. Thanks to my husband, Bo, for his unconditional love and encouragement along the journey. Bo always has faith in me, and he is very supportive of my academic career. Thank you for being the gentle breeze beneath my wings and the light of my life.

This dissertation was supported by the National Science Foundation Grant AGS-1405479 (funded to John Chiang), the Doctoral Completion Fellowship from the Berkeley Graduate Division, and departmental funds from the Department of Geography at Berkeley. This dissertation was typeset using the ucastrothesis LaTeX template.

Chapter 1

Introduction

1.1 Motivation

The term "monsoon" originates from the Arabic word "mausim" meaning season, which was used by seamen in the early days to describe the seasonal reversal of surface winds along the shores of the Indian Ocean and surrounding regions, in particular in the Arabian Sea (Dash, 2005). Early studies view the monsoon as a land-sea breeze like circulation driven by the thermal capacity contrast between land and ocean (Halley, 1687; Webster et al., 1998). Land heats up and cools down faster than the ocean, leading to differential heating of atmosphere over land and ocean, which creates horizontal pressure gradient and produces winds blowing from the ocean to the land during summer and vice versa during winter. The current consensus is that the monsoon broadly refers to peak rainfall season during summertime (Figure 1.1). Globally, the most prominent monsoonal system is the tropical rain belt, the so-called intertropical convergence zone (ITCZ). The marine ITCZ produces the majority of tropical oceanic precipitation, while the monsoon over land is considered a manifestation of seasonal migration of the ITCZ (Gadgil, 2003).

If we zoom in to the regional scale, each monsoon system is different in terms of the rainfall intensity, seasonal cycle, and circulation pattern. This dissertation reveals to the readers the intriguing dynamics of the East Asian summer monsoon (EASM). Motivated by a recent "jet transition hypothesis" (Chiang et al., 2015), the core question we aim to address is whether and how does the atmospheric westerly jet impinging on the Tibetan Plateau determines the timing and latitudinal position of the East Asian summer monsoonal precipitation. The following four sections briefly introduce the behavior of the EASM (section 1.2), previous mechanisms of the EASM (section 1.3), the hypothesis that motivated this work (section 1.4), and an overview of the ensuing chapters (section 1.5).

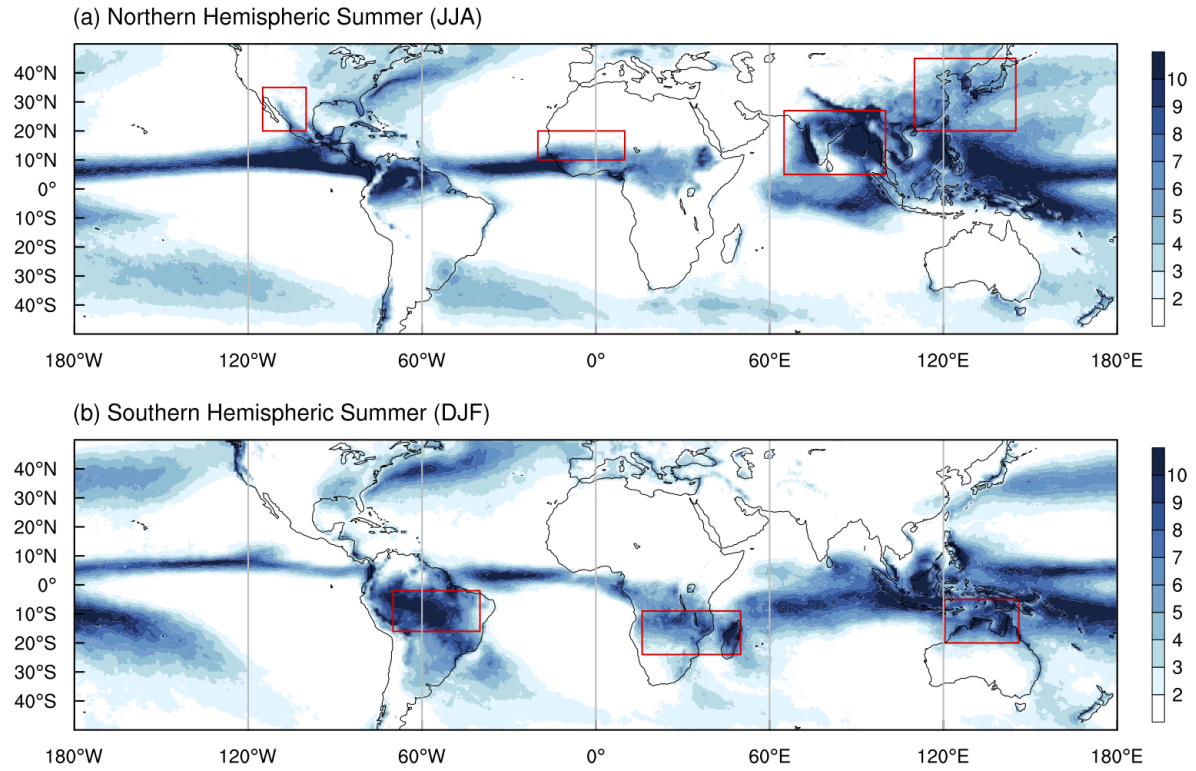

Figure 1.1: Precipitation in (a) June to August and (b) December to February (unit: $\mathrm{mm\,d^{-1}}$). Precipitation data is from the Tropical Rainfall Measuring Mission (TRMM) 3B42 (v7) (Huffman et al., 2007) averaged from 1998 to 2013. Red boxes highlight monsoonal areas of the North American monsoon over 20° to 35° N, 115° to 100° W (Douglas et al., 1993; Gutzler, 2004), the West African monsoon over 10° to 20° N, 20°W to 10°E (Janowiak, 1988), the South Asian monsoon over 5° to 27° N, 65° to 100° E (Wang & Fan, 1999), the East Asian monsoon over 20° to 45° N, 110° to 140° E (Ding & Chan, 2005), the South American monsoon over 16° to 2° S, 70° to 40° W (Gan et al., 2004), the East African monsoon over 24° to 9° S, 16° to 50° E (McHugh, 2004), and the Australian monsoon over 20° to 5° S, 120° to 146° E (Colman et al., 2011; Wang & Ding, 2008)

1.2 The phenomenon

The EASM is distinct from typical monsoons. Differing from most monsoon systems located in the tropics (Figures 1.2a-c), the EASM spans over the subtropics and the mid-latitudes. Its precipitation can penetrate inland as far as poleward of 40° N (Figure 1.2d).

This monsoon system is thus of hybrid nature of tropical and subtropical monsoon. Further, unlike typical monsoons such as the South Asian Monsoon and the West African Monsoon that experience smooth seasonal rainfall evolution, the EASM features abrupt northward jump of precipitation in the region (Figures 1.2d and 1.3a-d). One prominent feature of the East Asian summer monsoonal rainfall is a subtropical frontal rainband extending from central East China to the northwestern Pacific, Korean Peninsula, and Japan. This frontal rainband is termed the mei-yu in Chinese, the changma in Korean, and baiu in Japanese. Though regional disparities exist, the seasonal rainfall evolutions over each sector resemble each other (Figures 1.3e-h). This dissertation focuses specifically on the EASM over the mei-yu sector that affects summer rainfall in East China.

The seasonal transition of the EASM is characterized by a distinct northward rainfall migration, with two abrupt jumps and three stationary periods in between (Ding & Chan, 2005) (Figure 1.3). In climatology, the 'persistent spring rainfall' dominates southern East China in late spring (Wu et al., 2007). The first onset of the EASM, the 'pre mei-yu' stage, starts in early May when the precipitation over southern East China intensifies, and a frontal rainband starts to establish from south China to subtropical western Pacific. The rainband advances northward in mid-June, forming the Chinese mei-yu, the Korean changma, and the Japanese baiu. The second jump occurs in mid-July, creating the 'mid-summer' that features sporadic convective rainfall over northeastern China.

Variability of the EASM spans a wide range of timescales. Stable oxygen isotope records of speleothem calcium carbonate from Chinese caves provided valuable insight into the evolution of the EASM in the past climate (Wang et al., 2008b, 2001). Previous authors have viewed fluctuations in the $\delta^{18}O_p$ on paleoclimate timescales indicators of the summer rainfall intensity in East Asia: the lighter the isotope composition, the more intense the summer rainfall. Recent advances offered several alternative interpretations of the $\delta^{18}O_p$, such as the isotopic depletion via convection from the upstream region (Battisti et al., 2014; Pausata et al., 2011), the selection of the moisture source region (Maher, 2008), and the 'jet transition hypothesis' (Chiang et al., 2015, 2020) that motivated this dissertation. Though its interpretation is still in debate, the speleothem records in East Asia offered us a window to peep in the past and understand how a regional monsoonal system works under different climate forcings. In the present day, the EASM is known for its variability from interannual to decadal and inter-decadal timescales. The leading model of the interannual variation of the EASM exhibits a so-called 'tripole pattern' (Hsu & Lin, 2007), 2007). Changes of precipitation over central East China show a different sign from that in the north and south East China; when central East China is wetter, the north and south East China are drier, and vice versa. On decadal and interdecadal timescales, the EASM experienced evident regime changes during the late 1970s (Gong & Ho, 2002) and the 1990s (Kwon et al., 2007; Zhu et al., 2011). One notable phenomenon is the "north drought – south flood" pattern during the latter half of the twentieth century (Gong & Ho, 2002). Though not the focus of the dissertation, it is of great interest how the EASM will behave in a warming climate. Understanding the physical processes that drive the EASM is key to a reliable future projection.

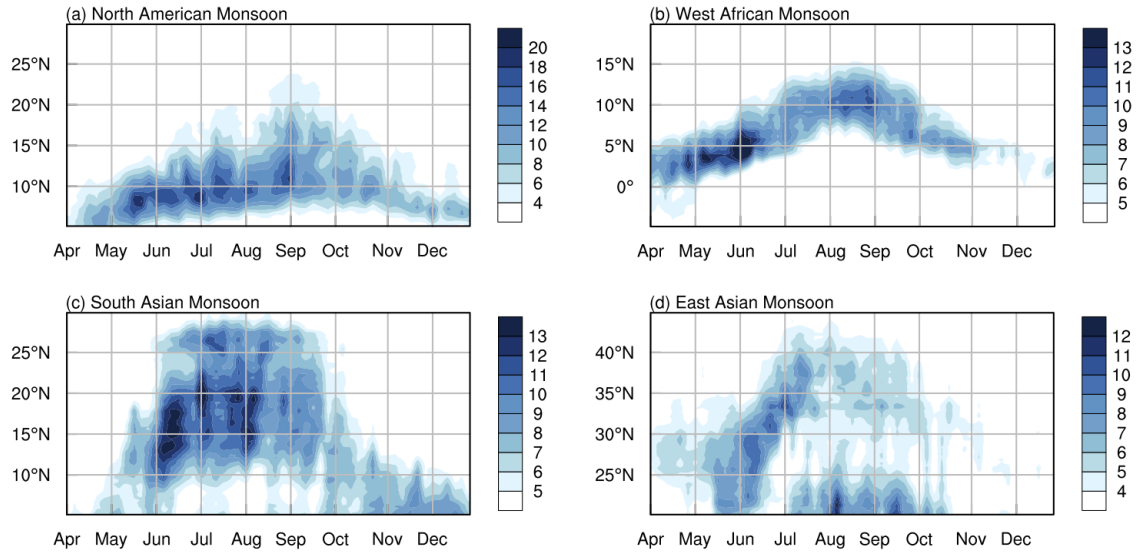

Figure 1.2: Hovmöller diagram of summer precipitation from the Northern Hemispheric monsoonal regions. (a) North American monsoon (averaged in 115° to 100° W), (b) West African monsoon (averaged in 20°W to 10°E), (c) South Asian monsoon (averaged in 65° to 100° E), and (d) East Asian monsoon (averaged in 110° to 145° E). Data is from the TRMM 3B42 (v7) from 1998 to 2013.

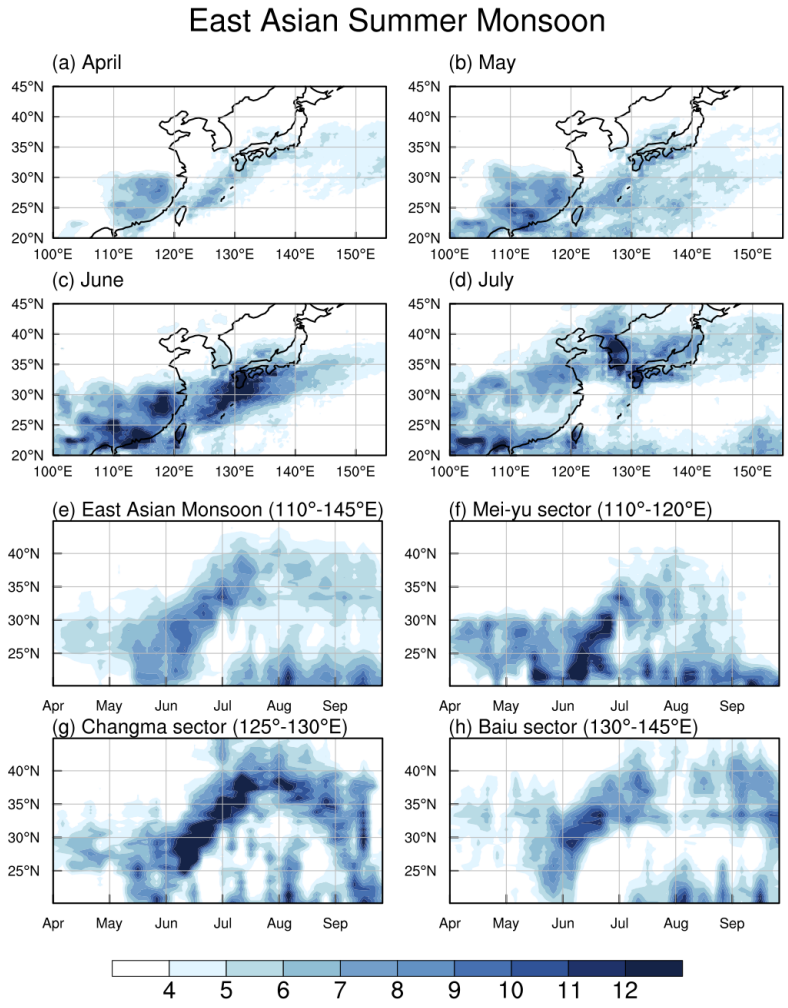

Figure 1.3: East Asian summer monsoon. (a)-(d) show seasonal evolution of the precipitation from April to July. (e)-(h) are hovmöller diagrams of precipitation averaged over different zonal bounds, (e) the whole East Asian domain from 110° to 145° E, (f) the mei-yu sector from 110° to 120° E, (g) the Changma sector from 125° to 130° E, and the Baiu sector from 130° to 145° E. Data is from the TRMM 3B42 (v7) from 1998 to 2013.

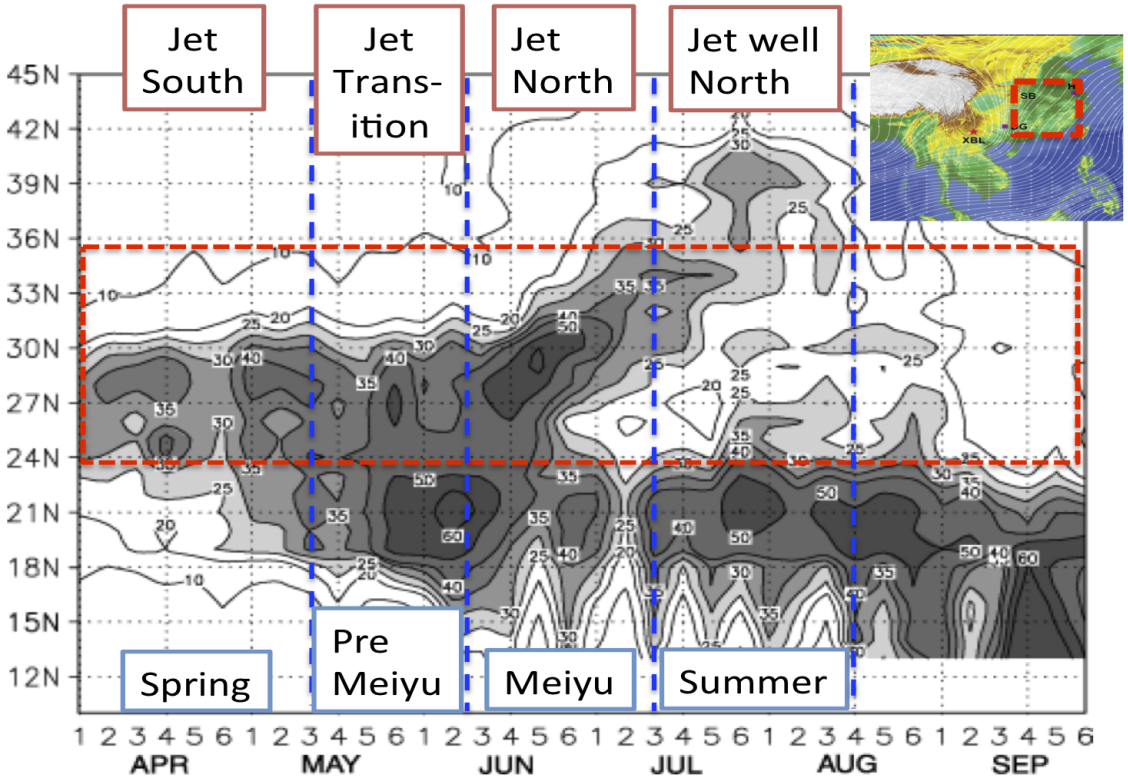

Figure 1.4: Latitude-time section of 5-day mean rainfall over eastern China (110° to 120° E, see inset) from April to September averaged for 1961-1990. Units of rainfall are mm, and regions of heavy rainfall (> 25 mm) are shaded. Also marked (blue dashed lines) are the stages in the rainfall and relationship to jet position. The red dashed line corresponds to latitudes shown in the map inset. Figure adapted from Chiang et al. (2015). Figure originally from Ding & Chan (2005), and identification of the rainfall stages and map inset were added by Chiang et al. (2015).

1.3 Previous hypotheses

Numerous processes have been proposed as the primary driver of the EASM. The conventional wisdom argues that it is the land-sea thermal contrast between the Asian continent and the Pacific Ocean that drives the onset and interannual variability of the EASM (Li & Yanai, 1996). The pressure gradient resulting from the thermal contrast drives a low-level southerly monsoonal flow from the South China Sea, penetrating inland and bringing precipitation. In a similar vein, the western Pacific subtropical high has long been thought of as a dominant factor that affects the EASM (Wang et al., 2013), as the anticyclonic circulation surrounding the subtropical high modulates the southerly monsoonal flow in East Asia. Previous studies suggest that the subtropical high act as a bridge that mediates the impacts of the tropical

ocean on the EASM. For example, some authors attribute the enhancement of East Asian summer rainfall following El Niño to an intensification of the western Pacific subtropical high, which is thought of as a response to the Indian Ocean warming that accompanies El Niño episodes (Xie et al., 2009). Anomalous convective activities over the Philippines Sea can also affect the EASM via modulating the subtropical high through the Pacific-Japan (PJ) pattern (Nitta, 1987). The PJ pattern suggests that the subtropical high intensifies when anomalously stronger convection occurs near the Philippines, and vice versa. This teleconnection is tied through Rossby waves, which is excited by the anomalous convective heating, that propagates from the tropics to mid-latitude (Kosaka & Nakamura, 2006, 2010).

Atmospheric waves propagating from the mid to high latitude also show a close connection to the East Asian summer rainfall. One notable example is the so-called Silk Road Pattern (Enomoto et al., 2003; Kosaka et al., 2009), an eastward propagating wave train across Eurasia during boreal summer. The current consensus is that the Silk Road Pattern is a stationary Rossby wave trapped in the Asian westerlies, and the latter act as an efficient waveguide (Hoskins & Ambrizzi, 1993). This wave train matters for the East Asian summer climate because the circulation pattern in the region varies with its phase changes. For instance, the Silk Road Pattern tends to present cyclonic anomalies over East Asia when the westerly jet is displaced southward (Hong & Lu, 2016). And the cyclonic circulation associated with the Silk Road Pattern is suggested to increase rainfall in the Yangtze River basin (Li & Lu, 2017). Mechanisms on the excitation and maintenance of the Silk Road Pattern are still in debate, and readers are referred to (Wang et al., 2017) for a comprehensive summary in their introduction section. Besides the quasi-stationary waves, transient eddies from the extratropics may play an essential role in strengthening monsoonal southerlies in East China (Park et al., 2015). In particular, Park et al. (2015) suggest that peak southerly winds usually develop a few days after an anomalous upper-tropospheric cyclone establishes in the region. They also argue that the baroclinic wave train propagating southeastward into East China causes quasi-geostrophic ascent and induces precipitation.

The Tibetan Plateau, a massive orographic landscape in Asia, also exert profound impacts on the EASM. Earlier studies placed the role of the plateau's elevated heating in the context of land-sea thermal contrast (Flohn, 1957; Li & Yanai, 1996). Subsequent studies suggest that the plateau's diabatic heating induces a low-level cyclonic wind around the plateau and drives southerlies to East Asia (Wu et al., 2007). Though the exact origin is still in debate (Boos & Kuang, 2010; Wu et al., 2012), the Tibetan Plateau is also argued to influence the EASM through the South Asian monsoon heating, which excites stationary eddies and induces monsoonal southerlies in East Asia (Liu et al., 2007; Wu et al., 2012). However, the dominant role of thermal forcing has been challenged recently (Son et al., 2019). In particular, the role of the mechanical interaction between the westerly jet and the plateau has been emerging in recent advances (Chen & Bordoni, 2014; Chiang et al., 2015; Molnar et al., 2010; Sampe & Xie, 2010). In the next section, I introduce the 'jet transition hypothesis' (Chiang et al., 2015) that motivated this dissertation, and advocate understanding the EASM via a perspective of its unique seasonality.

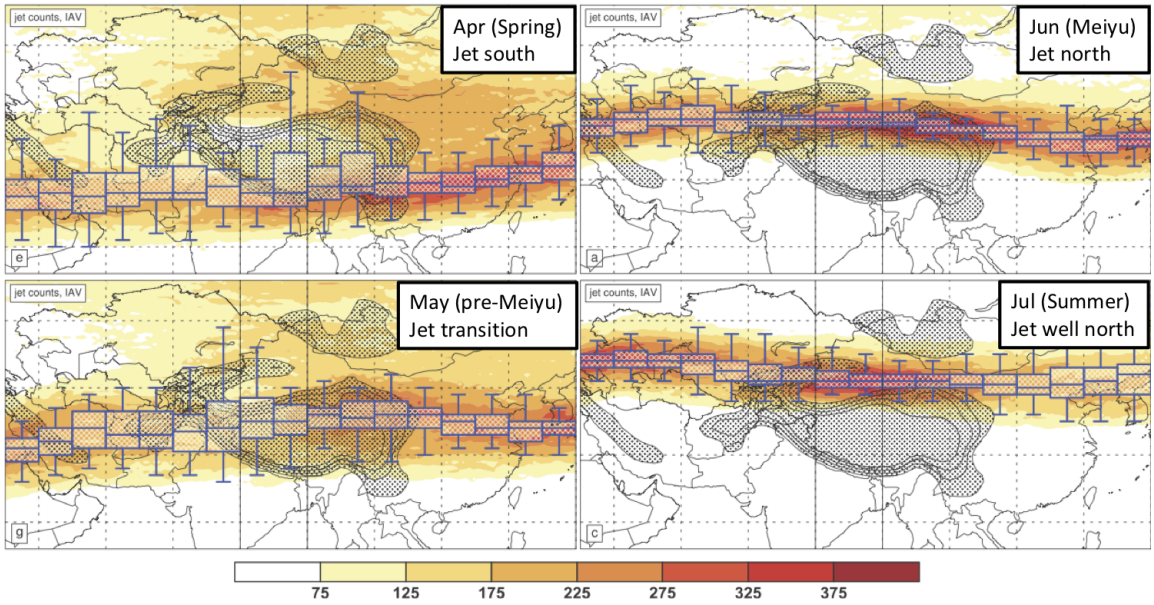

Figure 1.5: Seasonal transition of the westerly jet from south to north of the Plateau, and their association with the rainfall regimes over East Asia. Total jet occurrence counts (shaded) and interannual variability of jet latitude (boxes) for April to July as computed by Schiemann et al. (2009) from six-hourly ERA-40. A 'jet occurrence' is defined at a location if wind speed is a local maximum somewhere in the vertical column, that it exceeds $30\,\mathrm{m\,s^{-1}}$, and is westerly. Associated with each jet position is the particular rainfall regime, indicated by the text. Figure adapted from Chiang et al. (2015). Original figure is taken from Schiemann et al. (2009), and the identification of the rainfall stages is added by Chiang et al. (2015).

1.4 The jet transition hypothesis

The close connection between the East Asian summer rainfall and the westerly jet has long been documented (Staff Members of the Section of Synoptic and Dynamic Meteorology, 1957; Yeh et al., 1959). These pioneering studies showed that the winter to summer transition of East Asian climate is characterized by a northward shift of westerlies, accompanied by the mei-yu onset. However, a causal linkage between the seasonal jet transition and the seasonality received little attention until recently. Molnar et al. (2010) formulated that westerlies impinging on the Tibetan Plateau modulates East Asian summer rainfall through

mechanical interaction with the plateau. They suggest that the formation of the mei-yu rainband is due to orographic downstream large-scale convergence that results from the jet-orography interaction. In this view, the mei-yu rainband disappears when the westerly jet migrates to the north of the plateau. In a similar vein, Chiang et al. (2015) proposed to interpret past changes in East Asian summer climate via a "jet transition hypothesis": *changes to the seasonal meridional position of the westerlies relative to the Tibetan Plateau drive rainfall climate changes over East Asia on paleoclimate timescales.*

The synchronous relation between the latitudinal position of the westerly jet and East Asian summer precipitation provides observational evidence of the hypothesis (Figures 1.4 and 1.5). Schiemann et al. (2009) provides a detailed examination of the seasonal jet transition during the East Asian summer monsoon. In climatology, the westerly jet locates to the south of the Tibetan Plateau in April. The jet starts migrating northward to the Tibetan Plateau in May, corresponding to the pre-mei-yu season. The mei-yu onsets over central East China when the jet reaches the plateau's northern edge in June. The mei-yu transition to the midsummer occurs in July as the jet migrates well north of the plateau. Thus, the 'jet transition hypothesis' predicts that the timing and length of the EASM rainfall stages are paced by the positioning of the westerly jet relative to the Tibetan Plateau. If proven true, we can use the response in the latitudes of westerlies under various climate scenarios as predictors of changes in the EASM.

1.5 An overview

In the ensuing chapters, we explore the "jet transition hypothesis" from three angles. Chapter 2 tests the hypothesis in the evolution of the EASM from the early to the late Holocene. Chapter 3 explores the dynamical linkage between the mei-yu termination and the northward migration of westerlies off the Tibetan Plateau. Chapter 4 proposes an interpretation of the teleconnection between the El Niño and the mei-yu through the westerlies. The final chapter summarizes the main findings and suggests future directions to further our understanding of the EASM.

Chapter 2

Seasonal transitions and the westerly jet in the Holocene East Asian Summer Monsoon

2.1 Introduction

Unlike other major monsoon systems (such as the West African monsoon and the North American monsoon), the East Asian summer monsoon (EASM) undergoes unique meridional transitions during its seasonal evolution (Lau, 1988; Tao & Chen, 1987) characterized by three quasi-stationary stages and two abrupt jumps between them (Ding & Chan, 2005). In their review article, Ding & Chan (2005) suggested that the onset process of the EASM can be summarized as follows: 1) Following the "spring persistent rainfall" (Wu et al., 2007), the first onset starts in early May, which we label as the "pre-mei-yu" season. 2) The rainfall band then advances northward in mid-June, forming the Chinese mei-yu, the Korean changma, and the Japanese baiu. 3) The second jump occurs around mid-July, bringing more rainfall over northern China, which we label as "midsummer rainfall" following Xu & Zipser (2010). The conventional interpretation of the EASM seasonal evolution is that the land–sea thermal contrast caused by the differential heat capacities of the Asian continent and the Pacific Ocean induces a pressure contrast, which in turn drives a low-level monsoonal flow from the South China Sea that penetrates inland, bringing moisture and thus rainfall. This mechanism is thought to contribute to the onset and interannual variability of the EASM (e.g., Li & Yanai (1996)). The thermal and mechanical effects of the Tibetan Plateau are also thought to play important roles in the EASM evolution (Molnar et al., 2010; Yanai & Wu, 2006).

Previous work provided a basis to link the seasonal migration of the modern EASM and that of the mid- latitude westerlies impinging on the Tibetan Plateau. The meridional migration of the westerlies relative to Tibet follows the seasonal cycle of the insolation and its effect on the meridional temperature gradient, consistent with the thermal wind relationship. The advance of the westerly jet over East Asia was first tied to the downstream

northward transition of the rainfall belt over China in the English literature in the 1950s (Staff Members of the Section of Synoptic and Dynamic Meteorology, 1957, 1958a,b; Yeh et al., 1959). Subsequent studies have further supported the synchronous connection between the westerlies shift in the Tibetan region and the seasonal transitions of the EASM. For example, Schiemann et al. (2009) show that the position of the westerly jet impinging on the Tibetan Plateau is systematically correlated to the spatial distribution of precipitation over East Asia: the climatological westerly jet stays to the south of the Tibetan Plateau in April and migrates onto the Tibetan Plateau in May, corresponding to the pre-mei-yu season; the jet reaches the northern edge of the Tibetan Plateau in June timed to the start of the mei-yu season; the northernmost jet position is achieved in July to August, timed with the mid-summer rainfall season; and finally, the jet retreats southward and the East Asian monsoonal rainfall declines in September.

This synchronous relationship points to a strong dynamical control of the westerlies on EASM seasonality (e.g., (Liang & Wang, 1998; Sampe & Xie, 2010)); however, a comprehensive and dynamically consistent interpretation of how this comes about is still lacking. Sampe & Xie (2010) suggest that the westerlies advect warm air downstream that then rises due to adiabatic uplift, thus providing a favorable environment for convection; the uplift is further intensified from the resulting latent heat release during condensation. They also highlight the role of the westerlies in anchoring the mei-yu rainfall band via steering the weather disturbances along the jet. Chen & Bordoni (2014) confirm that the westerly jet induces low-level downstream convergence through providing horizontal advection of dry enthalpy, and argue that the meridional stationary eddy activity is crucial in sustaining the mei-yu front via transporting the mean temperature meridionally.

Paleoclimate reconstructions suggest that the intensity of the EASM varied considerably during the late Quaternary. Oxygen isotope records ($\delta^{18}O_c$) from Chinese caves suggest that the EASM during the Holocene changes in pace with orbital forcing on the precessional scales; that is, stronger Northern Hemisphere summer insolation induces enhanced EASM in the early to mid-Holocene (Wang et al., 2001, 2008b). Based on the "amount effect" (Dansgaard, 1964), this interpretation views the values of $\delta^{18}O_c$ recorded in the caves as a measure of EASM intensity (Wang et al., 2005). In agreement with the paleo-proxy records, climate model simulations also suggest an intensified EASM during the mid-Holocene (e.g., (Zheng et al., 2013)). For example, the PMIP3 models median suggests that the summer precipitation over eastern China increases by 6.57% on average in the mid-Holocene simulations (Zheng et al., 2013).

Given that today's EASM seasonal evolution is nontrivial, describing the early to mid-Holocene EASM as simply "more intense" is clearly incomplete. A recent modeling study (Shi, 2016) argues for changes to the monsoon duration in the orbital-scale variability of EASM. Their results suggest that, under interglacial conditions, the length of rainy season over northern East Asia (33° to 40° N, 105° to 130° E) is longer for precession maxima (weaker boreal summer insolation) than for precession minima (stronger boreal summer insolation). Chiang et al. (2015) postulated that the defining characteristic of EASM changes in past climates is in the timing and duration of the EASM seasonal stages, rather than

intensity. They furthermore invoke the dynamical link between the westerlies and the seasonal transition: their so-called jet transition hypothesis argues that the altered timing in the meridional migration of the westerlies relative to Tibet led to changes in the seasonal transition of the EASM in the past climate. They argue that the seasonality perspective can more consistently explain the varieties of existing proxy evidences of the East Asian paleoclimate changes, including speleothem, dust, and pollen records.

Following Chiang et al. (2015), this study explores orbitally induced EASM changes across the Holocene from the viewpoints of seasonality and the westerly jet. We simulate the orbitally induced Holocene changes to the EASM using "time snapshot" simulations of an atmospheric general circulation model (coupled to a slab ocean) that simulates the present-day EASM seasonal stages with fidelity. A novel feature of our analysis will be the use of "self-organizing maps" (SOMs) to objectively identify the spatial pattern and timing of the EASM seasonal stages from the model rainfall simulations. We analyze the simulations to address two questions: 1) How does the timing, duration, and seasonal transition of the EASM change across the Holocene? 2) What factors are these changes in seasonality attributable to? For the first question, we show that orbitally driven EASM of the early to mid-Holocene is characterized by an advanced rainfall seasonality, with earlier mei-yu onset and an earlier transition from mei-yu to midsummer rainfall; this results in a shortened mei-yu rainfall stage and prolonged midsummer rainfall stage. For the second question, we show that the advanced seasonality is attributable to an earlier northward shift of the East Asian westerlies in the early to mid-Holocene compared to the present.

This chapter proceeds as follows. Section 2.2 describes the data, experiments, and the self-organizing maps. Section 2.3 presents the identification of the EASM seasonal stages from the SOMs. Section 2.4 presents our analysis of the simulated East Asian summer climates at various snapshots across the Holocene. Section 2.5 discusses the dynamical linkage between the westerlies and the seasonality of the EASM. Section 2.6 compares our results against two key paleoproxy observations of the Holocene East Asian climate, namely, the "asynchronous Holocene optimum" interpretation (An et al., 2000) and the dust proxy record, and shows that our seasonality interpretation is consistent with these observations. Conclusions and discussion are given in section 2.7.

2.2 Data, experiments, and method

2.2.1 Data

We use the APHRODITE rain gauge data (Yatagai et al., 2009) for the self-organizing maps (SOMs) analysis of the EASM rainfall patterns. APHRODITE data are also used to present the seasonal transitions of today's EASM (Figure 2.1). The APHRO_MA_025deg_V1003R1 product covers 57 years (1951–2007) of daily precipitation on $0.25° \times 0.25°$ grid within 15° S–55° N, 60°–150° E. This product has better quality control, incorporates more data, and has had bugs corrected when compared with the previous version APHRO_MA_

V0902 (Yatagai et al., 2009). The gridded data only include rainfall values over land and are generated by interpolating rain gauge observations obtained from meteorological and hydrological stations over the region. The uncertainties of the APHRODITE lie in the discrepancies in the ending time for 24-h precipitation accumulation between countries, and the fact that the rain gauge network changes in region and time (Yatagai et al., 2012). Han & Zhou (2012) compared the APHRO_MA_025deg_V1003R1 product with daily precipitation obtained from 559 rain gauges with rigorous quality control in contiguous China. Compared with the station data, APHRODITE presents bias in both rainfall intensity and frequency; on the other hand, APHRODITE is able to precisely capture the seasonal transition of the rain belt and the long-term trend of precipitation amount over China (Han & Zhou, 2012).

2.2.2 Experiments

Seven sets of numerical experiments are conducted using the E_1850_CAM5 component set from the National Center for Atmospheric Research's (NCAR) Community Earth System Model (CESM) version 1.2.2 (Hurrell et al., 2013), which includes the coupler, active atmosphere, land, and ice components, and a static slab ocean. The atmospheric component of the CESM1 is the Community Atmosphere Model version 5 (CAM5) at $0.9\,\mathrm{h} \times 1.25\,\mathrm{h}$ to orizontal resolution and 30 layers of vertical resolution. The ocean heat transport convergence (i.e., the "Q flux") from a CESM1 preindustrial fully coupled run (available on the Yellowstone high-performance IBM cluster at NCAR) is prescribed to the slab ocean model to achieve a simulated sea surface temperature close to the preindustrial.

We apply the CAM5 to seven time periods—9000 years before present (9ka hereafter), 7.5, 6, 4.5, 3, 1.5 ka, and preindustrial (PI)—and the insolation at the top of atmosphere is prescribed for each time segment by specifying the corresponding year, and the model computes the corresponding eccentricity, obliquity, and precession (Berger et al., 1993). The GHG concentrations in our PI simulation are set to default values as in the CESM preindustrial configuration (i.e., CO_2 is 284.7 ppm, CH_4 is 791.6 ppb, and N_2O is 275.68 ppb). Following the Paleoclimate Modeling Intercomparison Project phase 3 (PMIP3) protocol (Braconnot et al., 2012), we prescribe the atmospheric content of CH_4 at 650 ppb in the 9-, 7.5-, 6-, 4.5-, 3-, and 1.5-ka experiments, while keeping CO_2 and N_2O fixed at their values for the PI. Land surface type is kept to the same as for the pre-industrial control. Each experiment is integrated for 60 years, with the first 30 years treated as spinup; the climatology derived over the last 30 years is used for the analysis presented. We use the Student's t test to present the statistical significance of the difference in the climatological means, with the null hypothesis that the anomaly is not significantly different from zero. To this end, we make the assumption that the samples used in calculating the statistical significance at each grid point are drawn from a Gaussian distribution (i.e., normally distributed) and independent of each other.

2.2.3 Self-organizing maps

Our problem requires accurate and objective identification of the seasonal EASM rainfall stages. Given that they exhibit unique spatial characteristics, and the transitions between them are abrupt, a cluster analysis is ideally suited for this analysis. The SOMs method is a neural network–based cluster analysis that classifies a high-dimensional dataset into representative patterns (Kohonen, 2001; Kohonen et al., 1996). It uses a neighborhood function to topologically order the high-dimensional input, grouping similar clusters together. The SOMs method has advantages over the empirical orthogonal function (EOF) technique in extracting nonlinear features (Iskandar, 2009; Liu et al., 2006). In addition, the SOMs method distinguishes itself from other clustering analyses, such as the k-means method (Lin & Chen, 2006) and Ward's method (Bao & Wallace, 2015; Solidoro et al., 2007), via extracting more distinctive and more robust representative patterns. Unlike EOFs, however, there is no straightforward way to reconstruct the dataset from the patterns derived from the SOMs (Liu et al., 2006). The SOMs method has been used successfully to characterize patterns of climate variations such as El Niño–Southern Oscillation (Johnson et al., 2013) and the Northern and Southern Hemisphere teleconnection patterns (Chang & Johnson, 2015; Johnson et al., 2008). This approach was first applied in the Asian monsoon by Chattopadhyay et al. (2008) for the intraseasonal oscillation of the Indian summer monsoon and has been applied to demonstrate the intraseasonal modes of the East Asian–western North Pacific summer monsoon (Chu et al., 2012). In this study, we use the SOMs to identify the distinct phases of rainfall during the seasonal transitions of the EASM.

We first applied the SOMs to the APHRODITE daily climatology during 1951–2007. We chose 20° to 45° N, 110° to 140° E (Wang & LinHo, 2002) as the domain for the EASM. Only data over land were used and each grid box was weighted by the cosine of latitude. We took the 5-day running mean of this latitude-weighted daily climatology and chose the summer half year (April–September) for the SOMs analysis. Following Johnson et al. (2013), we use the Epanechicov neighborhood function and the batch training algorithm in the present analysis. We did a statistical distinguishability test as in Johnson et al. (2013) and specified the number of nodes (K) to be 5 to match the number of expected rainfall patterns.

To test whether our simulations capture the seasonal stages of the EASM in a realistic way, we proceed to repeat the SOMs analysis of the APHRODITE dataset in the PI simulation. Note that we took the 7-day running mean of the daily rainfall climatology for the SOMs analysis in the PI simulation. We then match the 30-yr daily rainfall climatology from the remaining simulations to the SOMs patterns of the PI run. Each daily rainfall field is assigned to a best-matching SOMs pattern based on the minimum Euclidean distance.

For further specifics of the SOMs technique, the readers are referred to Johnson et al. (2013) and the appendix of Johnson et al. (2008).

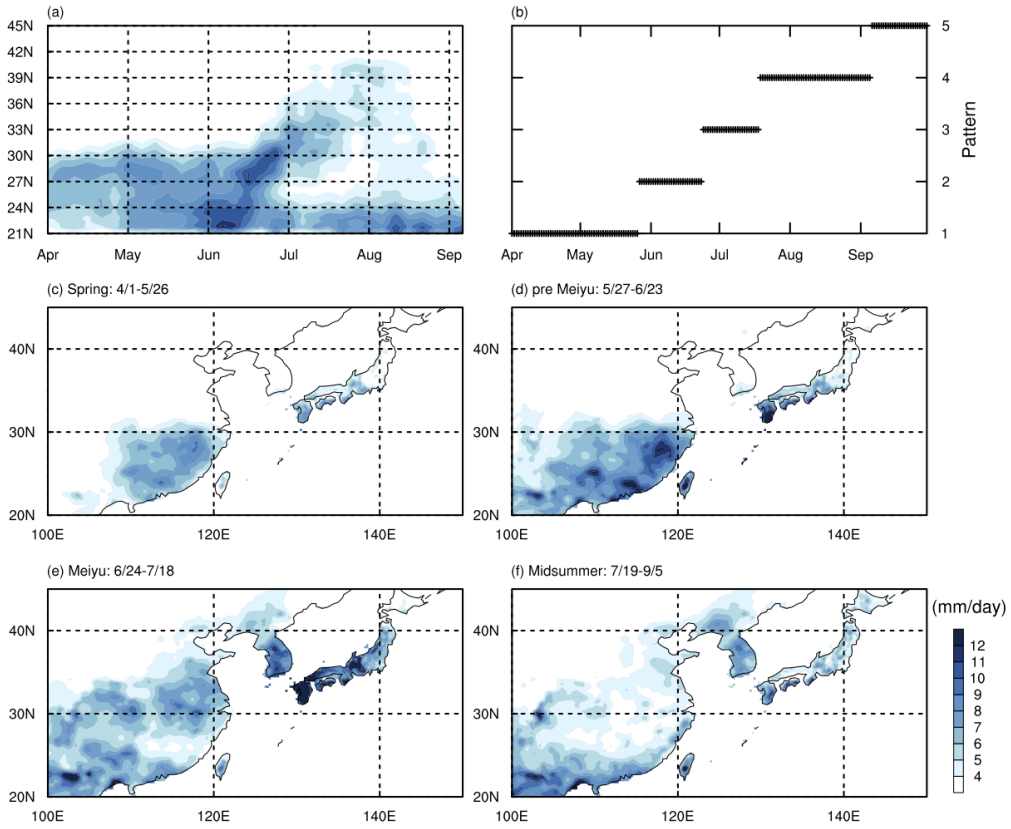

Figure 2.1: Climatology of the 1951–2007 APHRODITE daily precipitation rate (unit: $\mathrm{mm\,d^{-1}}$) over East Asia. (a) Hovmöller diagram of precipitation rate averaged from 110° to 120° E. Also shown are the (b) temporal and (c)–(f) spatial patterns of rainfall based on the SOMs analysis of the APHRODITE dataset: pattern 1 denotes the spring persistent rainfall (1 Apr–26 May) in (c), pattern 2 denotes the pre-mei- yu (27 May–23 Jun) in (d), pattern 3 denotes the mei-yu (24 Jun–18 Jul) in (e), and pattern 4 denotes the midsummer (19 Jul–5 Sep) in (f).

2.3 Identification of the EASM seasonal stages from SOMs analysis

In this section, we show that the SOMs analysis is able to objectively extract the seasonal stages of the EASM in observed precipitation data, and we furthermore show that the CAM5 is capable of simulating the EASM seasonal stages.

Figure 2.1a shows the latitude–time cross section of precipitation over eastern China

(110° to 120° E), reflecting the onset process of the EASM as summarized in Ding & Chan (2005): 1) Following the spring persistent rainfall (Wu et al., 2007), the pre-mei-yu season starts from the first 10-day period of May and features a steep rise in precipitation between 18° and 25° N. 2) The rain belt shifts to the valley of the Yangtze River in mid-June, the traditional Chinese mei-yu season. 3) From mid-July, the second jump of the rain belt brings more rainfall over northern and northeastern China, forming the midsummer rainfall season. 4) The southward retreat of the monsoon rain belt from the end of August to early September indicates the end of the EASM.

Largely in agreement with Ding & Chan (2005), SOMs analysis of the APHRODITE data (Figs. 2.1b–f) extracts the seasonal stages and transitions of the EASM accurately. Figure 2.1b presents the temporal rainfall patterns, here called "spring" (pattern 1), "pre-mei-yu" (pattern 2), "mei-yu" (pattern 3) and "midsummer" rainfall (pattern 4), during the seasonal transitions. Pattern 5 denotes the end of the EASM. Figures 2.1c–f present the spatial maps of the spring (Fig. 2.1c), pre-mei-yu (Fig. 2.1d), mei-yu (Fig. 2.1e), and midsummer (Fig. 2.1f) patterns based on the SOMs analysis. These results show that the SOMs method is able to distinctly extract the seasonal stages of the EASM, including both the spatial pattern and the timing and duration of each rainfall stage. We note that the onset timing of the pre-mei-yu and mei-yu stages from the APHRODITE SOMs is slightly delayed compared to Ding & Chan (2005): instead of early May and mid-June as in Ding & Chan (2005), here the pre-mei-yu starts in late May and the mei-yu in late June in our SOMs analysis. This difference may be due to the fact that the precipitation data and the time range used in our SOMs analysis are different from those in Ding & Chan (2005).

We now show that CAM5 can reasonably simulate the seasonal stages of the EASM. First, the Hovmöller diagram of the precipitation over eastern China (110° to 120° E) from the PI simulation (Fig. 2.2a) clearly captures the stepwise northward transition of the EASM rain belt, resembling today's rain gauge data (Fig. 2.1a). Second, by employing the SOMs method in the PI simulation, Figs. 2.2b–f suggest that the seasonality of the EASM simulated in CAM5 is largely consistent with that in the APHRODITE data (Figs. 2.1b–f). Besides the slight shift in the onset timing compared to the APHRODITE, the largest biases in the simulation come from the spatial pattern of each stage. For example, the position of the spring (Fig. 2.2c) and pre-mei-yu (Fig. 2.2d) patterns are northward shifted compared to APHRODITE (Figs. 2.1c,d). Although bias does exist, the CAM5 clearly simulates the seasonal transitions of the EASM with reasonable fidelity.

In the next two sections, we will show our analysis of the simulated Holocene EASM in CAM5 on the basis of the SOMs method.

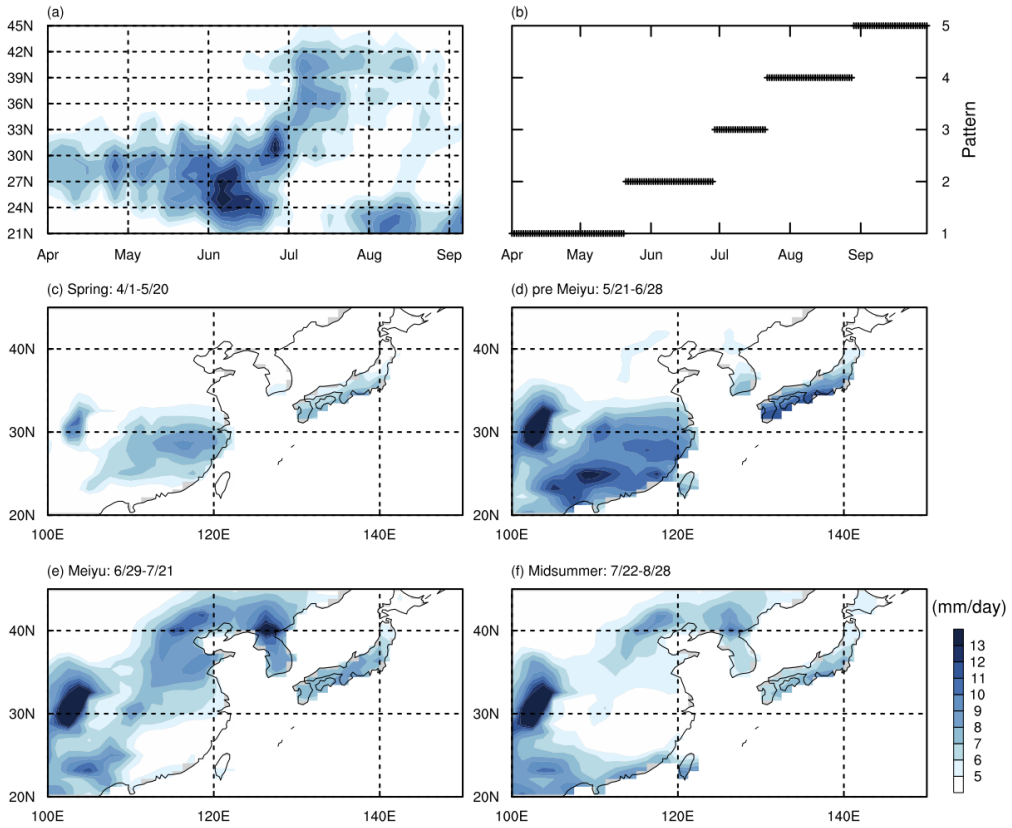

Figure 2.2: The East Asian summer monsoon from the preindustrial simulation in CAM5. (a) Hovmöller diagram of the precipitation averaged between 110° and 120° E. (b) The SOMs temporal patterns. (c)–(f) The SOMs spatial patterns averaged over the periods indicated, respectively: pattern 1 (spring; 1 April–20 May 20), pattern 2 (pre-mei-yu; 21 May–28 June), pattern 3 (mei-yu; 29 June–21 July), and pattern 4 (midsummer, 22 July–28 August).

Table 2.1: Statistics of mei-yu and midsummer rainfall in the Holocene simulations.

Simulation	Mei-yu onset	Mei-yu duration	Midsummer onset	Midsummer duration
PI	29 Jun	23 days	22 Jul	38 days
1.5 ka	25 Jun	25 days	20 Jul	54 days
3 ka	25 Jun	17 days	12 Jul	56 days
4.5 ka	24 Jun	15 days	9 Jul	63 days
6 ka	23 Jun	16 days	9 Jul	66 days
7.5 ka	19 Jun	9 days	28 Jun	79 days
9 ka	12 Jun	13 days	25 Jun	81 days

2.4 Changes to the EASM seasonality over the Holocene

The SOMs analysis provides an objective method to extract the seasonal stages of the EASM. In this section, we use this method on the Holocene simulations to show that the simulated EASM experiences gradually delayed seasonal transitions across the Holocene. We further- more show that the meridional positioning of the west- erlies shifts gradually southward across the Holocene, consistent with its hypothesized role in determining the timing of the EASM seasonal transitions.

2.4.1 General results

Table 2.1 and Fig. 2.3 (the visualization of Table 2.1) show the onset timing and length (on the average basis) of the mei-yu and midsummer derived from the SOMs analysis across the simulated Holocene. The onset of mei-yu and midsummer delays gradually from the early to the late Holocene. For example, the onset of mei-yu in 9 ka, on 12 June, is two weeks earlier than that in PI, which is on 29 June. Similarly, the onset of midsummer in 9ka, which is on 25 June, starts about one month earlier than that in PI. In addition, Table 2.1 shows that the early to mid-Holocene features shorter mei-yu duration and longer midsummer duration compared to the late Holocene. For instance, the duration of mei-yu in PI (23 days) is about twice as long as that in 9 ka (13 days), and the duration of midsummer in PI (38 days) is less than half of that in 9 ka (81 days).

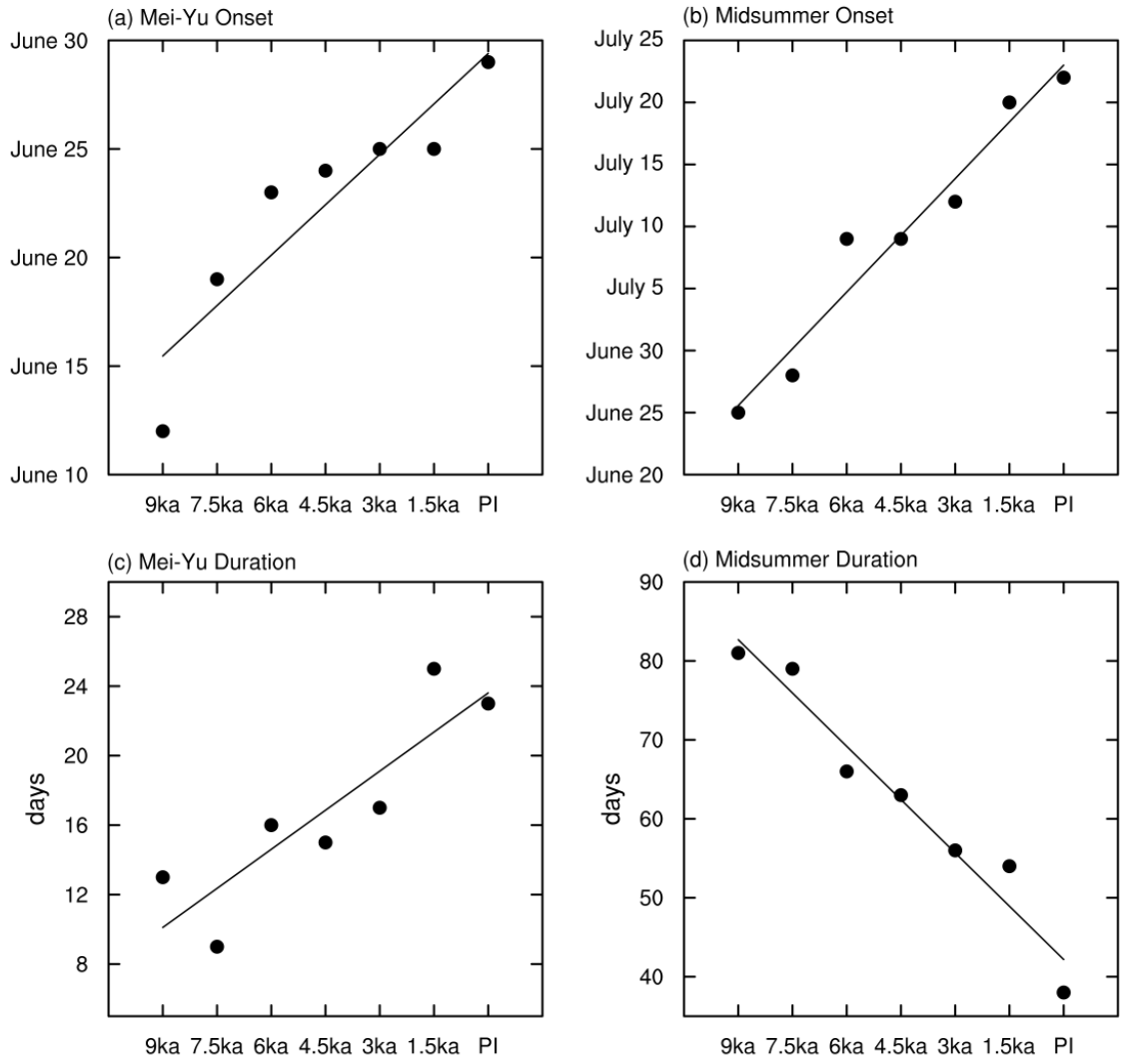

Figure 2.3: (a),(b) Onset timing and (c),(d) duration of the mei-yu and midsummer rainfall patterns, respectively, across the Holocene. The result of PI is based on the SOMs analysis, and the results of the rest simulations are derived by matching to the SOMs patterns of PI. The solid lines indicate the best-fit linear least squares regression based on the results.

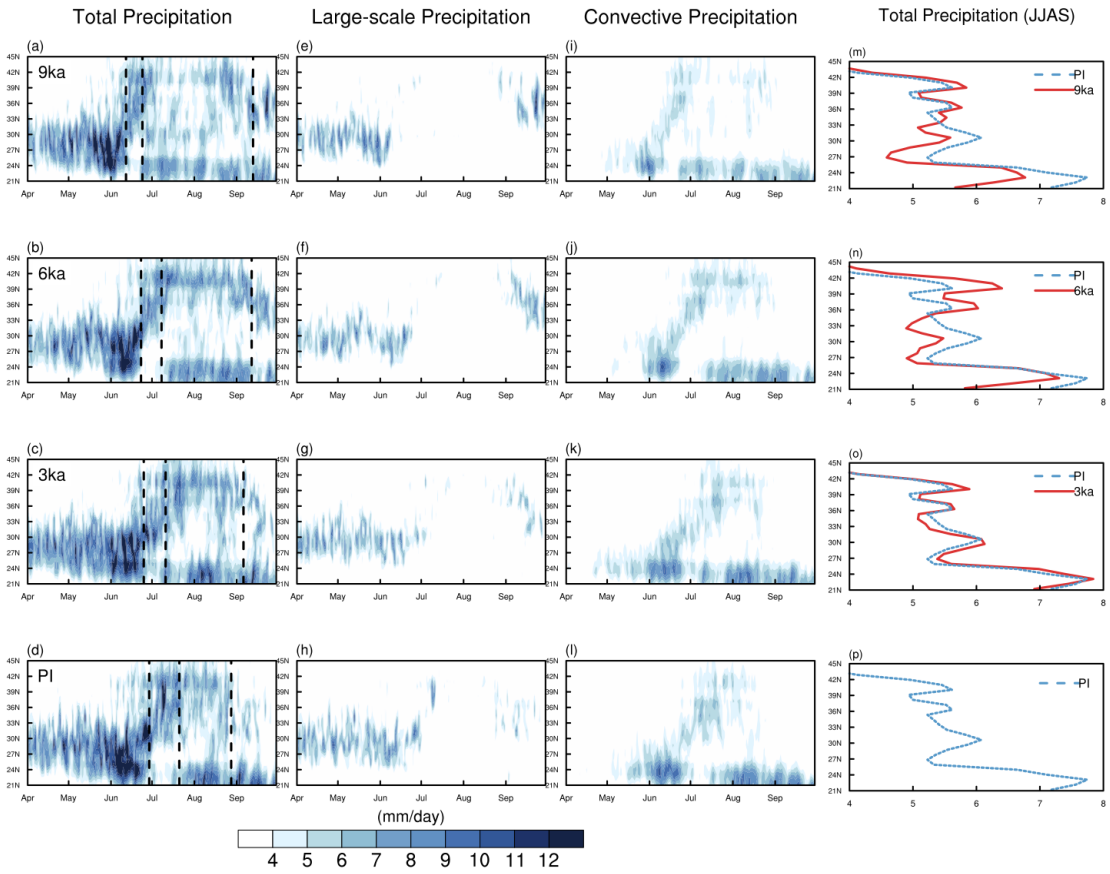

Figure 2.4: Seasonal transition of (a)–(d) total, (e)–(h) large-scale, and (i)–(l) convective precipitation rate, and (m)–(p) the averaged total precipitation (110° to 120° E) in June–September, in (from top to bottom) the 9-, 6-, 3-ka, and PI simulations, averaging from 110° to 120° E. Vertical dashed lines in (a)-(d) indicate timings of (from left to right) the mei-yu onset, the mei-yu termination (the midsummer onset), and the midsummer termination. The x axis in (m)-(p) indicates the strength of the rainfall. The blue dashed line denotes the results from PI, while the red solid lines denote the results from the 9-, 6-, and 3-ka runs. The unit is mm d^{-1}.

Figure 2.4 shows the temporal evolution of EASM seasonality in the 9-, 6-, 3-ka, and PI simulations, using a zonal average of the daily rainfall climatology over 110° to 120° E. Consistent with Fig. 2.3, Fig. 2.4 depicts a gradual shift of timing in the total rainfall transition from 9 ka to PI, suggesting that the seasonal transition of the EASM occurs earlier in 9 and 6 ka relative to 3 ka and PI. The evolution becomes particularly notable when we separate the total precipitation into the large-scale precipitation (Figs. 2.4e–h) and convective precipitation (Figs. 2.4i–l). Large-scale precipitation is characteristic of the rainfall over southern China during the spring and pre-mei-yu (Figs. 2.4e–h), whereas

convective precipitation dominates the mei-yu and midsummer rainfall seasons (Figs. 2.4i–l). The changes in the large-scale and convective rainfall are consistent with our hypothesis that the spring and pre-mei-yu are shortened during the early to mid-Holocene, and that the onset of mei-yu and midsummer appears earlier. Compared to 3 ka and PI, the 9- and 6-ka experience shorter mei-yu duration and longer midsummer duration. The common interpretation of the early Holocene EASM is that it is more "intense" (e.g., (Wang et al., 2008b)). It begs the question of how this relates to our finding that the seasonal transitions occur earlier. To evaluate summer monsoon "intensity" in the simulations, the fourth column in Fig. 2.4 shows the averaged total precipitation (110° to 120° E) over the entire summer rainfall period including June, July, August, and September. The notable aspect of this seasonally averaged picture is that whereas the rainfall over northern China (north of 36° N) is stronger in the early to mid-Holocene, the rainfall over southern China (south of 36° N) is actually weaker, in particular during the 6-ka period. Thus, describing the early to mid-Holocene EASM as being more intense clearly does not capture this regional heterogeneity in the rainfall response. Rather, the seasonality perspective—a shorter mei-yu and longer midsummer stage—provides a more accurate picture of the early to mid-Holocene rainfall changes over eastern China.

Unlike the 6 and 9 ka, the 3 ka does not show evident advance in the timing of the seasonal transitions compared to PI. This may be attributable to the nature of the insolation changes between those periods. For 9 and 6 ka, the increased summer insolation anomalies occur at the beginning of April for 9 ka and May for 6 ka (Fig. 2.5), which is sufficiently early to affect the transitions to the mei-yu and midsummer regimes. For 3 ka, however, the positive insolation anomalies only start in June.

To further elucidate the difference of the EASM between the early to mid-Holocene and the late Holocene, we will subsequently focus our analysis to the 6 ka compared against the PI. Based on the timing of the rainfall seasonal transitions in PI (Table 2.1), we define 29 June–21 July as the PI mei-yu and 22 July–28 August as the PI midsummer rainfall season. Similarly, we define 23 June–8 July as the 6-ka mei-yu season and 9 July–12 September as the 6-ka midsummer rainfall season.

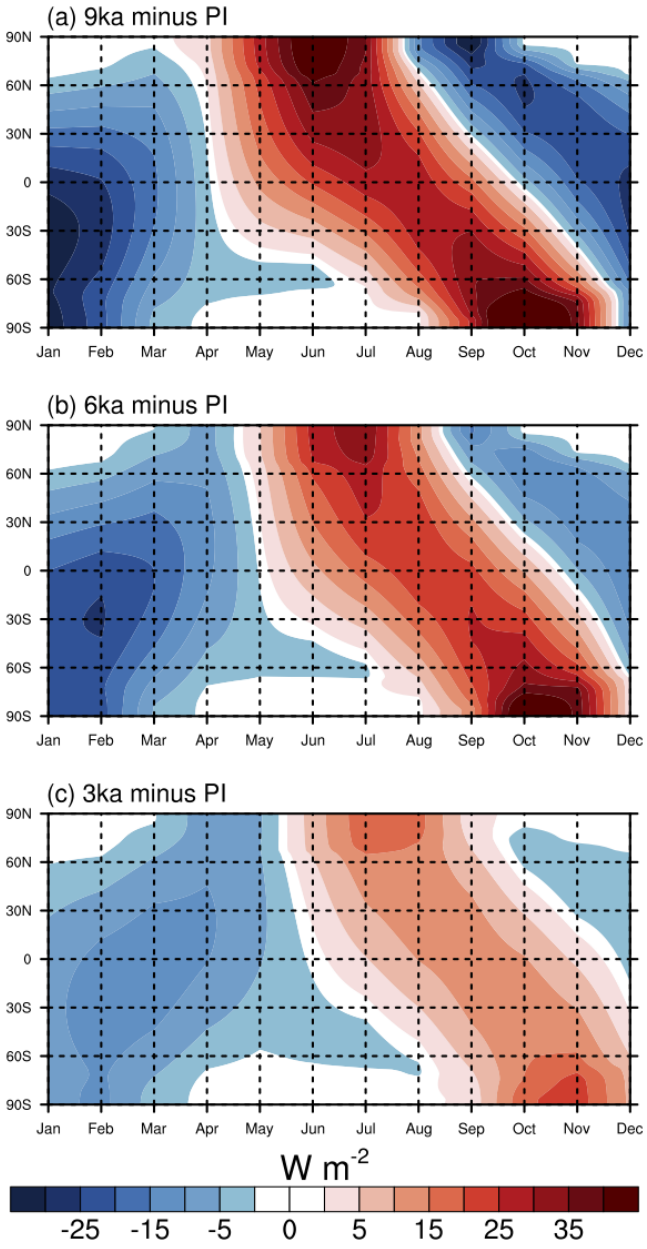

Figure 2.5: Insolation difference at the top of the atmosphere for (a) 9 ka and PI, (b) 6 ka and PI, and (c) 3ka and PI. The unit is watt/m^2.

2.4.2 Changes to the EASM frontal position and moisture transports and convergence

To confirm our interpretation (thus far based only on rainfall changes) that the onset of the mei-yu and mid-summer periods in 6 ka appears earlier, we examine the mei-yu

frontal position and associated moisture transports. The mei-yu front is characterized by a steep meridional gradient in equivalent potential temperature (θ_e) across northern China (Ninomiya, 1984; Tomita et al., 2011). Here we use the maximum in the meridional gradient of moist static energy (MSE) [$\frac{-\partial(MSE)}{\partial y}$] to approximately indicate this position (Fig. 2.6). The MSE is given by

$$MSE = C_p T + L_v q + gz,$$

where C_p is the specific heat at constant pressure ($1004\,\mathrm{J\,kg^{-1}\,K^{-1}}$), T is the temperature (K), g is the gravitational constant ($9.81\,\mathrm{m\,s^{-2}}$), z is the geopotential height (m), L_v is the latent heat of vaporization ($2.5 \times 10^6\,\mathrm{J\,kg^{-1}}$), and q is the specific humidity ($\mathrm{kg\,kg^{-1}}$). In the PI mei-yu phase (29 June–21 July), the front is located around 30° to 40° N (Fig. 2.6b). During 29 June–1 July in 6 ka, the front is located around 40° to 50° N (Fig. 2.6a). Also, there is a decrease in the MSE gradient in 30° to 40° N and an increase to the north of 45° N (Fig. 2.6c), suggesting an earlier northward shift of the frontal systems in 6ka and therefore earlier mei-yu onset. In the PI midsummer rainfall season (22 July–28 August), the front is weakened and moves to northern China (Fig. 2.6e); the front during the same time at 6ka shifts farther poleward (Fig. 2.6f), suggesting the early termination of mei-yu season and early onset of the midsummer rainfall. The moisture flux at 850 mb is shown in Fig. 2.7. The simulations demonstrate that during 6 ka there is stronger low-level monsoonal flow delivering more moisture to central to northern China in the PI mei-yu phase (Fig. 2.7c) and to northern China in the PI midsummer rainfall phase (Fig. 2.7f). Together, the northward frontal shift and increased low-level moisture transport suggest an earlier seasonal transition from pre-mei-yu to mei-yu and from mei-yu to midsummer rainfall in 6 ka.

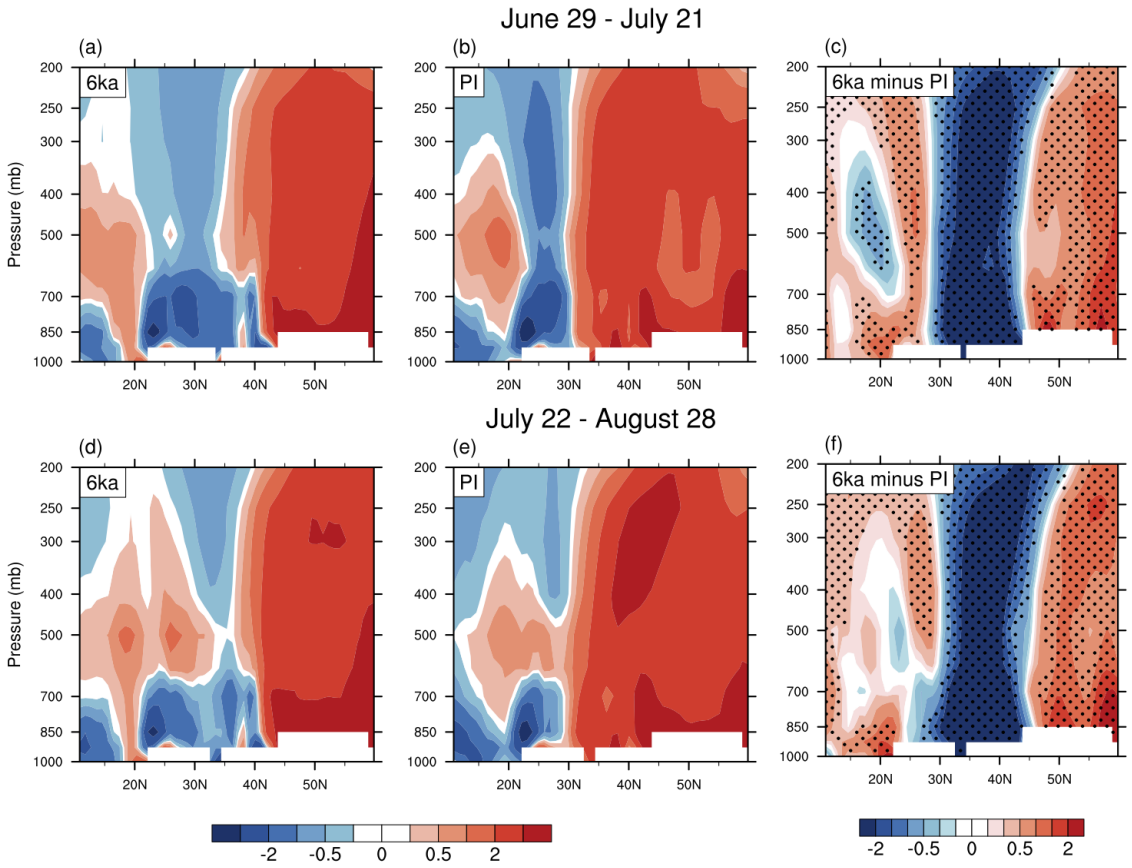

Figure 2.6: Pressure–latitude (10° to 60° N) cross section of the meridional gradient of MSE $[\frac{-\partial(MSE)}{\partial y}]$ averaged over 110° to 120° E, for (top) 29 Jun–21 Jul (i.e., the mei-yu season in PI) and (bottom) 22 Jul–28 Aug (i.e., the midsummer season in PI), for (left) 6 ka, (middle) PI, and (right) 6 ka minus PI. The stippled areas indicate that the difference is statistically significant at the confidence level of 90 %. The unit is $3 \times 10^{-6}\,\mathrm{kJ^2\,kg^{-1}\,m^{-1}}$.

Our interpretation is further corroborated by the changes in the relative vorticity ($\zeta = \frac{\partial v}{\partial x} - \frac{\partial u}{\partial y}$) and moisture convergence ($-\nabla \cdot (\mathbf{v}q) = -[\frac{\partial(uq)}{\partial x} + \frac{\partial(vq)}{\partial y}]$) at 850 mb (Fig. 2.8). As shown in Chen et al. (1998), high cyclonic vorticity is associated with convective rainstorms along the mei-yu front. The ascending motion generated by strong latent heat release stretches the local troposphere air mass vertically and creates the low-level convergence, which combines the low-level horizontal wind shear associated with the low-level jet, to force the rapid spinup of low-level vorticity [see Fig. 20 of Chen et al. (1998)]. Our simulation suggests that the high cyclonic vorticity zone is displaced northward from PI to 6 ka, which can be seen in both the periods of the PI mei-yu (Fig. 2.8c) and PI mid-summer rainfall

seasons (Fig. 2.8f). In addition, the 6-ka moisture convergence is enhanced to the north of 40° N (Figs. 2.8c,f), which likely results from the combined effect of the ascending motion along the northward-displaced frontal systems (Figs. 2.6c,f) as well as the enhanced poleward moisture supplies (Figs. 2.7c,f).

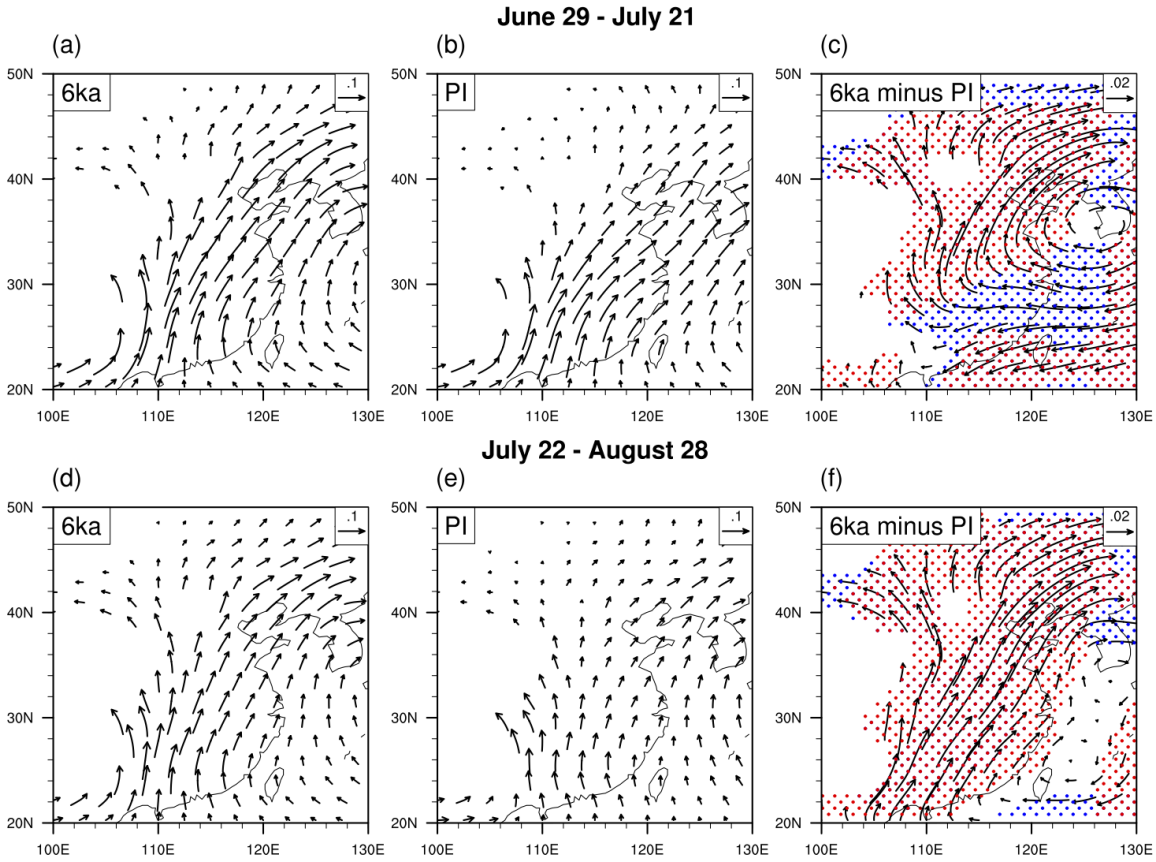

Figure 2.7: Moisture flux (vectors) at 850 mb for (top) 29 Jun–21 Jul (i.e., the mei-yu season in PI) and (bottom) 22 Jul–28 Aug (i.e., the midsummer season in PI), for (left) 6 ka, (middle) PI, and (right) 6 ka minus PI. The blue (red) dots indicate that the difference in zonal moisture flux ($\mathbf{u}q$) [meridional moisture flux ($\mathbf{v}q$)] is statistically significant at the confidence level of 90 %. [The unit is $10^3\,\mathrm{g\,kg^{-2}\,m^{-1}\,s^{-1}}$, and the reference vector is $0.1 \times 10^3\,\mathrm{g\,kg^{-2}\,m^{-1}\,s^{-1}}$ in (a),(b),(d), and (e) and $0.02 \times 10^3\,\mathrm{g\,kg^{-2}\,m^{-1}\,s^{-1}}$ in (c) and (f).

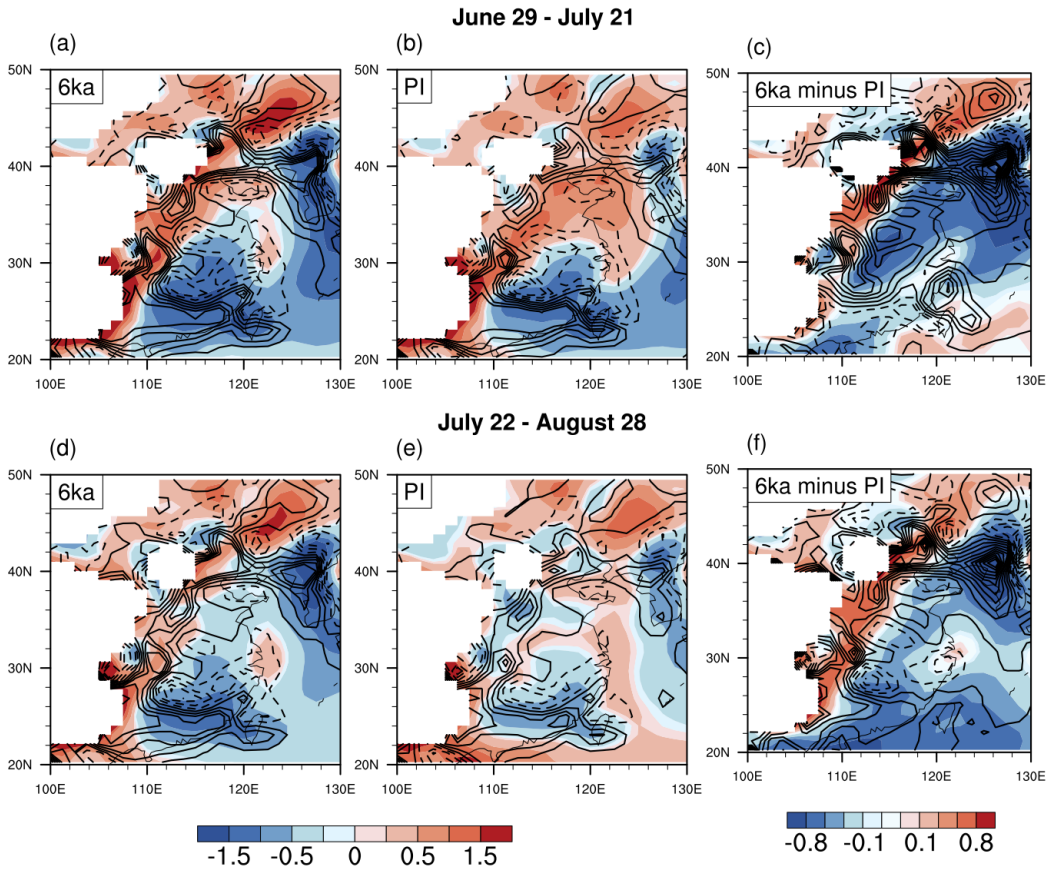

Figure 2.8: Relative vorticity (shading, the unit is $10^{-5}\,s^{-1}$) and moisture divergence [contour, contour interval $0.25 \times 10^{-7}\,s^{-1}$ for (a),(b),(d), and (e), $0.1 \times 10^{-7}\,s^{-1}$ for (c) and (f); negative values are in dashed lines] at 850 mb. Results are shown for (top) 29 Jun–21 Jul (i.e., the mei-yu in PI) and (bottom) 22 Jul–28 Aug (i.e., the midsummer in PI) for (left) 6 ka, (middle) PI, and (right) 6 ka minus PI. Warm (cold) color indicates cyclonic (anticyclonic) vorticity. The solid (dashed) lines indicate moisture divergence (convergence).

2.4.3 Is the PI mei-yu (midsummer) the same as the 6-ka mei-yu (midsummer)?

We have shown that the EASM seasonal stages occur with different timings in the Holocene simulations. A further question we can ask is this: If we compare the climate fields associated with the PI mei-yu (or midsummer) stage with those from the 6 ka (in other words, allowing for the difference in timing and duration), are the fields similar, or not? In other words, does the PI mei-yu (midsummer) dynamically resemble the 6-ka mei-yu

(midsummer)?

The answer appears to be no, at least quantitatively. Figure 2.9 compares the frontal position and the moisture transport between PI mei-yu and 6-ka mei-yu and between PI midsummer and 6-ka midsummer. The fronts and the moisture flux penetration during mei-yu (midsummer) in 6 ka reach more northward locations compared to the PI, indicating more northward positioning of the rain belt in 6 ka. Similar analyses for the westerlies (Figs. 2.10b,d) suggest more northward positioning of the westerlies relative to the Tibetan Plateau in 6-ka mei-yu and midsummer.

This suggests that the 6-ka mei-yu is more intense than the PI mei-yu; the same appears to be the case if the midsummer stages are compared. The reason for this appears to again be tied to the westerlies, namely that a more northward positioned westerly jet in 6 ka relative to the PI allows for more northward-penetrating fronts and moisture flux to occur. However, dynamically, the PI and 6-ka mei-yu (or midsummer) qualitatively resemble each other.

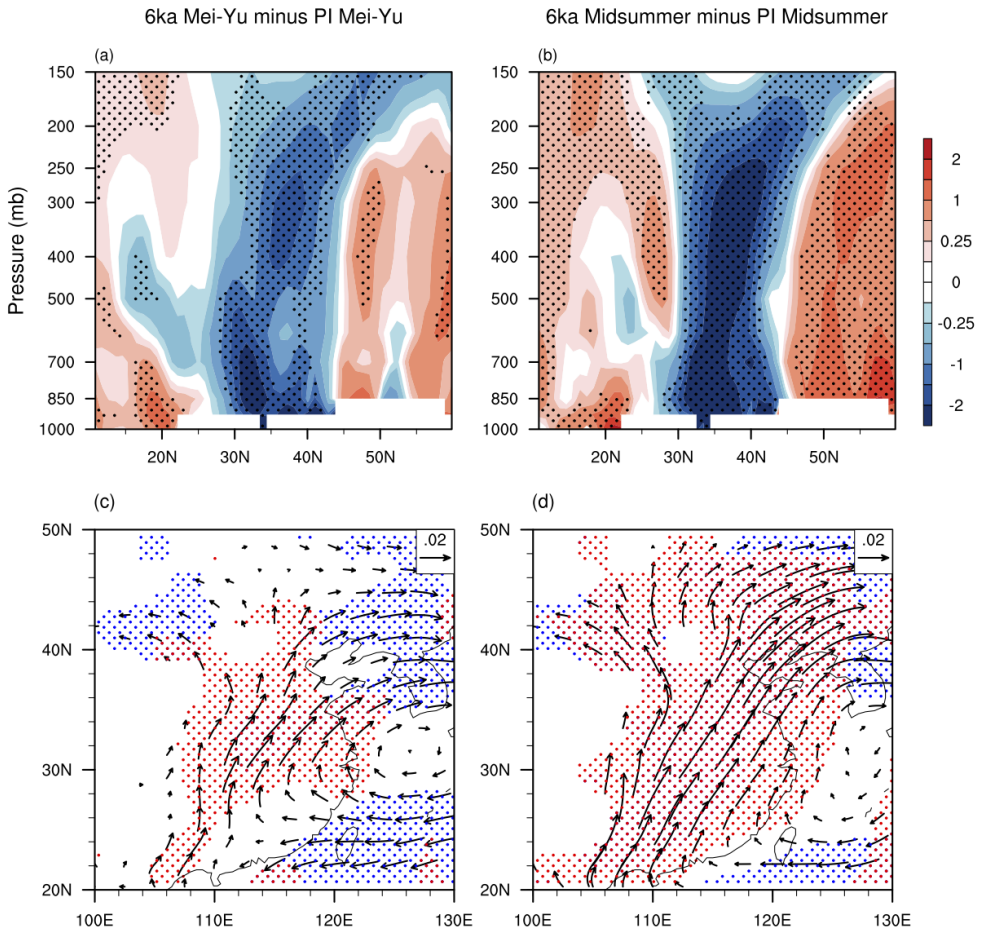

Figure 2.9: (top) The meridional gradient of MSE $[\frac{-\partial(MSE)}{\partial y}]$ (110° to 120° E) for (a) 6-ka mei-yu (23 Jun–8 Jul) minus PI mei-yu (29 Jun–21 July and (b) 6-ka midsummer (9 Jul–12 Sep) minus PI midsummer (22 Jul–28 Aug). The stippled areas indicate that the difference is statistically significant at the confidence level of 90 %. The unit is $3 \times 10^{-6}\,\mathrm{kJ^2\,kg^{-1}\,m^{-1}}$. (bottom) The moisture flux (850mb) for (c) 6-ka mei-yu minus PI mei-yu and (d) 6-ka midsummer minus PI midsummer. The blue (red) dots indicate that the difference in zonal moisture flux ($\mathbf{u}q$) [meridional moisture flux ($\mathbf{v}q$)] is statistically significant at the confidence level of 90%. The unit is $10^3\,\mathrm{g\,kg^{-2}\,m^{-1}\,s^{-1}}$, and the reference vector $0.02 \times 10^3\,\mathrm{g\,kg^{-2}\,m^{-1}\,s^{-1}}$.

2.5 Role of the westerlies in the EASM changes

Chiang et al. (2015) hypothesized that earlier seasonal transitions in the EASM correspond to earlier northward transitions of the westerlies relative to the Tibetan Plateau. This view appears to be supported in our 6-ka Holocene simulation (Figs. 2.10a,c). The strength-

ened westerlies to the north of the PI jet core and weakened westerlies to the south of the PI jet core indicate an earlier northward displacement of the westerly jet in 6 ka during the PI mei-yu phase (Fig. 2.10a) and the PI midsummer phase (Fig. 2.10c) (note that the westerly anomalies to the south of 30° N in Figs. 2.10a, c are due to the weaker easterlies over southern China in 6ka). In the following two subsections, we explore mechanisms linking the seasonality of the EASM to the East Asian westerlies.

2.5.1 The dynamical linkage between the westerlies and the EASM

To understand the origins of the earlier northward migration of the westerlies, we examine changes to the meridional temperature gradient induced by the insolation changes. Figures 2.11a–c show the Hovmöller diagram of the meridional temperature gradient ($-\frac{\partial T}{\partial y}$) at 200 mb over East Asia (80° to 120° E). Compared to the PI, the meridional temperature gradient in 6 ka is weaker, and the northward movement of the maximum gradient belt in 6ka is faster from May to August. Also, the position of the positive temperature gradient is farther north in 6 ka during July and August (see the positive anomaly in Fig. 2.11c). Consistent with the changes in the meridional temperature gradient, the 6-ka features weakened and northward-shifted westerlies, as shown in Figs. 2.11d–f.

With an earlier northward transition of the westerlies across the plateau, the frontal location will also have an earlier northward migration. We interpret the maximum meridional gradient of the MSE as the indicator of the frontal systems and Figs. 2.11g–i show the Hovmöller diagram of the tropospheric meridional MSE gradient $[\frac{-\partial(MSE)}{\partial y}]$ over eastern China (110° to 120° E). In agreement with the changes in the transition of westerlies and rainfall band, the northward shift of the frontal systems in 6 ka is earlier and the fronts reach a more northward location.

Sampe & Xie (2010) suggest that the westerlies traps transient disturbances and these disturbances are conducive for the frontal convection. Thompson & Birner (2012), however, argue that the synoptic eddy fluxes of heat act to reduce the meridional temperature gradient. Both studies imply that the transient eddy activity is another indication of the presence of the fronts. We use the eddy kinetic energy ($EKE = u'^2 + v'^2$) to indicate transient eddy activity (Figs. 2.11j–l). The prime denotes 2.5–6-day bandpass-filtered daily fields. The EKE in 6 ka (Fig. 2.11j) suggests an earlier northward shift of the occurrence of transient eddies, which corroborates the northward shift of the frontal systems in 6ka.

Taken together, the weaker meridional temperature gradient and the earlier northward migration of the East Asian monsoonal fronts and associated transient eddy activity suggest that the earlier northward migration of the westerlies across the plateau, caused by the reduced meridional insolation gradient during the mid-Holocene, is responsible for the changes to the EASM seasonal transitions in the 6-ka simulation.

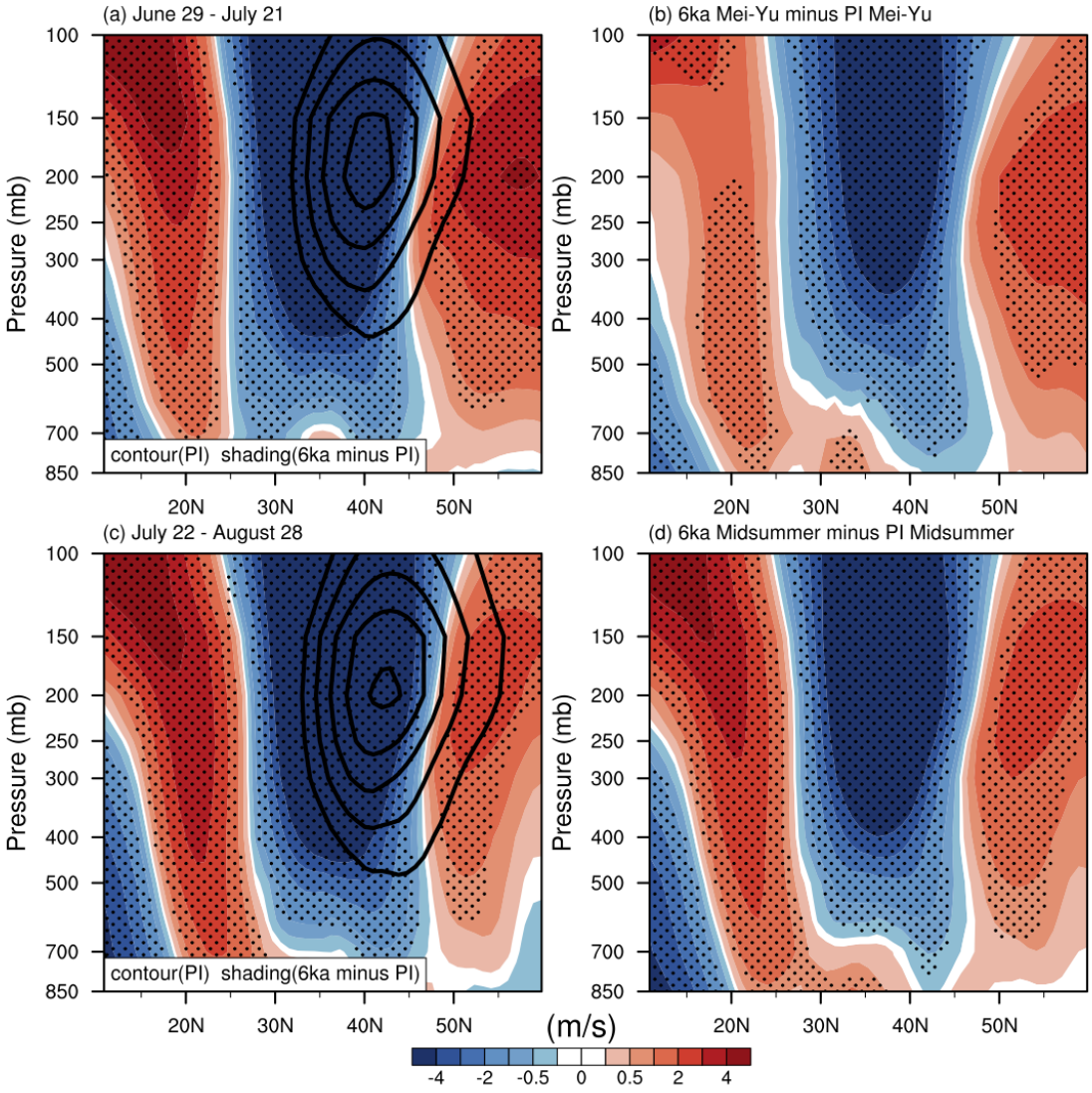

Figure 2.10: (left) The zonal wind (80° to 120° E) during (a) 29 Jun–21 Jul and (c) 22 Jul–28 Aug (contour: PI; shading: 6 ka minus PI). (right) The zonal wind (80° to 120° E) for (b) the 6-ka mei-yu season (23 Jun–8 Jul) minus PI mei-yu season (29 Jun–21 Jul), and (d) the 6-ka midsummer season (9 Jul–12 Sep) minus PI midsummer season (22 Jul–8 Aug). The stippled areas indicate that the differences of zonal wind are statistically significant at the confidence level of 95%.

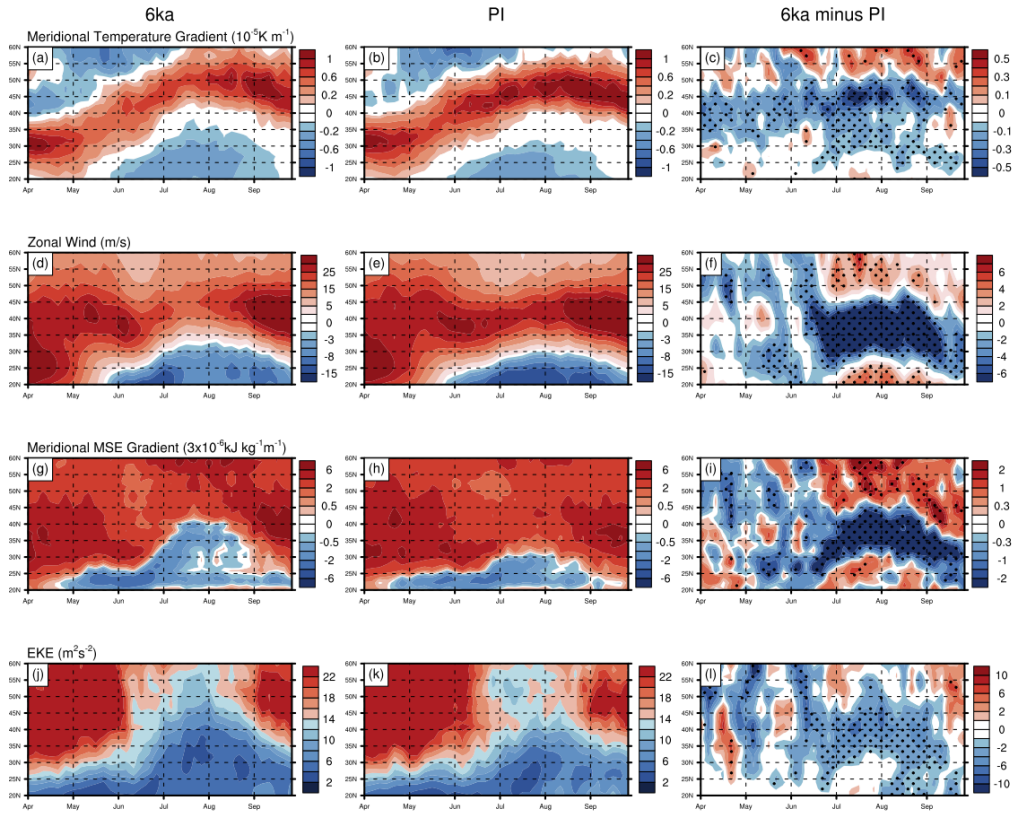

Figure 2.11: Hovmöller diagrams of the (a)–(c) meridional temperature gradient (averaged over 80° to 120° E) at 200 mb, (d)–(f) the zonal wind (averaged in 80° to 120° E) at 200 mb, (g)–(i) the meridional gradient of MSE (averaged over 110° to 120° E) between 300 and 850 mb, and (j)–(l) the eddy kinetic energy (averaged in 110° to 120° E) between 300 and 850 mb, for (left) 6 ka, (middle) PI, and (right) 6 ka minus PI. The unit is $10^{-5}\,\mathrm{K^2\,m^{-1}}$ in (a)–(c), $\mathrm{m\,s^{-1}}$ in (d)–(f), $3\times10^{-6}\,\mathrm{kJ^2\,kg^{-1}\,m^{-1}}$ in (g)–(i), and $\mathrm{m^2\,s^{-2}}$ in (j)–(l). The stippled areas indicate that the difference is statistically significant at the confidence level of 90 %.

2.5.2 Threshold of the westerlies' position in determining the EASM seasonality

We have shown that the timing of the EASM seasonal transitions is linked to the meridional positioning of the westerlies over East Asia. We also argued (see section 2.4c) that although the timing of the EASM seasonal stages changes across the Holocene, the dynam-

ical configuration determining each stage remains essentially unchanged. Here we ask: Is there a physical threshold of the position of the westerlies that can exactly determine the timing of the mei-yu or midsummer onset? To answer this question, we examine the position of the westerlies across the plateau during the mei-yu onset and the midsummer onset.

Figure 2.12 shows the meridional position of the maximum westerlies over the Tibetan Plateau (80° to 100° E) at 200mb. Figure 2.12a shows that compared to the late Holocene (3 ka and PI), the northward shift of the jet axis occurs earlier in the early to mid-Holocene (9 and 6ka), and the position of the jet axis in the early to middle Holocene is more northward displaced.

Figure 2.12b shows that the axis of the westerlies relative to the Tibetan Plateau is located at 40° N during the mei-yu onset for all simulation cases, suggesting that this latitude acts as a threshold for triggering mei-yu onset. The left column of Fig. 2.13, which shows the meridional position of the maximum westerlies at mei-yu onset as a function of longitude, further confirms the consistent meridional positioning of the jet axis over the plateau longitudes at the mei-yu onset across the simulations. The position of the jet axis downstream of the plateau, though, shows some variation across the simulations. Unlike the mei-yu onset, there does not appear to be a consistent latitudinal threshold for the maximum westerlies associated with the onset of the midsummer stage. For example, Figs. 12b and 13b show that the onset of midsummer is associated with a 1° to 2° northward shift of the westerly jet axis from the mei-yu threshold position of 40° N.

Taken together, our simulations suggest that the mei-yu onset is linked to the maximum upper-tropospheric westerlies crossing a particular meridional position over the Tibetan region. It suggests that the position of the westerlies relative to the Tibetan Plateau provides the dynamical constraint that determines the start of mei-yu season. However, the position of the westerlies does not seem to be the deterministic factor for the midsummer onset. Therefore, we speculate that the onset process of the midsummer stage is more complex, with more than one factor playing a role. We will further explore the mechanisms associated with the onset of the mei-yu and midsummer patterns in follow-up studies.

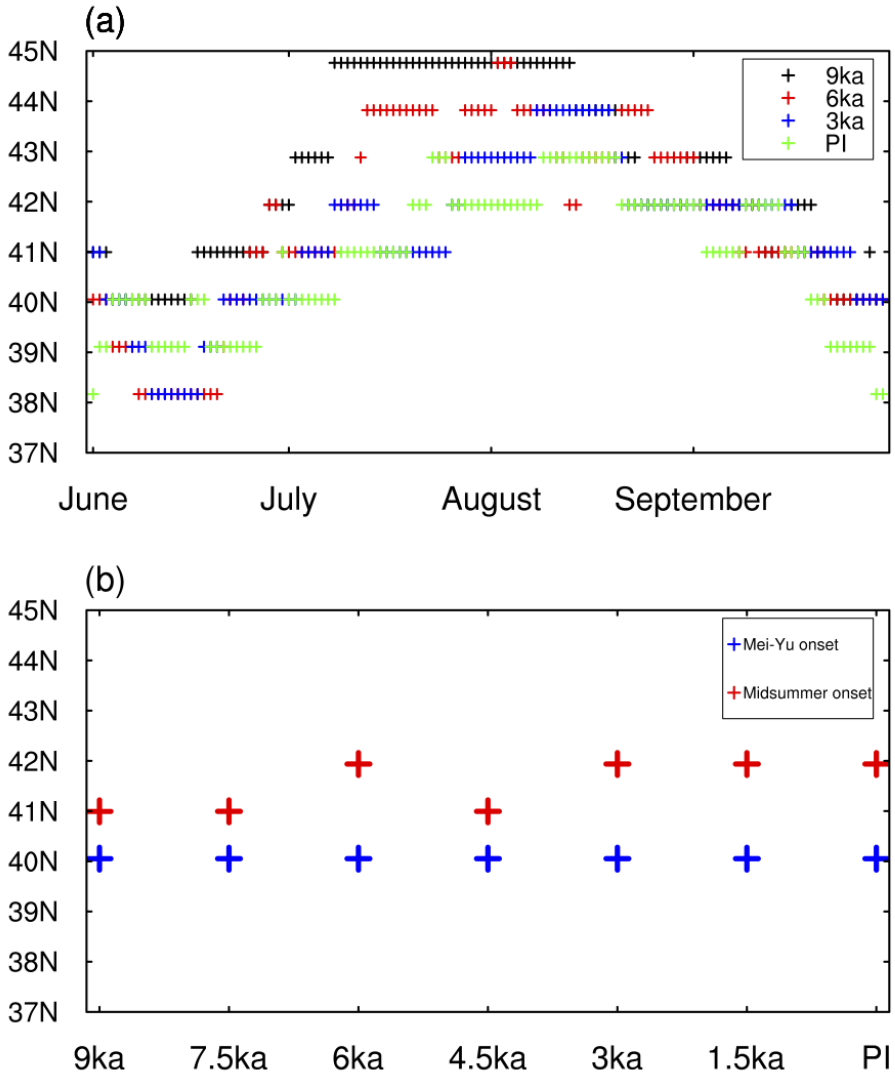

Figure 2.12: (a) Meridional position of the June–September maximum zonal wind at 200 mb between 80° and 100° E in 9 ka (black crosses), 6ka (red crosses), 3ka (blue crosses), and PI (green crosses). (b) Meridional position of the maximum zonal wind at 200mb between 80° and 100° E across the simulated Holocene during mei-yu onset (blue crosses) and midsummer onset (red crosses). Note that (a) is based on the daily climatology after 5-day running average, and (b) is based on the 5-day running average with the mei-yu/midsummer onset date as the center day.

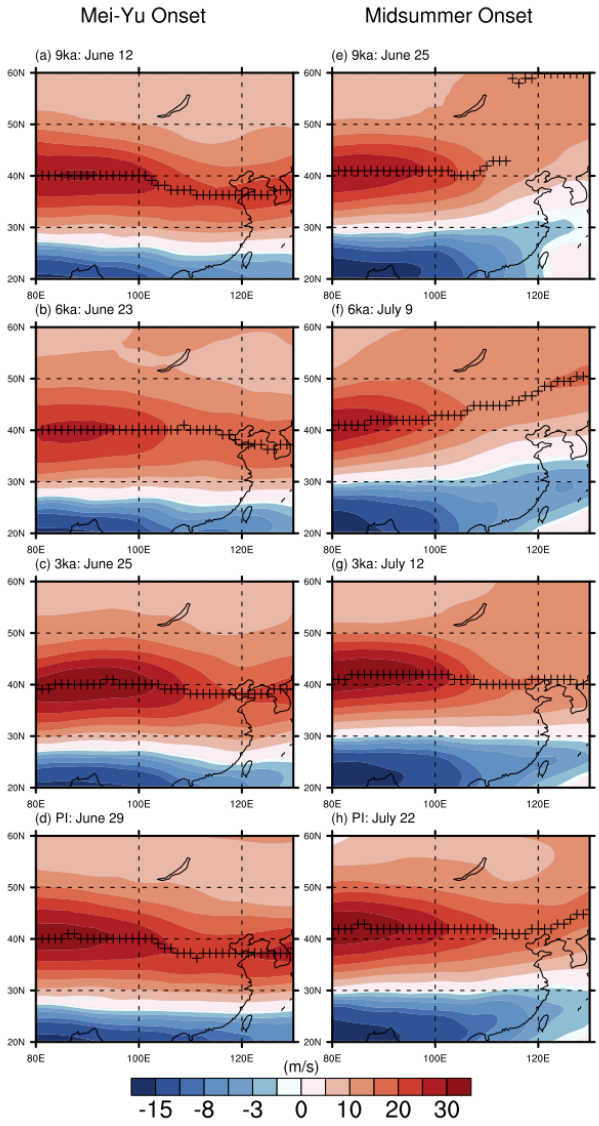

Figure 2.13: (left) Zonal wind at 200 mb (warm color: westerlies; cold color: easterlies; unit: $\mathrm{m\,s^{-1}}$) during the mei-yu onset (a) 9 ka: 12 Jun, (b) 6 ka: 23 Jun, (c) 3 ka: 25 Jun, and (d) PI: 29 Jun. (right) As at left, but for the midsummer onset (e) 9 ka: 25 Jun, (f) 6 ka: 9 Jul, (g) 3 ka: 12 Jul, and (h) PI: 22 Jul. The crosses denote the latitude position of the maximum zonal wind. For each simulation, the result is based on the 5-day average with the mei-yu/ midsummer onset date as the center day.

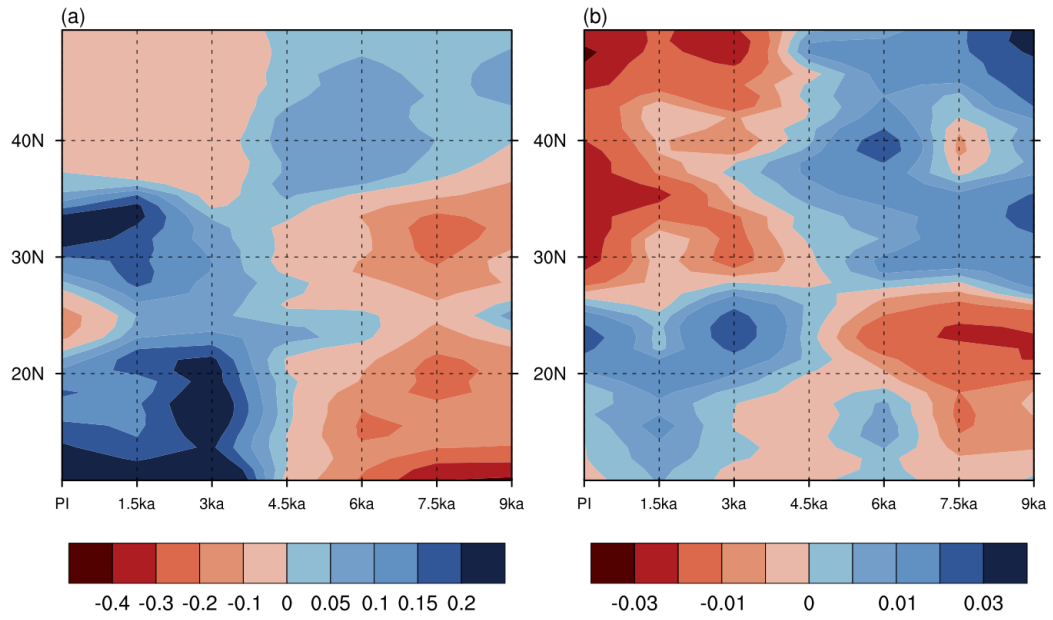

Figure 2.14: (a) Annual total precipitation amount (110° to 120° E) change from 9 ka to PI and (b) annual convective-to-total precipitation (convective/total) ratio change from 9 ka to PI. The convective/total ratio is calculated from proportion of convective precipitation rate to total precipitation rate between 100° and 120° E. In (a), the mean value of 9 ka to PI is removed for each simulation, cold color indicates higher annual total precipitation amount and vice versa. In (b), the mean convective/total ratio value of 9 ka to PI is removed for each simulation, cold color indicates higher convective/total ratio and vice versa.

2.6 Interpretation of the Holocene EASM pollen and dust records from a seasonality perspective

In this section, we further demonstrate the validity of our hypothesis by comparing our simulations with two key paleoproxy records over East Asia. We show that focusing on seasonal transitions, as opposed to the conventional focus on monsoon intensity, can provide new insights into the interpretation of these records.

2.6.1 Asynchronous Holocene optimum

Based on an interpretation of Chinese lake levels, pollen sequences, and eolian deposit records, An et al. (2000) proposed the "asynchronous Holocene optimum" hypothesis of a stepwise latitudinal shift of the maximum rainfall from northwestern China in the early Holocene (10–8ka) to southeastern China in the late Holocene (3ka), in response to the progressively decreased summer insolation. They argued that the weakened Northern Hemisphere insolation seasonality induces the weakening of the EASM and therefore the southward retreat of the northernmost frontal zone from the early Holocene to the late Holocene, resulting in the southward shift of the maximum rainfall belt. The view proposed by An et al. (2000) cannot be explained by the conventional interpretation of viewing paleo-EASM changes simply in terms of intensity, since it implies that the Holocene "optimum" should occur at the same time at all locations in China.

We argue that seasonal transitions provide a more satisfactory interpretation than An et al. (2000) result. Figure 2.14 presents the evolution of the EASM annual total rainfall amount (100° to 120° E) (Fig. 2.14a) and the convective-to-total precipitation (convective/total) ratio (Fig. 2.14b) from 9ka to PI. Figure 2.14a shows that the simulated peak annual rainfall band shifts southward from 9 ka to PI, in agreement with the asynchronous Holocene optimum hypothesis (An et al., 2000). Moreover, Fig. 2.14b shows a southward shift of the peak convective-to-total precipitation ratio from 9ka to PI, reflecting the southward displacement of the frontal systems from 9 ka to PI. Thus, we attribute the asynchronous Holocene optimum hypothesis (An et al., 2000) to the changes in both timing and duration of the EASM seasonal transition across the Holocene. In the early Holocene, the midsummer rainfall season occurs earlier and stays longer, thus the maximum annual rainfall amount occurs over northern China (cf. Figs. 2.3b and 2.3d). In the mid-Holocene, the midsummer rainfall stage starts later and ends earlier, leading to reduced rainfall over northern China; on the other hand, the mei-yu rainfall duration is longer, leading to increased rainfall over central China, and the so-called Holocene optimal rainfall occurs there (Fig. 2.3c). In the late Holocene, the relatively late start of the mei-yu season determines the lengthened spring and pre-mei-yu rainfall stage, leading to more rainfall over southern China; on the other hand, the midsummer rainfall stage over northern China is further shortened, reducing the rainfall amount over northern China. The above interpretation for the asynchronous Holocene optimum hypothesis is in agreement with the schematic model summarized in Fig. 5 of Chiang et al. (2015) and is in alignment with our simulation results as well (e.g., Fig. 2.3).

We note that our results and interpretation differ from a recent modeling study by (Jin et al., 2014). They also find regional disparity of the Holocene optimum precipitation between northeastern China and central-eastern China. However, in contrast to An et al. (2000), their modeling results suggest that the peak precipitation over central and southeastern China occurred synchronously, and earlier than that over northeastern China, leading them to conclude that "the previously-proposed time-transgressive Holocene climate across China (e.g. An et al. (2000) is not supported by [their] study" ((Jin et al., 2014), p. 58).

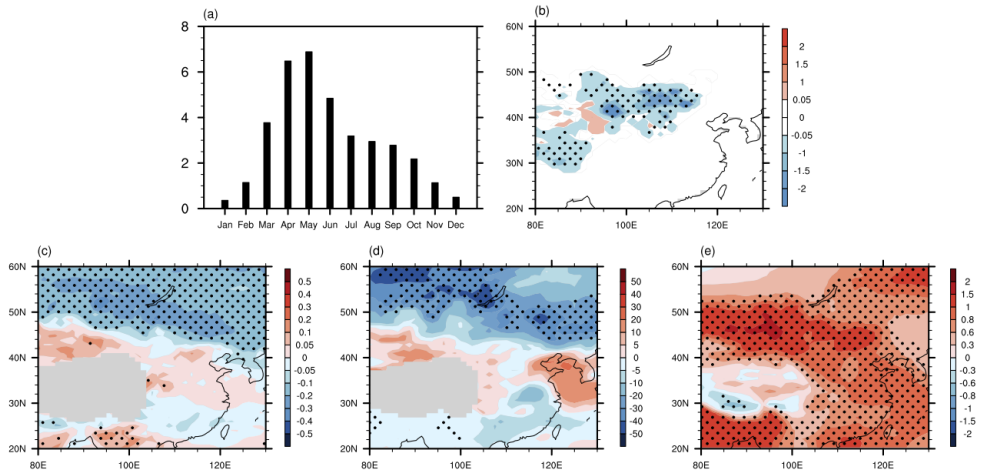

Figure 2.15: (a) Monthly dust emission over high dust emission region (33.5° to 52° N, 88.5° to 131.5° E) from the PI simulation and (b) change of the annual mean dust emission between 6 ka and PI (6 ka minus PI). The unit is $Tg\ m^{-2}\ s^{-1}$ in (a) and (b). Also shown is the difference between 6ka and PI (6ka minus PI) for MAM for (c) the meridional temperature gradient averaged over 700–1000mb (unit: $10^{-5}\ K^2\ m^{-1}$), (d) the variance of 2.5–6 days bandpass-filtered daily geopotential height averaged over 700–1000 mb (unit: m^2), and (e) sea level pressure (unit: mb). The stippled areas indicate that the difference is statistically significant at the confidence level of 90%.

2.6.2 Changes to dust emissions

Dust proxies are thought to reflect changes to the westerlies in the past climate. For example, both An et al. (2012) and Nagashima et al. (2011, 2013) indicate that the enhanced dust emission over East Asia is associated with the southward-shifted westerlies during times of colder climates. Nagashima et al. (2011, 2013) hypothesized that the seasonal jet transitions from south of Tibet to the north were delayed during Dansgaard–Oeschger stadials.

Given that the dust emission over East Asia mainly occurs in spring as cyclogenesis maximizes in that season (Roe, 2009), the suggestion is that the dustier climate over East Asia is associated with prolonged spring rainfall season and southward-shifted westerlies.

If (as per our hypothesis) the westerlies were displaced southward and the rainfall seasonal transition was delayed in the late Holocene, we should see dustier climate during the late Holocene compared to the early to mid-Holocene; indeed, this is what our simulation shows. The monthly dust emission over the major dust outbreak region [33.5° to 52° N, 88.5° to 131.5° E, adapted from Kurosaki & Mikami (2003)] in PI (Fig. 15a) shows a reasonable seasonal cycle compared to observations (Kurosaki & Mikami, 2003), with the exception of May when the simulated dust emission is too high. The simulated dust emission in the PI is indeed larger than that in 6 ka over East Asia (Fig. 2.15b). The climatological annual mean dust emission over 33.5° to 52° N, 88.5° to 131.5° E is 3.02 $Tg\ m^{-2}\,s^{-1}$ in the PI and 2.78 $Tg\ m^{-2}\,s^{-1}$ in the 6 ka, and the Student's t test suggests that the difference between the two is statistically significant at a confidence level of 95 %.

Roe (2009) suggests that the transient eddy disturbances in the atmospheric circulation and strong meridional temperature gradients are the two major prerequisites for the dust-generating windstorms. We argue that the dustier climate in the PI is due to the prolonged springtime, which is characterized by stronger meridional temperature gradient and storminess over East Asia as seen in Figs. 2.15c, d. The strength of the Siberian high in spring is thought to be negatively correlated to the dust outbreak frequency in Asia (Ding et al.). Figure 2.15e suggests a weaker Siberian high during the PI spring, which further supports the enhanced dust emission as noted in Fig. 2.15b. Apart from the foregoing analyses, the delayed mei-yu onset during PI also leads to a deficit in soil moisture over the dust emission region, and thus enhances the dust lofting.

2.7 Conclusions and discussion

The Holocene EASM evolution, inferred from proxies such as the $\delta^{18}O_c$ records in Chinese caves (Wang et al., 2008b, 2001), has been typically interpreted to be a weakening of the monsoon intensity from the early Holocene to the present day. Given that today's EASM is characterized by three distinct seasonal regimes and abrupt transitions in between, this interpretation is incomplete and a fuller account of the Holocene EASM changes must include the changes to these seasonal transitions. In this study, we investigate the changes in the seasonal transitions of the EASM during the Holocene based on the simulation from CAM5 that is capable of simulating today's seasonal transitions with fidelity. Following a previous lead (Chiang et al., 2015), we test the hypothesis that the changes in the seasonal transition of the Holocene EASM are determined by the altered position of the westerly jet relative to the Tibetan Plateau.

We explored the Holocene EASM in a set of CAM5 simulations spanning various time periods in the Holocene (9, 7.5, 6, 4.5, 3, 1.5 ka, and PI). We showed that compared to the late Holocene, the early to mid-Holocene is characterized by an earlier onset of the mei-yu

and midsummer rainfall seasons, with a shorter duration of mei-yu and longer duration of midsummer. In particular, the simulations suggest that the mid-summer stage was twice the duration and the mei-yu half the duration during the early Holocene as in the present. In confirmation of the altered seasonality of the EASM, the early to mid-Holocene also featured northward- shifted mei-yu and midsummer rainfall fronts as well as more northward penetration of the moisture flux. The meridional position of the high cyclonic vorticity and the moisture convergence further corroborates the above interpretation. It should be mentioned that we obtained similar results—namely, that the mid-Holocene featured earlier EASM seasonal transition than the preindustrial—from four PMIP3 models (CCSM4, BCC-CSM1.1, FGOALS-g2, FGOALS-s2) that are able to simulate the EASM with fidelity (see the Appendix A).

In terms of the role of the westerlies, the northward positioning of the westerlies relative to the Tibetan Plateau in the early Holocene appears linked to the earlier timing of the seasonal transitions. The insolation over the Northern Hemisphere summer was increased in the early Holocene, leading to a northward shift in the maximum meridional temperature gradient and hence the westerlies. Transient eddies over East Asia are also northward shifted in the early to mid-Holocene, further indicating the northward displacement of the frontal systems during that time. Our analysis suggests the existence of specific thresholds (40° N) in the meridional position of the westerlies over the Tibetan region (80° to 100° E) that controls the mei-yu onset across the Holocene. This is not true, however, for the midsummer stage onset.

The mei-yu and midsummer rainfall stages in the early to mid-Holocene appear more intense than their counterparts in the late Holocene. This is also associated with the more northward positioned westerlies in the early to mid-Holocene. However, the underlying dynamics of the EASM in the early to mid-Holocene and the late Holocene resemble each other qualitatively.

We also compare our simulations against two well-known paleoproxy studies of the East Asian paleoclimate and offer an interpretation based on the seasonal transition perspective. In agreement with the "asynchronous Holocene optimum" hypothesis (An et al., 2000), the simulated changes in the annual rainfall amount and the (convective/total) ratio over East Asia suggest that the latitudinal position of the maximum rainfall band moves southward from the early Holocene to the late Holocene. We argue that this phenomenon is readily interpretable if we consider that the seasonal transitions from spring/pre-mei-yu to mei-yu and from mei-yu to midsummer occurred later as the Holocene progressed. We also find that the simulated late Holocene is dustier than the mid-Holocene over East Asia, which is consistent with the argument that the enhanced dust emission over East Asia is associated with the southward-shifted westerlies during colder climate (An et al., 2012; Nagashima et al., 2013, 2011). Given that the dust emission over East Asia is mainly a springtime phenomenon (Roe, 2009), the dustier late Holocene is a further confirmation of the delayed onset of the mei-yu (i.e., the prolonged spring/pre-mei-yu rainfall season).

It is not the purpose of this paper to fully elucidate the mechanistic links between the westerlies and the EASM seasonality. The overarching question that we will explore in future

studies is this: what characteristics of the westerlies are most relevant to each seasonal stage of EASM? Besides the meridional positioning of the westerlies, the potential candidates include the width, the vertical structure, and the strength of the westerlies. During the transition from spring to pre-mei-yu, the westerlies shift poleward from southern China to the south edge of the Tibetan Plateau (Schiemann et al., 2009); however, the meridional positioning of the rainfall over southern China between spring and pre-mei-yu is similar (Fig. 2.1). The strength as well as the westward extension of the pre-mei-yu rain belt, however, is intensified. Unlike the difference between mei-yu and midsummer rainfall, the northward shift of the westerlies does not affect the meridional position of the rain belt during the transition from spring to pre-mei-yu. For the mei-yu onset, our analysis suggests that the meridional positioning (40° N) of the westerlies axis at 200 mb relative to the Tibetan Plateau is a strong determinant thereof, but this needs further examination. Specifically, what are the specific dynamics that determine why the mei-yu onset occurs at this latitude? A latitudinal threshold does not appear to hold for the midsummer onset, and this begs the question of whether there are other factors that affect the onset of the midsummer stage.

There are still fundamental questions to be answered regarding the role of stationary eddies and transient eddies associated with westerly atmospheric circulation across East Asia. Stationary eddies downstream of the Tibetan Plateau are thought to be the main factor for the formation and maintenance of the East Asian monsoon front by converging warm, moist air from the south with the cold, dry air from the north (Staff Members of the Section of Synoptic and Dynamic Meteorology, 1957). Therefore, we postulate that the westerlies exert a modulation of the seasonality of the EASM via controlling the behavior of the stationary eddies downstream of the plateau. The role of the transient eddies in the EASM seasonality is not yet fully understood. On one hand, the transient eddies are argued to smooth out the meridional temperature gradient (Thompson & Birner, 2012); on the other hand, Sampe & Xie (2010) suggest that the transient disturbances trapped along the westerlies facilitate the mei-yu frontal convection.

2.8 Acknowledgments

We thank Nathaniel Johnson for sharing his SOMs analysis code, and Shing Chang for her assistance in implementation. Mike Wallace suggested the use of SOMs to analyze East Asian rainfall seasonality. We thank Chi-Hua Wu, Inez Y. Fung, and Yanjun Cai for valuable discussions. We thank Dr. Mathew Barlow and the three anonymous reviewers for their constructive comments. WK thanks Jun Yang for helpful conversations on the use of the Community Earth System Model. APHRODITE precipitation data were obtained from `http://www.chikyu.ac.jp/precip/index.html`. We thank the Paleoclimate Modelling Intercom-parison Project Phase III (PMIP3) for producing and making available their model output. We acknowledge high-performance computing support for the CAM5 from the Yellowstone cluster (ark:/85065/d7wd3xhc) provided by NCAR's Computational and Information Systems Laboratory, sponsored by the National Science Foundation. We use the

NCAR Command Language (http://www.ncl.ucar.edu) to perform the calculation and visualization, and MATLAB (http://www.mathworks.com/products/matlab/) to perform the self-organizing maps (SOMs) analysis. This work was funded by National Science Foundation Grant AGS-1405479.

Chapter 3

Interaction of the westerlies with the Tibetan Plateau in determining the mei-yu termination

3.1 Introduction

The mei-yu (also known as changma in Korea and baiu in Japan) is a quasi-stationary rain belt extending from central eastern China to Japan, establishing around mid-June and disappearing around mid-July. The dynamics of the mei-yu are intimately tied to the westerlies impinging on the Tibetan Plateau. In particular, the synchronous relationship between the latitudinal position of westerlies over the Tibetan Plateau and the spatial pattern of the East Asian summer rain belt has long been recognized (Liang & Wang, 1998; Molnar et al., 2010; Murakami, 1951; Schiemann et al., 2009; Staff Members of the Section of Synoptic and Dynamic Meteorology, 1958a; Yeh et al., 1959). For example, Schiemann et al. (2009) note that the westerly jet migrates onto the Tibetan Plateau in May, corresponding to the pre-mei-yu in southeastern China; the westerly jet reaches the northern edge of the plateau in June, timed to the mei-yu over central eastern China; as the jet migrates well north of the plateau in July–August, midsummer occurs and brings more rainfall over northeastern China. Decreased summer rains over the Yangtze River Valley—the region dominated by the mei-yu—have been argued to be associated with the poleward displacement of westerlies in East Asia, and vice versa (e.g., (Li & Zhang, 2014)). Recent studies further suggest that the meridional positioning of the Asian westerly jet relative to the Tibetan Plateau controls the timing and duration of the mei-yu in both past (Chiang et al., 2015; Kong et al., 2017) and present (Chiang et al., 2017) climates.

A variety of mechanisms have been proposed for how the westerlies modulate the mei-yu. Japanese meteorologists noted that the demise of the baiu is associated with the establishment of an anticyclone over Japan around August, the latter being part of an eastward propagating wave train—the so-called Silk Road pattern (Enomoto et al., 2003). Subsequent studies suggest that the interannual variation of the East Asian summer monsoon (EASM)

is closely associated with the Silk Road pattern (Hsu & Lin, 2007; Kosaka et al., 2011). Li & Lu (2017) suggest that increased precipitation in the Yangtze River basin is linked to northeasterly anomalies to the north of the region. They argue that the northeasterly anomaly in the lower troposphere is associated with the cyclonic anomaly over East Asia in the upper troposphere, and that the latter is induced by the Silk Road pattern along the westerly jet. In fact, behavior of the Silk Road pattern is closely linked to the meridional position of Asian westerlies (Hong & Lu, 2016; Hong et al., 2017). For instance, Hong & Lu (2016) suggest that when the jet is displaced southward, the Silk Road pattern tends to present as cyclonic anomalies over East Asia, and vice versa. Hong et al. (2017) further demonstrate that the Silk Road pattern is more pronounced when the jet is located to north of the Tibetan Plateau. Taken together, these studies suggest that westerlies might affect the mei-yu through modulating the variation of the Silk Road pattern.

On the other hand, precipitation over central eastern China during the mei-yu exhibits strong correlation with ascending motion and horizontal warm advection in the midtroposphere (e.g., (Sampe & Xie, 2010)). This strong correlation led Sampe & Xie (2010) to conclude that the westerly jet anchors the mei-yu rainband via the advection of warm air from the southeastern flank of the Tibetan Plateau, which is then lifted upward over East Asia, thereby inducing convection. This argument attributes the demise of the mei-yu to the northward migration of the jet away from the maximum midtropospheric temperature center; this interpretation is further supported by studies on variations of East Asian summer rainfall at interannual time scales (Kosaka et al., 2011).

A different view of the role of the westerlies on the mei-yu was postulated by Molnar et al. (2010). They focus on the effect of the westerlies impinging on the Tibetan Plateau in altering the downstream circulation, specifically producing a locus of moisture convergence that defines the mei-yu rainband. In this view, the demise of the mei-yu rainband is dynamically tied to the northward seasonal migration of the westerlies from south to north of the plateau: when the core of the westerlies migrates off the plateau, the mechanical forcing of the plateau disappears, and so does the mei-yu rainband. From an energetic and moisture budget perspective, Chen & Bordoni (2014) argued that the extratropical northerlies downstream of the Tibetan Plateau are crucial in maintaining the mei-yu front via advecting dry enthalpy and strengthening the moisture convergence over central eastern China.

The above studies suggested different processes for how the westerlies affect the mei-yu. Although the origins of these mechanisms are independent, they consistently indicate the meridional position of the westerly jet relative to the Tibetan Plateau is key to formation and maintenance of the mei-yu. However, how this dynamically relates to the demise of the mei-yu has not been examined in detail; this is the focus of this paper[1]. Furthermore, since the termination of the mei-yu is abrupt, it raises the question of whether a latitude threshold in terms of jet position exists over the plateau that triggers the mei-yu termination. A recent modeling study on seasonal transitions of the jet and of the EASM during the

[1]As mentioned at the beginning of this section, the mei-yu is a more distinct rainfall stage of the EASM compared to midsummer. So we phrase the focus of this study in terms of termination of the mei-yu, instead of onset of midsummer (or post-mei-yu)

Holocene suggests exactly this (Kong et al., 2017). In that study, the maximum in the 200-mb ($1mb = 1hPa$) westerly jet over the Tibetan Plateau (80° to 100° E) was found to be located at 40° N during the mei-yu onset, and the jet axis migrates northward by 1° or 2° when the mei-yu ends. Notably, 40° N is the latitude where the mean plateau elevation across 80° to 100° E drops below 1.5 km, marking the northern edge of the plateau. It suggests that 40° N acts as this threshold, and mei-yu ends when the jet core migrates to north of 40° N.

In this study, we confirm previous findings (Kong et al., 2017) that the termination of the mei-yu indeed coincides with the maximum upper tropospheric westerlies over the Tibetan Plateau shifting north of 40° N. We also find that these changes are accompanied with disappearance of tropospheric northerlies over northeastern China (35° to 40° N). We show that these concurrent behaviors hold from climatology to interannual and synoptic time scales, which motivate us to hypothesize that migration of the jet impinging over the plateau to north of 40° N causes the weakening of orographic downstream northerlies, and that this weakening in northerlies over central-northeastern China acts to terminate the mei-yu.

Mountains have long been held to be important in shaping the circulation and climate in the Northern Hemisphere midlatitudes (Bolin, 1950; Broccoli & Manabe, 1992; Manabe & Terpstra, 1974). Model simulations have suggested that the presence of the orography over Asia is essential for the existence of the Asian monsoon (Hahn & Manabe, 1975; Kitoh, 2004; Park et al., 2012; Wong et al., 2018; Wu et al., 2012). A widely held view is that elevated sensible heating over the Tibetan Plateau drives the EASM (Flohn, 1957; Li & Yanai, 1996; Wu et al., 2012; Yeh et al., 1959). However, this view is challenged by studies that emphasized the role of the mechanical influence of the Tibetan Plateau on its surrounding circulations (e.g., (Molnar et al., 2010; Park et al., 2012; Staff Members of the Section of Synoptic and Dynamic Meteorology, 1958a).

In this study, we argue that topographically forced stationary waves provide a potential dynamical link between the westerlies impinging on the Tibetan Plateau and the downstream northerly response. In the midlatitudes, the linear response of the atmosphere to orographic forcing shows equatorward propagation of the stationary Rossby wave and the generation of low-level cyclonic motion downstream of the mountain (Cook & Held, 1992; Held, 1983; Hoskins & Karoly, 1981). Following these studies, we attribute variations of northerlies over northeastern China to changes in the strength of the cyclonic circulation downstream of the plateau. We argue that migration of the jet to the north of the plateau weakens the orographic forcing and thus weakens the cyclonic circulation, leading to weakening and even disappearance of the northerlies.

We describe the data, methodology, and experiments in the next section. In section 3.3, we show how the climatological mean atmospheric circulation changes during the mei-yu termination. We then examine the variation of the mei-yu termination at interannual time scales and mei-yu-like rainfall patterns at synoptic scales in section 3.4. We explore how weakening of northerlies over central-northern eastern China affects the mei-yu termination in section 3.5. In section 3.6, we propose a hypothesis on the mei-yu termination and employ idealized simulations to test the response of northerlies and mei-yu termination to changes

in the orographic forcing by perturbing the northern edge of the Tibetan Plateau. We then use the dry dynamical core of a general circulation model (GCM) to explore the change to the orographic downstream northerlies as the location of westerlies changes from south to north of the plateau (section 3.7). We close the chapter with summaries in section 3.8.

3.2 Data, methods, and experiments

3.2.1 Data

We use winds, geopotential height, temperature, and specific humidity from the European Centre for Medium- Range Weather Forecasts (ECMWF) interim reanalysis (ERA-Interim) products (Dee et al., 2011), spanning the 29-yr period from 1979 to 2007. Daily fields are obtained by averaging the 6-hourly products mapped onto a $1^\circ \times 1^\circ$ grid on the standard pressure levels.

As with Kong et al. (2017), we use the APHRO_MA_025deg_V1003R1 product from the APHRODITE rain gauge data (Yatagai et al., 2009) to present summer rainfall in East Asia. We focus on the period of 1979–2007 for consistency with the ERA-Interim dataset.

3.2.2 Self-organizing maps

Following Chiang et al. (2017) and Kong et al. (2017), we use self-organizing maps (SOMs) (Kohonen et al., 1996; Kohonen, 2001) to objectively extract the seasonal EASM rainfall stages and identify the termination of the mei-yu. The SOM is a neural network–based cluster analysis that classifies a high-dimensional dataset into representative patterns (Kohonen et al., 1996; Kohonen, 2001). This method has been applied successfully to extract patterns of El Niño–Southern Oscillation (Johnson et al., 2013) and the Northern and Southern Hemisphere teleconnections (Chang & Johnson, 2015); Johnson et al. (2008). It has also been used on the intraseasonal oscillation of the Indian summer monsoon (Chattopadhyay et al., 2008) and the East Asian–western North Pacific summer monsoon (Chu et al., 2012).

The SOM analysis of the APHRODITE daily climatology used in this study is similar to that in Kong et al. (2017), to which the readers are referred for details. This study differs from Kong et al. (2017) in that we focus on a shorter period covering 1979–2007 and that we use the 9-day running mean [instead of the 5-day mean as in Kong et al. (2017)] of daily climatology for the SOM analysis.

3.2.3 Definition of jet position

We quantify the position of the westerly jet over the plateau based on its axis at 200 mb. We first zonally average the zonal wind at 200 mb between 80° E and 100° E, overlapping with the main body of the Tibetan Plateau. We then identify the location of the maximum zonal wind between 20° N and 50° N as the jet axis impinging on the plateau. We restrict

the search latitudes to 20° to 50° N in order to exclude the potential identification of the polar front jet at higher latitudes.

3.2.4 Model experiments

We use the National Center for Atmospheric Research's (NCAR) Community Earth System Model (CESM) version 1.2.2 (Hurrell et al., 2013). Previous work (Chiang et al., 2015; Kong et al., 2017) shows that this model simulates the seasonality of the EASM with fidelity. We design two sets of experiments: 1) testing the behavior of the mei-yu under "northward-extended plateau" scenarios, and 2) testing responses of orographic downstream northerlies by perturbing relative positioning of westerlies to the plateau in idealized simulations with a dry dynamical core.

For the northward-extended plateau simulations (section 3.7), we use the F_1850_CAM5 component set (Vertenstein et al., 2011), which includes the coupler, active atmosphere, land, and ice components, and a data ocean model with fixed sea surface temperature (SST). The atmospheric component of the CESM1 is the Community Atmosphere Model version 5 (CAM5) (Neale et al., 2010) at 0.9° × 1.25° horizontal resolution and with 30 vertical layers. We conduct four simulations, namely, Plateau_control, Plateau_3deg, Plateau_6deg, and Plateau_10deg. The only difference among these simulations is the meridional dimension of the Tibetan Plateau. Plateau_3deg, Plateau_6deg, and Plateau_10deg represent scenarios where the northern edge of the plateau is extended northward by 3°, 6°, and 10°, respectively. To generate topography files for these simulations, we first modify a global elevation dataset mapped onto the model grid (0.9° × 1.25°), which is obtained from NCAR's supercomputer. We then use the NCAR Global Model Topography Generation Software (Lauritzen et al., 2015) to smooth the modified topography files.

Figure B.1 (see the Appendix B) shows the boundary topography in East Asia for these simulations. We take the Plateau_3deg run as an example to describe how we extended the northern edge of the Tibetan Plateau. We first target the region 35° to 55° N, 60° to 110° E (simply called the "source region" hereafter), as highlighted by the black box in Fig. B.1a. We then shift the elevation in this region northward by 3°, replacing the elevation in the region 38° to 58° N, 60° to 110° E (the black box in Fig. B.1b) with the elevation of the source region. By doing so, we leave a topographic gap in the middle of the plateau, as indicated by the dashed box in Fig. B.1b. We fill the gap with the elevation of today's Tibetan Plateau around that latitude. Figures B.1e–h present the vertical cross sections of modified elevation in the plateau region.

The greenhouse gas (GHG) concentrations are set to default values as in the CESM preindustrial configuration (i.e., CO_2 is 284.7 ppm, CH_4 is 791.6 ppb, and N_2O is 275.68 ppb). The prescribed SST dataset is derived from the merged Hadley optimum interpolation (OI) SST and sea ice concentration (SIC) dataset (Hurrell et al., 2008). Each experiment is integrated for 25 years, with the first 5 years discarded to avoid model drift; the climatology derived over the last 20 years is used for the analysis presented here.

For the idealized simulations (section 3.8), we use the F_IDEAL_PHYS component,

that is, the finite volume dynamical core of CAM5, which is based on the model described by Held & Suarez (1994). This idealized physics configuration is hemispheric and zonally symmetric, with neither a seasonal cycle nor land–sea contrast. It employs a Newtonian relaxation toward a prescribed zonal mean radiative equilibrium temperature profile to represent radiative cooling, with a relaxation time scale of 40 days. There is neither moisture nor diabatic heating in the dry dynamical core, which allows us to neglect the possible effects of the sensible heating and condensational heating on the atmospheric circulation. We introduce the Tibetan Plateau in the model by setting the surface geopotential over 25° to 45° N, 60° to 105° E to today's value. To obtain a relatively localized plateau, elevations lower than 500 m in the region are set to zero. We shift the plateau meridionally to perturb relative positioning between westerlies and orography; by doing so, we mimic the seasonal migration of the westerly jet across the plateau. We undertake five simulations, namely Plateau, PlateauN3, PlateauN6, PlateauS3, and PlateauS6. The "Plateau" simulation is the case where the Tibetan Plateau is fixed at its present location, while the other cases represent scenarios where the plateau is shifted northward or southward by 3° or 6°. Each simulation is integrated for 5 years, with 30 levels in the vertical, at a horizontal resolution of $0.9° \times 1.25°$ (as with the northward-extended plateau simulations). An initial spinup period of 2 years is discarded, leaving 3 years of data for analysis.

For the boundary orography in the CAM5, the resolved grid scale component is the mean elevation in each grid box (i.e., the surface geopotential). The unresolved subgrid-scale orography is parameterized as the turbulent mountain stress (TMS) and the gravity wave drag (GWD) (Neale et al., 2010). In our simulations with both modified resolved and modified subgrid topography, the subgrid-scale variances needed for TMS and GWD parameterizations were derived from the modified resolved topography (e.g., Fig. B.1) using the NCAR Global Model Topography Generation Software (Lauritzen et al., 2015). Thus, the subgrid-scale variances are modified to be consistent with the modified resolved topography.

3.3 Termination of mei-yu in climatology

In this section, we show that the mei-yu termination in observed climatology is accompanied by the migration of core westerlies impinging on the Tibetan Plateau to the north of 40° N and the disappearance of northerlies in northeastern China (35° to 45° N, 110° to 120° E).

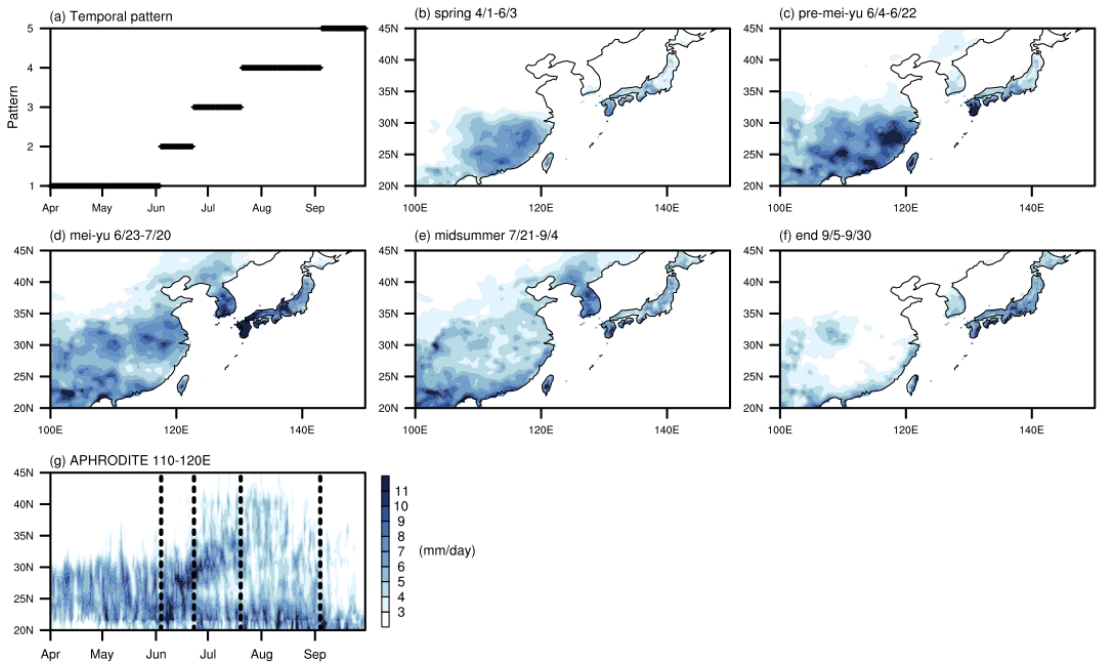

Figure 3.1: Climatology of the 1979–2007 APHRODITE daily precipitation rate ($\mathrm{mm\,d^{-1}}$) in East Asia. (a) Temporal and (b)–(f) spatial patterns of EASM derived from the SOM analysis of the APHRODITE dataset. Patterns 1–5 [shown in (b)–(f)] are respectively the spring persistent rainfall (1 Apr–3 Jun), pre-mei-yu (4–22 Jun), mei-yu (23 Jun–20 Jul), midsummer (21 Jul–4 Sep), and retreat of the EASM (5–30 Sep). (g) Hovmöller diagram of precipitation rate averaged from 110° to 120° E. Dashed lines in (g) denote timings of seasonal transitions based on the SOMs analysis.

3.3.1 Identification of mei-yu termination in climatology

Figure 3.1g presents the temporal evolution of the climatological precipitation over eastern China (110° to 120° E), with dashed lines indicating timings of the rainfall stages derived

from the SOMs analysis of the APHRODITE data (Fig. 3.1a). Figure 3.1a shows the temporal extent of each of the five rainfall patterns illustrated in the remaining panels, namely spring (pattern 1; Fig. 3.1b), pre-mei-yu (pattern 2; Fig. 3.1c), mei-yu (pattern 3; Fig. 3.1d), midsummer (pattern 4; Fig. 3.1e), and fall (pattern 5; Fig. 3.1f). Observational studies (Ding & Chan, 2005; Tao & Chen, 1987) suggest that the typical mei-yu season lasts from mid-June to mid-July. The SOM-captured timing of the mei-yu spans the interval from 23 June to 20 July, approximately matching this reported timing. For spatial patterns, the SOM-derived mei-yu covers the Yangtze River valley (27° to 34° N, 100° to 120° E), which is consistent with the previously defined domain (Ding & Chan, 2005).

The mei-yu front is characterized by a strong meridional moisture gradient (Chen & Chang, 1980; Ding, 1992) and can be identified from sharp meridional gradients in equivalent potential temperature θ_e (Ninomiya, 1984, 2000; Ninomiya & Shibagaki, 2007). Figure 3.2 shows the meridional gradient of θ_e $[-(\frac{\partial \theta_e}{\partial y})]$. Here, θ_e is approximately defined as $\theta_e = \theta + L_v q/C_p$ (Shaw & Pauluis, 2012), and the largest values of $-(\frac{\partial \theta_e}{\partial y})$ indicate the location of the front. We interpret the latitudinal migration of the band of strong gradient to indicate the meridional movement of the frontal system. Figure 3.2a presents the seasonal evolution of $-(\frac{\partial \theta_e}{\partial y})$ over East China (110° to 120° E) at 850 mb. It shows that the maximum gradient, and hence the front, migrates northward during the mei-yu and disappears by midsummer. Vertical cross sections further show weakening of the front in central eastern China (30° to 35° N, 110° to 120° E) from mei-yu to midsummer (Figs. 3.2b,c). Figures 3.2d-e depict the meridional moisture gradient and suggest that the moisture contrast over central eastern China weakens from mei-yu to midsummer.

Strong midtropospheric (500mb) ascending motion over central eastern China is also thought to be representative for the mei-yu season (Sampe & Xie, 2010). Figure 3.3a shows the ascending motion at 500mb and suggests that our SOM analysis accurately captured the mei-yu and midsummer stages. Both spatial distribution (Figs. 3.3b,c) and vertical cross sections (Figs. 3.3d,e) further indicate significant weakening of the ascending motion over central eastern China from mei-yu to midsummer.

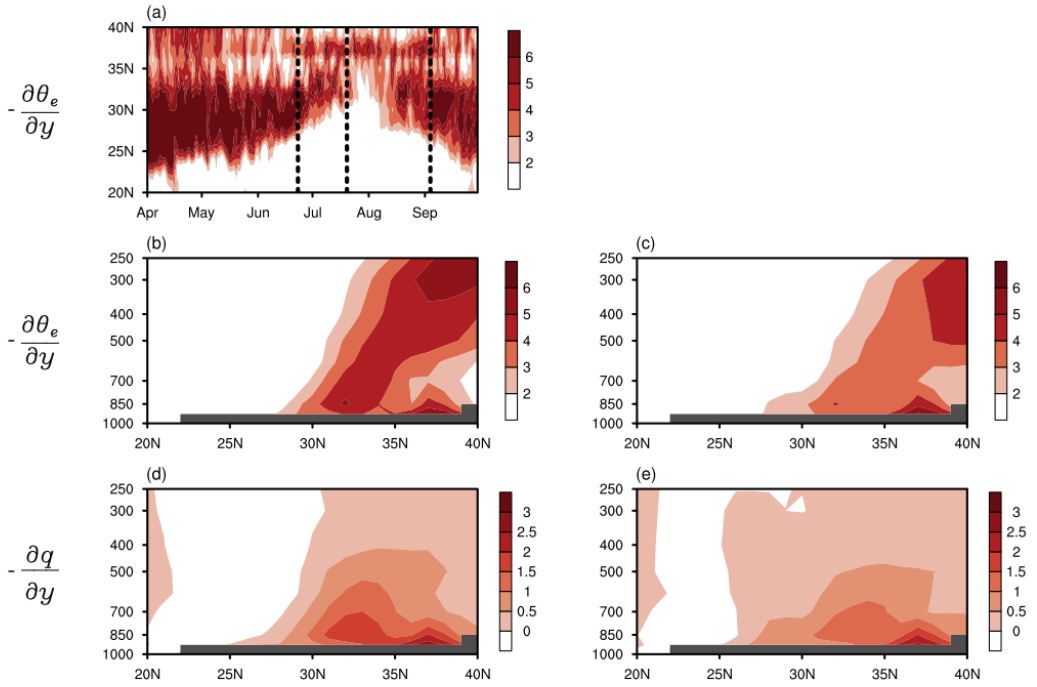

Figure 3.2: Climatological meridional gradient of equivalent potential temperature $[-(\frac{\partial \theta_e}{\partial y})]$ $(3 \times 10^{-6}\,\mathrm{K\,m^{-1}})$ and specific humidity $[-(\frac{\partial q}{\partial y})]$ $(3 \times 10^{-9}\,\mathrm{kg\,kg^{-1}\,m^{-1}})$. Black dashed lines indicate SOM-derived timings for mei-yu and midsummer. Also shown are vertical cross sections of $-(\frac{\partial \theta_e}{\partial y})$ over 110° to 120° E in (b) mei-yu and (c) midsummer and vertical cross sections of $-(\frac{\partial q}{\partial y})$ over 110° to 120° E in (d) mei-yu and (e) midsummer.

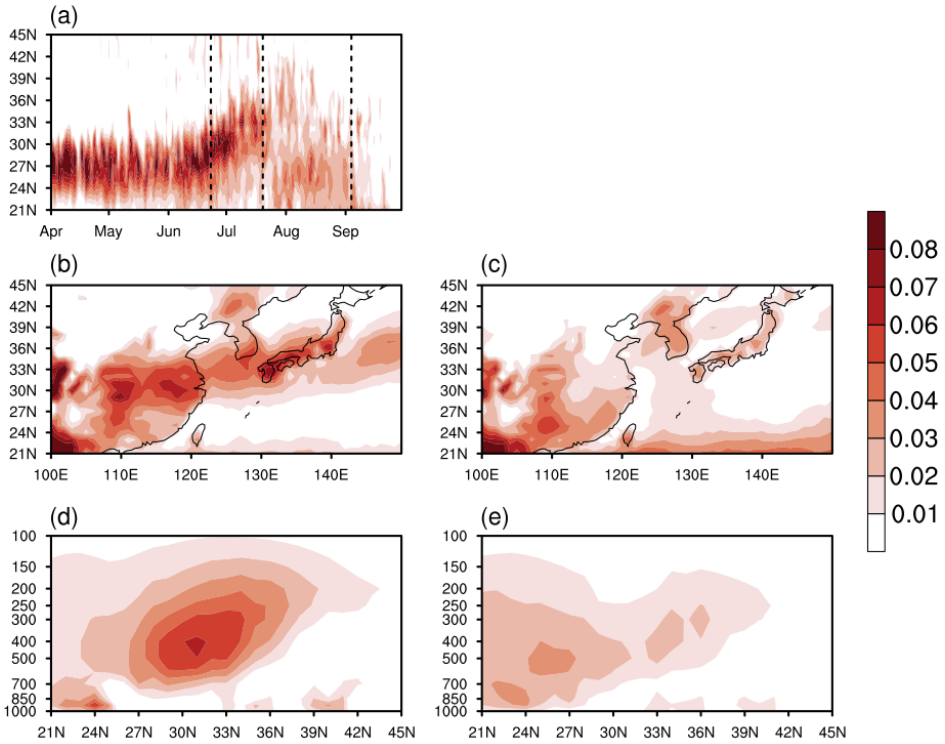

Figure 3.3: Climatological vertical velocity ω ($-$Pa/s) over 1979–2007. (a) Hovmöller diagram of ω at 500 mb in East China (110° to 120° E). Black dashed lines indicate SOM-derived timings for mei-yu and midsummer. Also shown are spatial patterns of ω at 500 mb in (b) mei-yu and (c) midsummer, and vertical cross sections of v over 110° to 120° E in (d) mei-yu and (e) midsummer. Warm color indicates ascent.

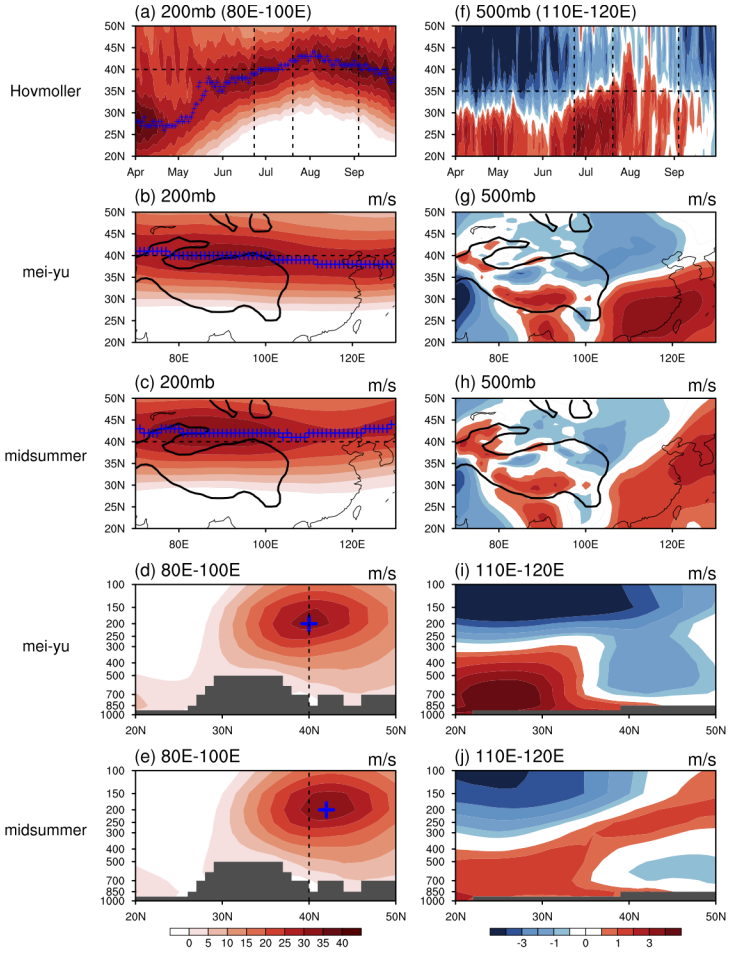

Figure 3.4: (left) Zonal wind and (right) meridional wind characteristics over East Asia associated with the mei-yu and midsummer stages (unit: $\mathrm{m\,s^{-1}}$). Hovmöller diagram of (a) zonal wind at 200 mb averaged over 80° to 100° E and (f) meridional wind at 500 mb averaged over 110° to 120° E; vertical dashed lines in (a) and (f) indicate SOM-derived timings for mei-yu and midsummer, and blue crosses in (a) indicate the latitude position of maximum westerlies for each day. Also shown are maps of (b),(c) zonal wind at 200 mb and (g),(h) meridional wind at 500 mb, for mei-yu in (b) and (g) and midsummer in (c) and (h), and pressure–latitude (20° to 50° N) cross sections of (d),(e) zonal wind averaged over 80° to 100° E and (i),(j) meridional wind averaged over 110° to 120° E, for mei-yu in (d) and (i) and midsummer in (e) and (j). Gray shadings indicate zonally averaged topography in (d) and (e) over 80° to 100° E and (i) and (j) over 110° to 120° E. Black contours in (b), (c), (g), and (h) indicate an elevation of 2000 m.

3.3.2 Threshold latitude of jet for the mei-yu termination

Figure 3.4a shows the seasonal migration of 200 mb westerlies averaged over 80° to 100° E, where the plus sign (+) symbol indicates the latitude of maximum westerlies. Resembling

model results from Kong et al. (2017) but now from observational data, the mean jet axis over the plateau is located at 40° N for most of the mei-yu season (Fig. 3.4a); it then migrates a few degrees northward during the transition from mei-yu to midsummer and stays at 42° or 43° N for most of midsummer before retreating southward in late August. Figures 3.4b–e further depict the distinct shift of jet axis over the plateau from 40° N in mei-yu to around 42° N in midsummer. It suggests that 40° N marks a latitudinal threshold for the termination of mei-yu.

3.3.3 Changes in orographic downstream northerlies from mei-yu to midsummer

Previous studies suggested that the meridional wind plays an important role in the formation of the mei-yu (Chen & Bordoni, 2014; Park et al., 2012). Figures 3.4f–j show variations of midtropospheric meridional wind from mei-yu to midsummer. During the spring and pre- mei-yu stages, the extratropical northerlies are strong and converge with the tropical southerlies along 30° N over eastern China. The northerlies weaken and retreat to the north of 35° N during the mei-yu stage, while the southerlies become stronger and penetrate northward. During midsummer, the extratropical northerlies almost disappear, while the tropical southerlies penetrate to around 40° N. Similar variation can be seen in the meridional winds at 700 mb (not shown).

3.4 Termination of the mei-yu on interannual and synoptic time scales

In this section, we seek a more rigorous examination of the link between jet latitude, weakening of northerlies over northeastern China, and termination of the mei-yu on interannual and synoptic time scales.

3.4.1 Termination of the mei-yu on interannual time scales

The leading mode of summertime rainfall over East Asia exhibits a tripole pattern with rainfall over northern and southern China varying out of phase with rainfall over central China (Hsu & Lin, 2007). Chiang et al. (2017) identified the leading mode of interannual variability of East Asian summer rainfall over 1951–2007 by deriving an empirical orthogonal function (EOF) from July–August APHRODITE rain gauge data (Fig. B.2). They attributed one phase of the tripole pattern—with wet northern and southern China and dry central China—to a significantly earlier termination of the mei-yu, accompanied by a shorter mei-yu duration and longer midsummer stage. They found that the years with earlier mei-yu termination are associated with earlier northward migration of westerlies over the Tibetan Plateau.

Here, we examine the linkage between the jet positioning, strength of northerlies, and the mei-yu in the context of the interannual variation of mei-yu termination. We select anomalous high and low years based on the first principal component of Chiang et al. (2017) (Fig. B.2b), but limited to 1979–2007, which is the time span of the ERA-Interim data we use. We identify 7 high years and 9 low years based on the principal component exceeding $+/-0.5$ standard deviations. For each group of years, we compute the daily climatological rainfall between April and September, and applied a 9-day running average. To find the corresponding rainfall stages, we assign the averaged rainfall for each day to a best- matching climatological SOM rainfall pattern (Figs. 3.1b–f) based on the minimum Euclidean distance between each daily pattern and each of the SOM patterns. Similar to Chiang et al. (2017), the matched timing for high and low years suggests that the mei-yu in low years terminates three weeks later than in high years (Figs. 3.5a,b).

Hovmöller diagrams of the meridional gradient of θ_e (Figs. 3.5c,d) and midtropospheric ascending motion (Figs. 3.5e,f) suggest that the mei-yu stages identified by the SOM analysis are reliable for both categories. Mei-yu stages of both high and low years are accompanied by sharp gradients of θ_e over central eastern China; termination of the mei-yu is accompanied by weakening of the gradient of θ_e and northward migration of the maximum gradient to north of 35° N, which is however more evident in the lower years than the high years. Similarly, both high and low years exhibit significant weakening of midtropospheric ascending motion over central eastern China when the mei-yu ends (Figs. 3.5e,f).

The associated behaviors of the jet latitude over the plateau and northerlies over eastern China for both composites are consistent with the climatology. The main feature to note is that the jet axis remains at 40° N during the mei-yu stage for both high and low years; this is despite the fact that the mei-yu stage has significantly longer duration in low years compared to the high years. Prior to the mei-yu, the jet axis is south of 40° N in both cases; after the mei-yu, the jet axis shifts north of 40° N (Figs. 3.5g,h). On the other hand, a weakening and retreat of the northerlies, and increased northward penetration of southerlies, appears at the transition from mei-yu to midsummer for both high and low years (Figs. 3.5i,j). It is worth noting that the southward retreat of westerlies toward the end of the summer monsoonal season is accompanied by a recurrence of northerlies in northeastern China, suggesting a causal link between the jet axis position relative to 40° N and the sign and strength of northerlies downstream of the plateau.

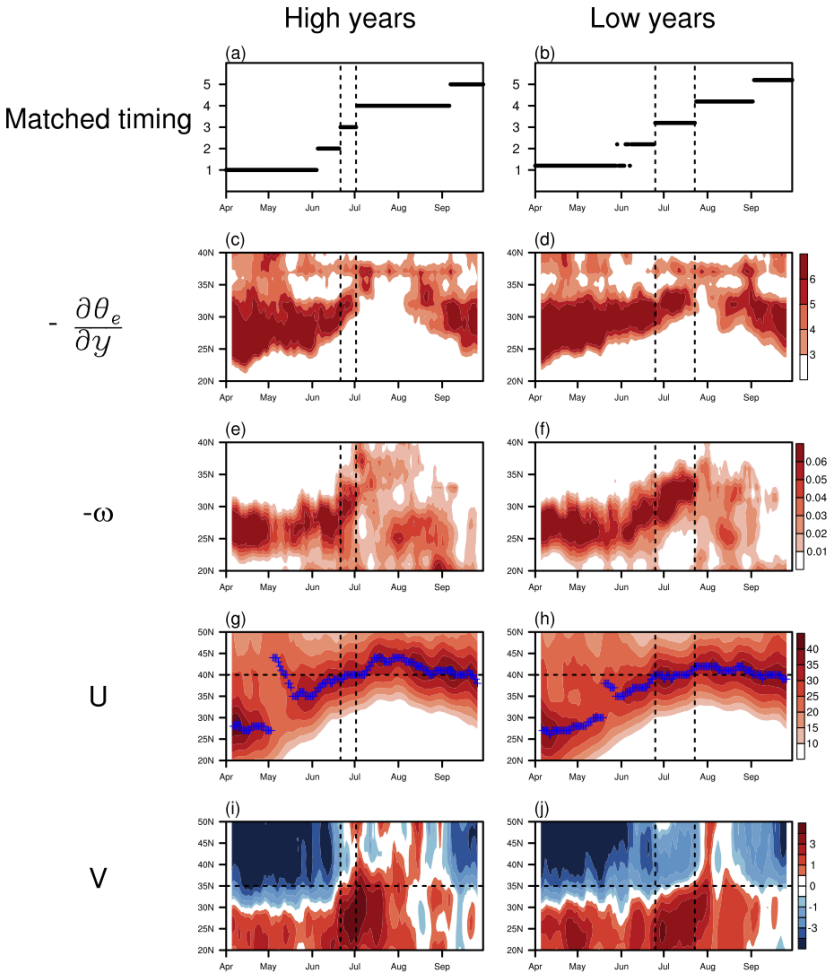

Figure 3.5: Matched timings for 9-day running averaged daily climatology, for (a) high years and (b) low years. The y axes in (a) and (b) label spring as 1, pre-mei-yu as 2, mei-yu as 3, midsummer as 4, and the end of the EASM season as 5. Also shown are Hovmöller diagrams for (left) high years and (right) low years: (c),(d) meridional gradient of 850-mb equivalent potential temperature $[-(\frac{\partial \theta_e}{\partial y})]$ averaged over 110° to 120° E ($3 \times 10^{-6}\,\mathrm{K\,m^{-1}}$); (e),(f) ascending motion averaged over 110° to 120° E at 500 mb (−Pa/s); (g),(h) zonal wind at 200 mb averaged over 80° to 100° E ($\mathrm{m\,s^{-1}}$); and(i), (j) meridional wind at 500 mb averaged over 110° to 120° E ($\mathrm{m\,s^{-1}}$). Black dashed lines in the left panel indicate the matched mei-yu period for high years, and black dashed lines in the right panel indicate the matched mei-yu period for low years. To remove weather noise, we applied a 9-day running mean to fields shown in (c)–(j).

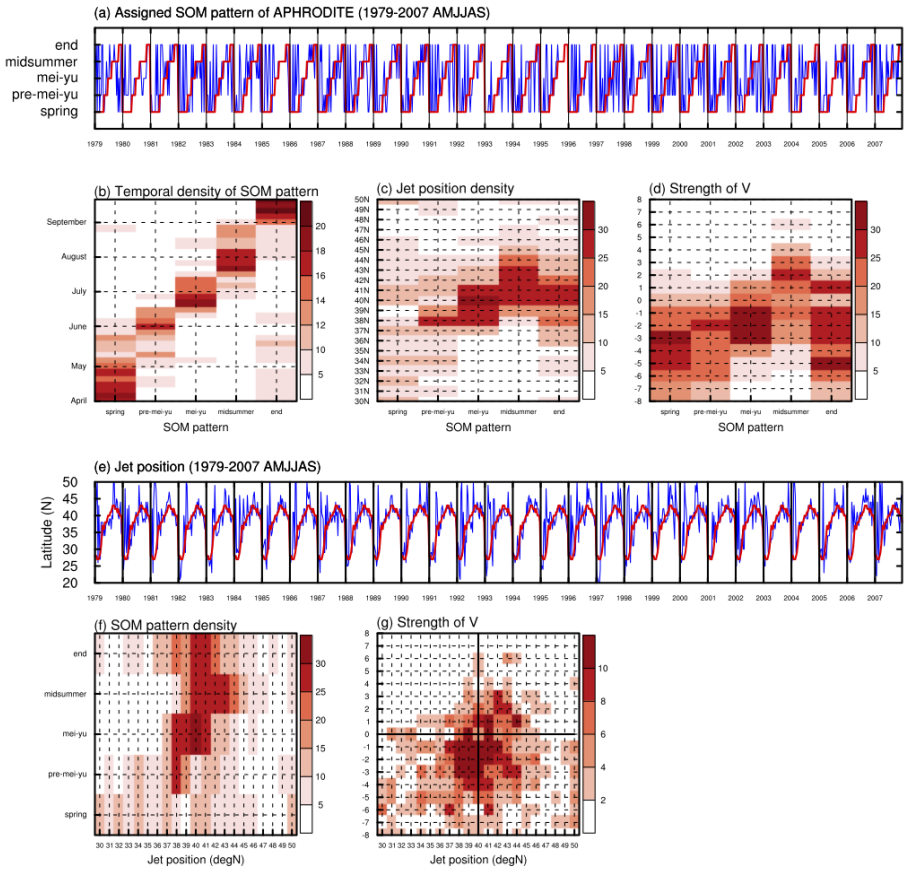

Figure 3.6: (a) Timings of matched SOM patterns for each pentad from 1 Apr through 27 Sep in 1979–2007 (blue lines), overlaid with climatological SOM patterns (red lines). (b) Temporal density of matched SOMs patterns shown in (a); for each pentad at the y axis, color for a corresponding SOMs pattern indicates the number of pentads in 1979–2007 April–September that are matched to that pattern. (c) Density of jet positions, where jet position is defined as latitude of maximum westerlies at 200 mb in the Tibet region; for each SOM pattern, colors indicate the number of pentads when the jet is located at a certain latitude. (d) Density of the strength of meridional wind at 500 mb averaged over 110° to 120° E, 35° to 40° N; for each SOM pattern, colors indicate the number of pentads when the strength of meridional wind is within a certain range as indicated on the y axis. (e) Jet position for each pentad in April through September from 1979 to 2007 (blue lines), overlaid with climatological jet position in 1979–2007. (f) SOM pattern density; for each jet position, colors indicate the number of corresponding pentads that are matched to a certain SOM pattern. (g) Density of strength of V; for each jet position, colors indicate the number of pentads when the strength of V falls in a certain interval as indicated on the y axis. Note that (f) is identical to (c) by construction; we show both here for clarity.

3.4.2 Termination of the mei-yu on synoptic time scales

Although the climatological westerlies exhibit a continuous northward migration from spring to summer (Figs. 3.4a and Figs.3.5g,h), on synoptic time scales the jet exhibits large and rapid latitudinal excursions (Schiemann et al., 2009). This observation raises the question of whether the connection between the jet position, strength of northerlies, and occurrence of mei-yu-like regimes holds on synoptic time scales.

To test this, we assign each pentad from 1 April (pentad 19) to 27 September (pentad 54) for each year over 1979–2007 (a total of 1044 pentads) to the best-matched climatological SOM rainfall pattern based on the minimum Euclidean distance. This allows us to identify mei-yu-like pentads and to examine the associated circulations. In contrast to the smooth climatological timing of each pattern (red lines in Fig. 3.6a), the SOM-matched patterns on the pentad basis from each year exhibit large varia- tions (blue lines in Fig. 3.6a). Figure 3.6b shows the seasonal distribution of the assigned SOM patterns of the 1044 pentads. Specifically for the mei-yu pattern, Fig. 3.6b suggests that mei-yu-like rainfall regimes could occur in spring or late summer, but are relatively rare at these times. Mid-June to mid-July is the period when the mei-yu-like rain pattern most likely occurs.

We now discuss distributions of the jet axis impinging on the plateau (Fig. 3.6c) and strength of meridional winds over northeastern China (Fig. 3.6d). On the pentad scale, mei-yu-like patterns are most closely associated with jet axes ranging from 38° to 41° N, whereas midsummer-like pentads are associated with jet axes between 40° and 43° N. For the strength of the 500-mb meridional wind over northeastern China, Fig. 3.6d suggests that northerly winds (negative values) are strongest when the rainfall is spring-like or pre-mei-yu-like; the northerlies tend to be weaker for mei-yu-like patterns. For midsummer-like patterns, the 500-mb meridional winds are both northerly and southerly, with a preference for the latter. These findings suggest that the synoptic relationships between the jet positions, the strength of northerlies, and the rainfall stage are in general agreement with the ones inferred from the climatology.

We now examine the question from the opposite perspective. If we classify all 1044 pentads based instead on their positioning of the jet axis over the plateau, can we see weaker orographic downstream northerlies and midsummer-like rain patterns during pentads when the jet axis locates to the north of 40° N, and vice versa? Figure 3.6e—which shows the jet latitude between April and September for each year from 1979 to 2007—indicates that jet latitude exhibits large synoptic variability about the climatological migration latitude (shown in red). There are overlaps in the jet latitudes between the mei-yu- like pentads and the midsummer-like pentads when the jet latitude is associated with the corresponding rainfall stage (Fig. 3.6f; note that Fig. 3.6f is identical to Fig. 3.6c, although they are generated based on different approaches), suggesting that the correlation between the position of the jet and the mei-yu/midsummer regimes is not as tight as that on climatological (Fig. 3.4) and interannual time scales (Fig. 3.5). Regardless, the close synoptic relationship between the two is evident, namely that when the jet axis is between 38° and 41° N, the corresponding rainfall patterns are mei-yu-like, whereas jet axes occupying the interval bounded by 40°

and 43° N are midsummer-like. Likewise, when the jet latitude is associated with the corresponding value of the 500-mb meridional wind, northeastern China more likely experiences northerlies when jet axes are south of 40° N, whereas southerlies more likely appear in the region when the jet is north of 40° N (Fig. 3.6g).

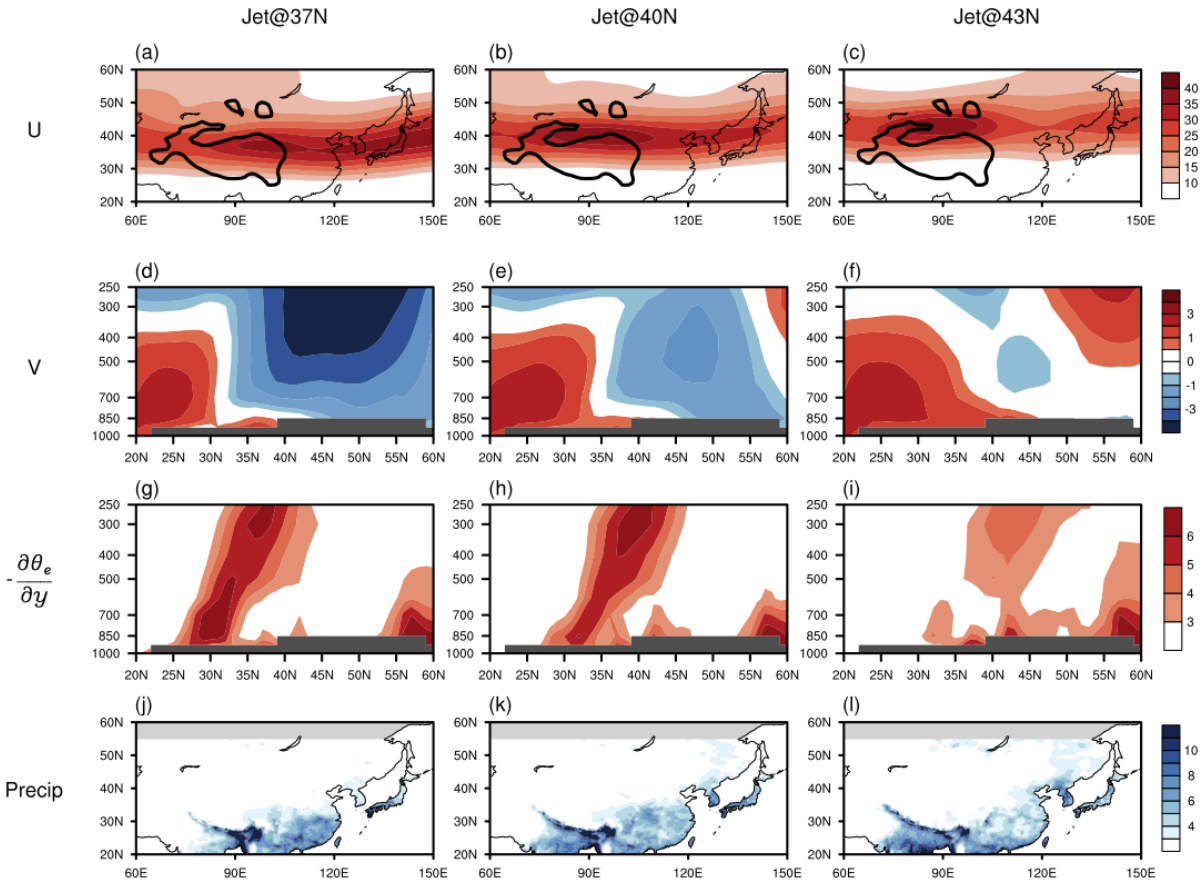

Figure 3.7: Composites based on pentads when latitude of the zonal wind maximum impinging on the Tibetan Plateau is (left) 37° N, (center) 40° N, and (right) 43° N. The pentads are taken from April through September, for years 1979–2007. (a)–(c) Zonal wind at 200 mb ($\mathrm{m\,s^{-1}}$). (d)–(f) Meridional wind at 500 mb ($\mathrm{m\,s^{-1}}$) averaged from 110° to 120° E. (g)–(i) Meridional gradient of equivalent potential temperature $[-(\frac{\partial \theta_e}{\partial y})]$ ($3 \times 10^{-6}\,\mathrm{K\,m^{-1}}$) from 110° to 120° E. (j)–(l) APHRODITE rain gauge data ($\mathrm{mm\,d^{-1}}$). Black contours in (a)–(c) indicate an elevation of 2000 m.

Composites of pentads when the jet axis is located at 37°, 40°, and 43° N are shown in Fig. 3.7. These composites confirm that the northerlies over northeastern China significantly weaken as the jet migrates from positions over the plateau to north of the plateau (Figs.

3.7a–f). The weakening of the meridional gradient of θ_e (Figs. 3.7g–i) and ascending motion (not shown) are all paced with the weakening of the northerlies. Finally, the pattern of rainfall extends northward with a more northward mean jet axis (Figs. 3.7j–l).

3.5 Connections between northerlies and mei-yu termination

In this section, we explore the dynamical connection between the disappearance of lower-to-midtropospheric northerlies and the mei-yu termination.

3.5.1 General discussion

One view of how the northerlies maintain the mei-yu is that they advect cold, dry air southward, meeting with the warm, moist southerly flow and forming a steep moisture gradient over central China characteristic of the mei-yu front. The northerlies essentially disappear when the mei-yu ends, leading to the demise of the strong moisture contrast (Fig. 3.2). This view is in agreement with previous findings on the close connection between the mei-yu and cold air mass associated with northerlies (Li & Zhang, 2014; Seo et al., 2015; Tomita et al., 2011).Park et al. (2012) found that the mei-yu is associated with southward low moist static energy (MSE) flux (integrated from the surface to 600 mb) over northeastern China and northward high MSE flux over southeastern China. In this vein, the mei-yu terminates when the southward low MSE air disappears with northerlies. Chou & Neelin (2003) argued that advection of low MSE air over the northern reaches of monsoon regions limits the northward extent of summer monsoons, through the so-called ventilation effect. In a similar vein, the advection of low MSE air by the northerly flow limits the northward extent of the rainfall over eastern China (Figs. 3.8a–c); as such, rainfall shifts to northeastern China in midsummer as the northerly flow retreats.

The northerlies are also crucial for the mei-yu formation through maintaining strong meridional wind convergence. Simulations with and without the Tibetan Plateau by Chen & Bordoni (2014) suggest that the presence of the Tibetan Plateau and the resultant orographic downstream meridional wind convergence is key to the formation of mei-yu. Figures 3.8d–f show that meridional wind convergence over central eastern China is indeed considerably stronger in the mei-yu than in midsummer. It is worth noting that seasonal variation of meridional wind convergence over central eastern China (Fig. 3.8d) resembles the rainfall seasonality (Fig. 3.1g), indicating close connection between the two. As will be shown in the section 3.5.2, weakening of the meridional wind convergence dominates the reduction of moisture flux convergence associated with mei-yu termination.

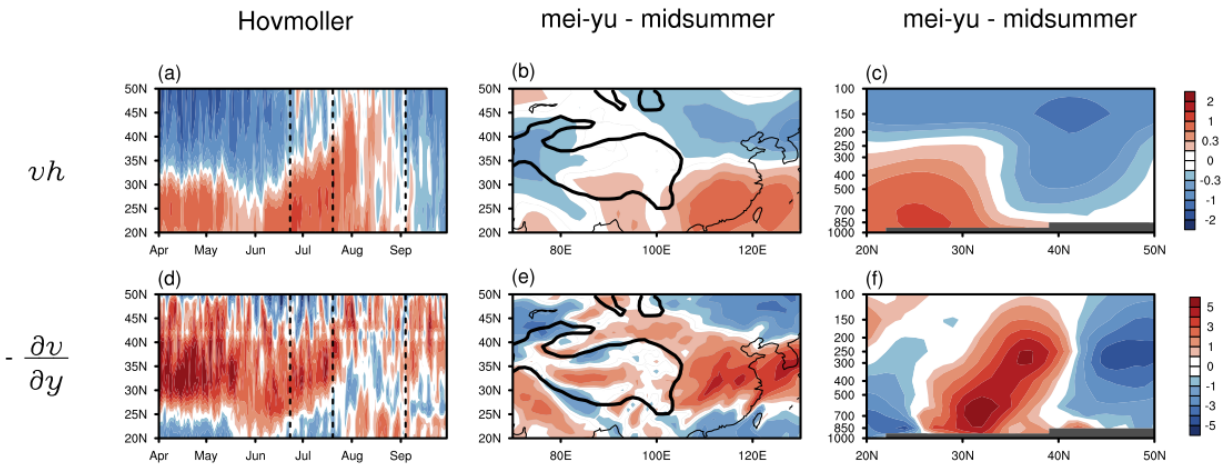

Figure 3.8: (top) The meridional MSE flux (vh; $h = C_pT + L_vq + gz$) and (bottom) the meridional wind convergence $[-(\frac{\partial v}{\partial y})]$. Results are shown for (a),(d) Hovmöller diagram of vertical integrations (1000–250 mb) averaged over 110° to 120° E, (b),(e) differences of vertical integrations (1000–250 mb) between mei-yu and midsummer (mei-yu minus midsummer), and (c),(f) differences of averaged values over 110° to 120° E between mei-yu and midsummer (mei-yu minus midsummer). Units are $10^6\,\mathrm{W\,m^{-1}}$ in (a) and (b), $10^6\,\mathrm{W\,m\,s^{-1}}$ in (c), $10^{-3}\,\mathrm{kg\,m^{-2}\,s^{-1}}$ in (d) and (e), and $10^{-6}\,\mathrm{s^{-1}}$ in (f). Gray shadings in (c) and (f) indicate zonally averaged topography over 110° to 120° E. Black contours in (b) and (e) indicate an elevation of 2000 m.

3.5.2 Moisture budget analysis

We explicitly show the role of meridional wind anomalies on rainfall changes associated with mei-yu termination through a vertically integrated moisture budget analysis. We follow Chen & Bordoni (2016) and employ moisture budget analysis to diagnose contributions to the moisture flux convergence. In long-term average, the moisture budget can be written as

$$\overline{P} - \overline{E} = -\overline{\langle \nabla \cdot (\mathbf{v} \cdot q) \rangle}, \tag{3.1}$$

where P is precipitation, E is evaporation, $\mathbf{v}$ indicates horizontal winds, and q is specific humidity; $\overline{(\cdot)}$ indicates temporal mean, while $\langle \cdot \rangle$ indicates the mass-weighted vertical integral from 1000 to 100 mb. Contribution to the vertically integrated moisture flux convergence by submonthly transient eddies is calculated from

$$trans = \overline{\langle \nabla \cdot (\mathbf{v} \cdot q \rangle} - \nabla \cdot (\overline{\mathbf{v}}\ \overline{q}). \tag{3.2}$$

Changes (δ) of vertically integrated moisture flux convergence between mei-yu and midsummer in climatology can be written as

$$\delta(\overline{P} - \overline{E}) = -\delta\{\overline{\langle \nabla \cdot (\mathbf{v} \cdot q) \rangle}\} = -\delta\{\langle \nabla \cdot (\overline{\mathbf{v}}\ \overline{q}) \rangle\} - \delta(trans), \tag{3.3}$$

where δ indicates mei-yu minus midsummer. Equation (3.3) can be written as below by further decomposition of the term $-\delta\{\overline{\langle \nabla \cdot (\mathbf{v} \cdot q) \rangle}\}$:

$$\underbrace{-\delta\{\overline{\langle \nabla \cdot (\mathbf{v} \cdot q) \rangle}\}}_{\text{A}} = \underbrace{-\langle \nabla \cdot (\overline{\mathbf{v}} \cdot \delta\overline{q}) \rangle}_{\text{B}} \underbrace{-\langle \nabla \cdot (\delta\overline{\mathbf{v}} \cdot \overline{q}) \rangle}_{\text{C}} \underbrace{-\langle \nabla \cdot (\delta\overline{\mathbf{v}} \cdot \delta\overline{q}) \rangle}_{\text{D}} \underbrace{-\delta(trans)}_{\text{E}}, \tag{3.4}$$

where term A indicates changes of vertically integrated moisture flux convergence, term B is contribution by changes to the specific humidity, term C is contribution by changes to the horizontal winds, term D is contribution by changes to both specific humidity and horizontal winds, and term E is contribution by submonthly transients. Note that variables without d in terms B and C represent midsummer. Seager & Henderson (2013) noted that the divergence of the vertically integrated moisture transport does not balance the ERA-Interim $P - E$, possibly from the influence of the data assimilation. We find slight difference between the magnitude of $\delta(P - E)$ and term A, but the patterns between the two match well (not shown).

Figures 3.9a–e shows terms A–E of Eq. (3.4), respectively, for the difference between the mei-yu and midsummer averages, in order to examine changes occurring to the components of the moisture flux budget between these intraseasonal stages. Not surprisingly, the mei-yu season exhibits enhanced moisture transport and moisture flux convergence over central eastern China (Fig. 3.9a). This enhancement is dominated by changes of horizontal winds (Fig. 3.9c), while the contribution by changes of specific humidity is minimal (Fig. 3.9b). Contributions by the cross-perturbation term (Fig. 3.9d) and the submonthly transient eddies (Fig. 3.9e) are negligible. Decomposing contributions by the horizontal winds (Fig. 3.9c) to its zonal (Fig. 3.9f) and meridional components (Fig. 3.9g) indicates that changes in the meridional wind are essential to changes of the total moisture flux convergence. Contributions by the meridional winds could be further decomposed as follows: $-(\frac{\partial(\delta v q)}{\partial y}) = -(\frac{\partial \delta v}{\partial y})q - \delta v(\frac{\partial q}{\partial y})$, where $-(\frac{\partial \delta v}{\partial y})q$ is contribution by changes in meridional wind convergence, while $-\delta v(\frac{\partial q}{\partial y})$ is the contribution by changes in the meridional advection of moisture. Figures 3.9h-i indicate

that although both terms positively contribute to the moisture flux convergence, changes of meridional wind convergence play the dominant role.

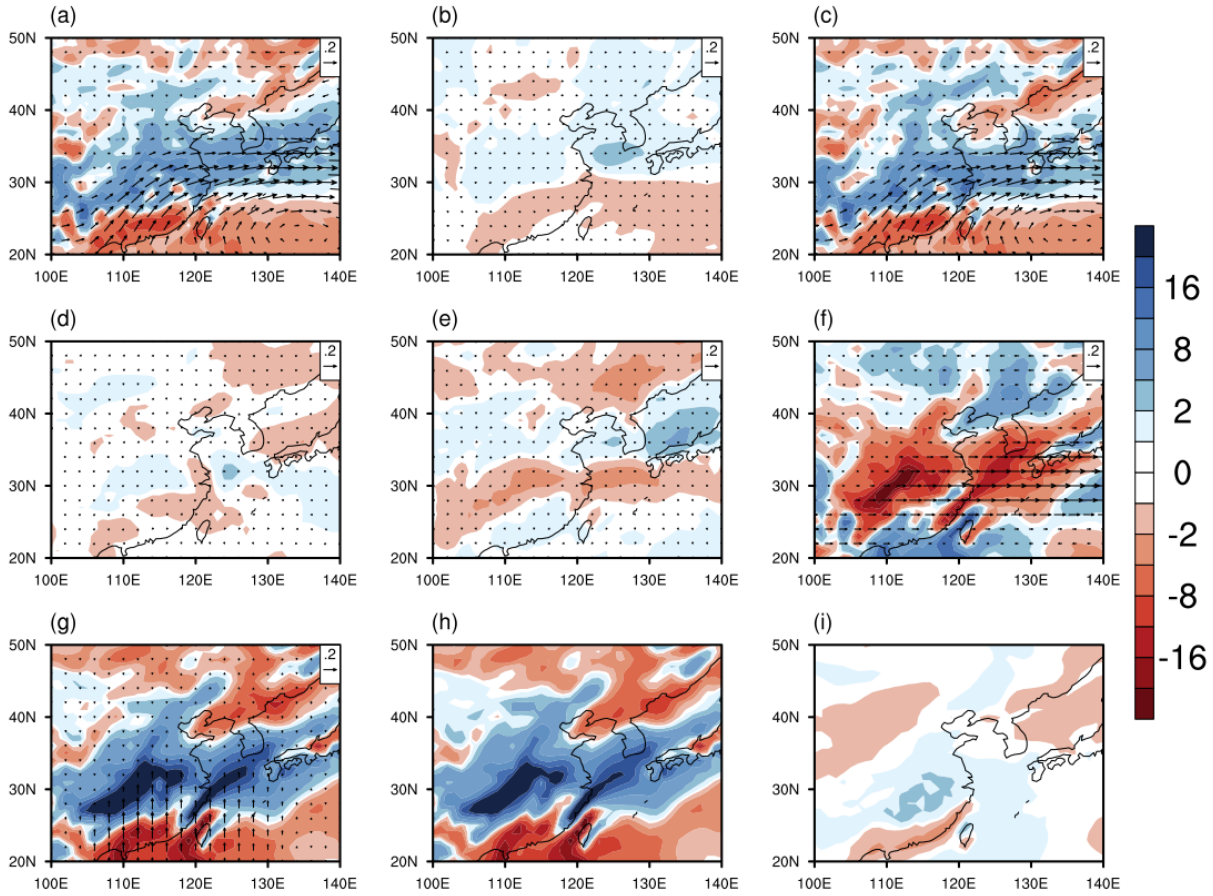

Figure 3.9: Climatological changes in the mass-weighted vertical integral (from 1000 to 100 mb) of moisture budget components between mei-yu and midsummer (mei-yu minus midsummer). Vectors denote moisture fluxes ($m^2\,s^{-2}$), and color shadings denote moisture flux convergence ($mm\,d^{-1}$; cold color indicates convergence, and warm color indicates divergence). (a) Changes of moisture flux and its convergence. (b) Contributions by the changes of specific humidity. (c) Contributions by changes of horizontal winds. (d) Contributions by changes of both specific humidity and horizontal winds. (e) Contributions by changes of transients. (f) Contributions by changes to the zonal moisture flux and its convergence. (g)–(i) Contributions by changes to the meridional moisture flux and its convergence; (g) is contributed from two terms, with (h) showing the contributions by meridional wind convergence and (i) showing contributions by meridional advection of moisture.

We repeat the above analysis but in the context of the tripole mode of East Asian rainfall interannual variability, using again the high and low year composites defined in section 3.4;

we refer to changes δ as low years minus high years. We focus on the gap in the timings of mei-yu termination between high and low years (i.e., 3–23 July). During this period, high years are already in the midsummer stage, while low years are still in mei-yu. The results (Fig. 3.10) show strong qualitative similarity to the analysis of Fig. 3.9 for the difference between mei-yu and midsummer stages, and reinforce the conclusions drawn from Fig. 3.9. Figure 3.10a shows enhanced moisture flux convergence over central China in low years relative to high years. The resemblance among Figs. 3.10a, c, g, h highlight the crucial role of meridional wind convergence in changes of total moisture flux convergence during the period when high years are in midsummer while low years are still in mei-yu.

3.5.3 Relative contributions from northerlies and southerlies

The moisture budget analysis above clearly shows the central role of meridional wind changes in mei-yu termination. We have focused on the role of the extratropical northerlies, but one might argue that variations of the southerlies also contribute to the mei-yu termination. On average, southerlies over eastern China are indeed weaker in midsummer, although this weakening is mainly limited to south of 30° N (Figs. 3.4g–j). Figure 3.9g also suggests the southerly moisture flux dominates contribution to the enhanced moisture flux convergence in mei-yu. However, the moisture budget analysis is diagnostic, so the southerlies can be, in part, interpreted as a feedback. In particular, diabatic heating from the mei-yu rainband and consequent vortex stretching will lead to a southerly flow because of Sverdrup vorticity balance (Rodwell & Hoskins, 2001). Furthermore, Fig. 3.4f shows that the most striking change in the meridional circulation associated with the mei-yu termination is disappearance of extratropical northerlies and northward penetration of southerlies. It suggests that weakening of the northerlies is the root cause of the transition from mei-yu to midsummer.

On shorter time scales, Fig. 3.10 suggests stronger and more persistent southward moisture flux, associated with enhanced northerlies, dominates the enhanced moisture flux convergence in low years during 3–23 July. Further, our composites of meridional wind at pentads with different jet positions clearly show the weakening of extratropical northerlies when the jet is located north of the plateau (Figs. 3.7d–f). However, there is no evident change in the strength of tropical southerlies among these composites.

We note in closing that relative roles of tropical southerlies and extratropical northerlies are still in debate. A recent idealized study by Son et al. (2019) suggests that orographic downstream southerlies are most crucial for the EASM. Tomita et al. (2011) and Suzuki & Hoskins (2009) suggest that the closing dates of baiu (the Japanese sector of the mei-yu–baiu rain belt) could be modified by the combined effects of both tropical and midlatitude circulations.

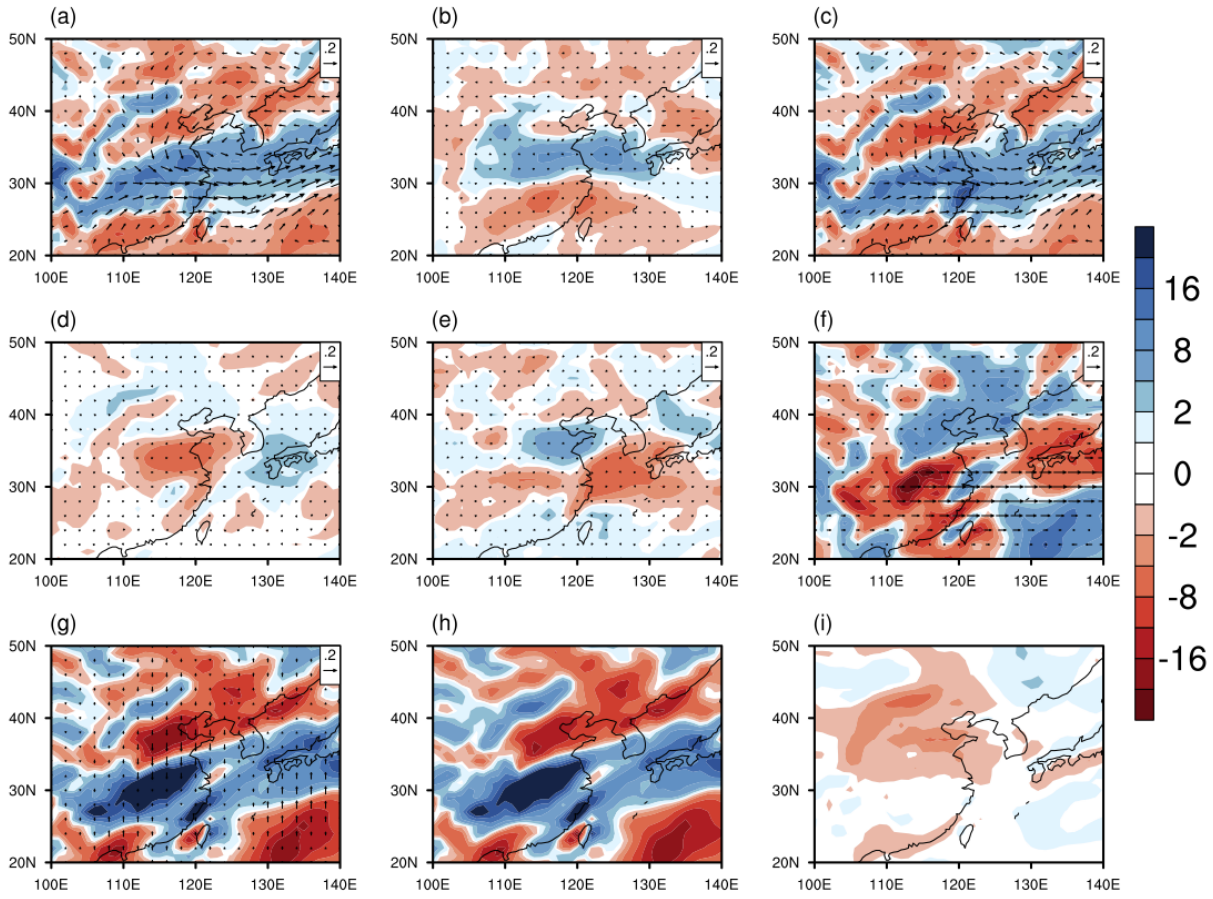

Figure 3.10: As in Fig. 3.9, but for comparison between high years and low years from 3 Jul (timing of mei-yu termination in high years) to 23 Jul (timing of mei-yu termination in low years). Here, changes denote low years minus high years.

3.6 Termination of the mei-yu with a northward extended Tibetan Plateau

Based on the various lines of evidence presented in sections 3.3–3.5, we propose this hypothesis on the mei-yu termination: *the weakening and eventual disappearance of the northerlies over northeastern China leads to the demise of the mei-yu, and this weakening is a direct consequence of the northward shift of westerlies beyond the northern edge of the plateau, around* 40° *N. We speculate that the reduced orographic forcing on the westerlies during the northward jet transition causes the weakening of the orographic downstream northerlies.*

To test this hypothesis, we artificially perturb the orographic forcing of the Tibetan

Plateau by changing the latitude of the northernmost edge of the plateau in the Community Atmosphere Model version 5 (CAM5). The expectation here is that with a more northward-extended plateau, mechanical forcing of the plateau on the westerlies should strengthen; by our hypothesis, northerlies downstream of the plateau should stay strong and mei-yu-like conditions persist as a result.

Figures 3.11a–d present the simulated seasonal evolution of 200-mb zonal wind over the plateau. With the presence of more northward-extended plateau, the westerlies impinging over the plateau are able to migrate to higher latitudes while the strength of the westerlies becomes weaker. In agreement with observations (Fig. 3.4f), tropospheric northerlies over northeastern China disappear from late June to late August in the Plateau_control run (Fig. 3.11e). Note that the simulated disappearance of northerlies occurs earlier (late June) than the observations (late July as suggested in Fig. 3.4f), indicating some model bias. Our hypothesis predicts stronger and more persistent northerlies downstream of the plateau as orographic forcing strengthens. When the plateau extends northward by 3° and 6°, downstream northerlies indeed persist longer, with the disappearance of northerlies occurring over a shorter time period (Figs. 3.11f-g). When the plateau extends northward by 10°, northerlies prevail over northeastern China throughout the summer season, though weakening of northerlies is still notable from late June to August (Fig. 3.11h).

Given the intensified northerlies (Figs. 3.11e–h) and meridional convergence (not shown), does the mei-yu front persist for longer duration in wider plateau scenarios? Note that due to the changed dimension of the plateau, the geographic location of the mei-yu in wider plateau cases may differ from the typical mei-yu in the present day. We thus identify the mei-yu front based on its expressed physical characteristics (i.e., sharp meridional gradients in θ_e). Compared with the control run, the meridional gradient of θ_e becomes stronger from April through June over central eastern China when the plateau extends northward by 6° and 10° (Figs. 3.11i–l). The relatively weak gradient of θ_e in the Plateau_3deg case is consistent with disappearance of northerlies in mid- to late June (Figs. 3.11f,j). In July, southerlies occupy central to northeastern China in the control run, while northerlies prevail over the region in the wider plateau scenarios. As a result, Figs. 3.11i–l show that the July meridional gradient of θ_e is more pronounced over northeastern China (40° to 45° N, 110° to 120° E) in the wider plateau scenarios than in the control run. This suggests that the wider plateau cases are able to maintain the mei-yu-like front over northeastern China in July.

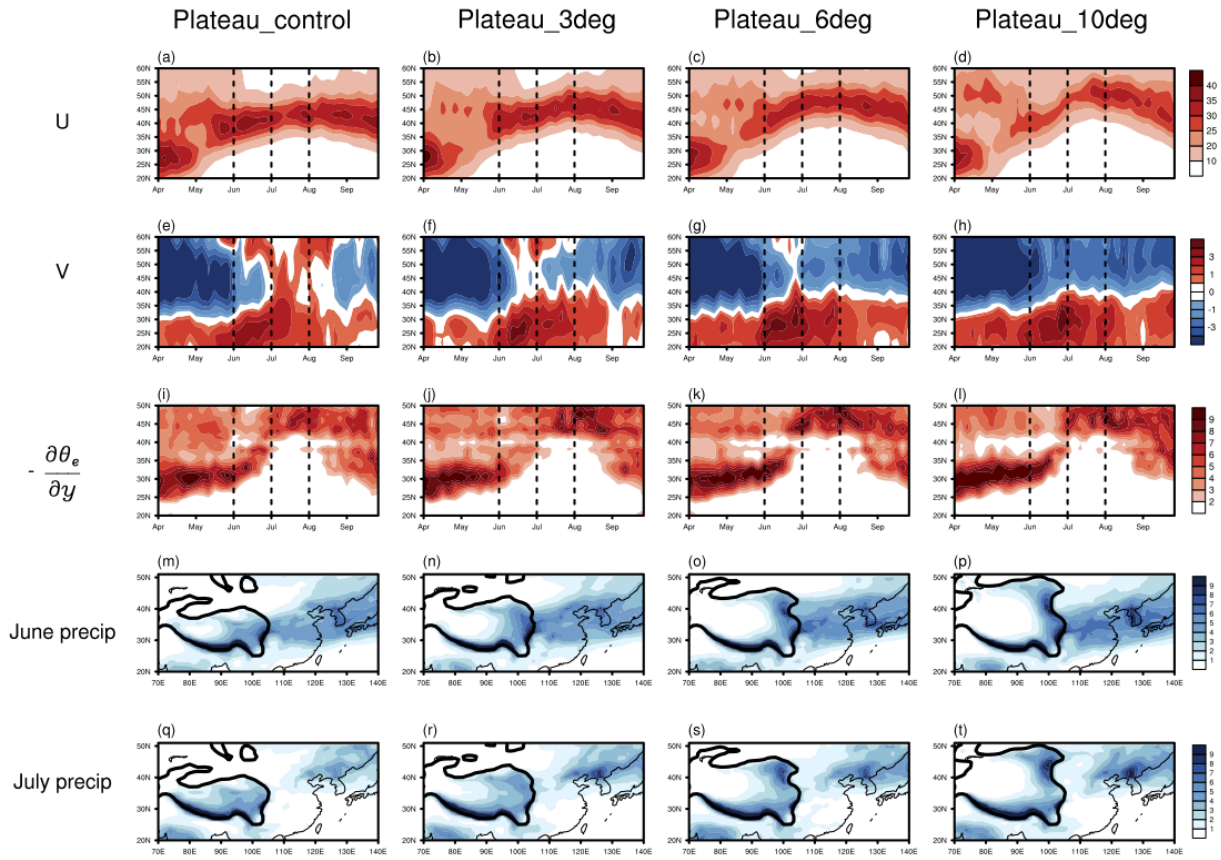

Figure 3.11: Results from (first column) the Plateau_control, (second column) Plateau_3deg, (third column) Plateau_6deg, and (fourth column) Plateau_10deg simulations. Hovmöller diagram of (a)–(d) zonal wind at 200 mb averaged over 80° to 100° E and (e)–(h) meridional wind at 500 mb averaged over 110° to 120° E ($\mathrm{m\,s^{-1}}$). (i)–(l) Hovmöller diagram of meridional gradient of θ_e at 850 mb and over 110° to 120° E ($3 \times 10^{-6}\,\mathrm{K\,m^{-1}}$). Large-scale precipitation averaged in (m)–(p) June and in (q)–(t) July ($\mathrm{mm\,d^{-1}}$). Black contours in (m)–(t) indicate an elevation of 2000 m.

Additionally, summer rainfall over East Asia could be partitioned into "banded" rainfall, which is associated with large-scale frontal convergence, and "local" rainfall, which is possibly driven by local buoyancy or topography (Day et al., 2018). Day et al. (2018) suggest that banded rainfall constitutes the majority of precipitation during pre-mei-yu and mei-yu, while midsummer is mainly characterized by sporadic local rainfall. We view the existence of banded large-scale rainfall as an indicator of mei-yu-like rainfall. Therefore, we expect more pronounced mei-yu-like rainbands over northeastern China in July in the wider plateau simulations. To estimate the amount of banded rainfall, we examine the large-scale rainfall

from the model output[2]. When northerlies over northeastern China are stronger and more persistent, large-scale rainfall over eastern China should be intensified as well. Figures 3.11m–p and 3.11q–t show the spatial distribution of large-scale rainfall in June and July, respectively. The leftmost panel suggests that the banded structure of rainfall in the control run is pronounced in June but disappears in July. In contrast, the rainbands remain in the wider plateau cases in July, though with weaker magnitude and more northward location.

One caveat to the "northward extended plateau" simulations is that it is difficult to exclude the potential role of diabatic heating over the plateau on the changes in the circulation and rainfall over East Asia (e.g., (Li & Yanai, 1996; Wu et al., 2012). Future studies are required to fully understand the relative contribution of the mechanical and thermal forcing of the Tibetan Plateau on the evolution of the EASM.

3.7 Response of downstream northerlies to the positioning of the jet in a dry dynamical core simulation

In this section, we use the dry dynamical core from CAM5 to further show that the downstream northerlies can originate from mechanical forcing on the westerlies by the Tibetan Plateau, and that the northerlies disappear when the westerlies impinging on the plateau shift sufficiently northward of it. The idealized physics of the dry dynamical core (see section 3.2.4) allows us to neglect possible effects of moisture feedbacks and diabatic heating on the westerlies. We relax the model to the same equilibrium radiative temperature profile in all cases, and perturb the relative positioning between westerlies and the plateau by shifting the plateau meridionally in order to mimic the northward seasonal migration of the westerlies.

3.7.1 Results

Figure 3.12 shows the zonal winds and meridional winds from the idealized simulations. When the plateau is shifted northward by 6° (PlateauN6; Figs. 3.12a,k), the configuration of westerlies around the plateau resembles spring in observations, with a much stronger southern branch of westerly wind to the south of the plateau compared with its counterpart to the north. In contrast to PlateauN6, the southern branch of westerlies in the PlateauN3 scenario is weaker, while the northern branch is stronger (Figs. 3.12b,l). The northern branch becomes further pronounced when the plateau is at the modern-day location (Figs. 3.12c,m). The westerlies are well north of the topography when the plateau is shifted to the south (Figs. 3.12d,e,n,o). In short, these scenarios mimic the northward seasonal migration of westerlies relative to the Tibetan Plateau from spring to summer. The responses of orographic downstream northerlies to perturbations of relative positioning between westerlies and the plateau are not clear-cut monotonic (Figs. 3.12f–j, p–t). However, the simulations

[2]Here, large-scale rainfall is rainfall from large-scale circulation that can be resolved by the model resolution, while convective rainfall is parameterized based on the Zhang-McFarlane scheme (Zhang & McFarlane, 1995)

demonstrate that the orographic downstream northerlies exhibit general weakening as location of westerlies changes from south of the plateau to north (Figs. 3.12f–j, p–t). It is also worth noting that the down- stream southerlies strengthen as the core of the westerlies shifts from being south of the plateau to north of it (Figs. 3.12f–j, p–t).

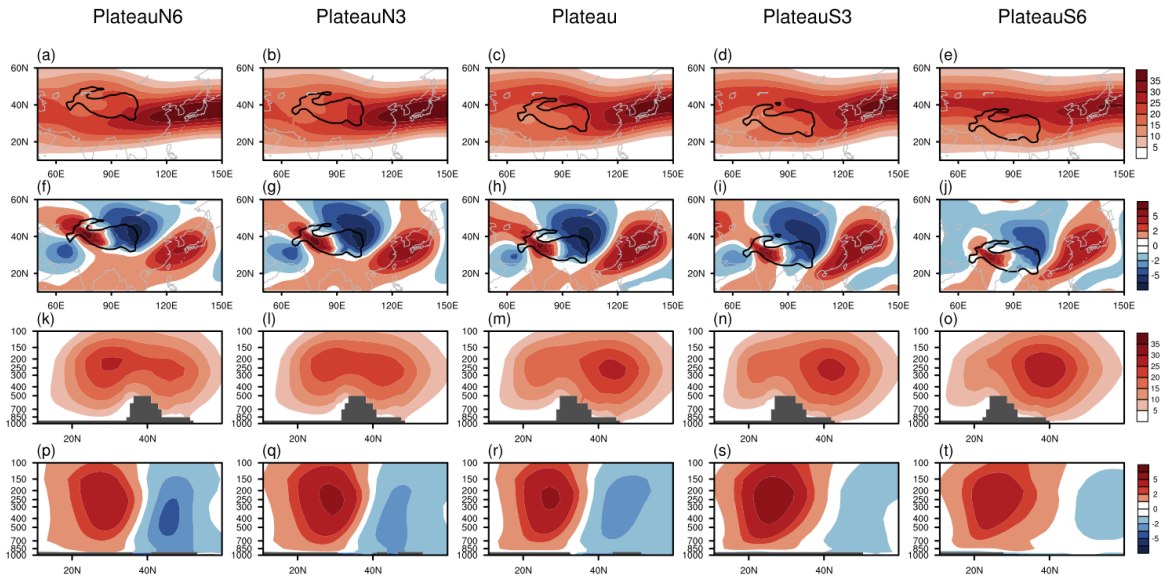

Figure 3.12: Results from the dry dynamical core simulations (from left to right) PlateauN6, PlateauN3, Plateau, PlateauS3, and PlateauS6. (a)–(e) Zonal wind at 200 mb. (f)–(j) Meridional wind at 500 mb. (k)–(o) Zonal wind averaged over 80° to 100° E; (p)–(t) Meridional wind averaged over 110° to 120° E. Black contours in (a)–(j) indicate an elevation of 2000 m.

3.7.2 Mechanism revealed in the dry dynamical core simulations

The low eddy geopotential height anomaly at 500 mb to the east of the orography appears to be a dynamical consequence of the orographic forcing on the atmosphere (Bolin, 1950; Charney & Eliassen, 1949; Held, 1983) (the eddy geopotential height is defined as

the geopotential height with the global zonal mean of geopotential height subtracted). We use the variation of eddy geopotential height at 500 mb downstream of the plateau as an indicator of changes in orographically forced stationary waves. In our idealized simulations, the simulations Plateau to PlateauS6 are the closest analogs to the seasonal shift of the jet to the north of 40° N in the real world, showing a weakening of orographic downstream northerlies from the former to the latter (Fig. 3.12). We show the eddy geopotential height at 500 mb from these simulations in Figs. 3.13a–c. Weakening of the orographic downstream cyclonic circulation from Plateau to PlateauS6 is evident, suggesting that the weakening of the mechanical forcing by the plateau as the jet shifts northward is the primary cause of the weakening of northerlies.

Lutsko & Held (2016) examined the transition from zonal to meridional propagation of orographically induced stationary waves by varying the height of the orography. They found that the stationary wave response is meridionally trapped, zonally propagating for weaker orographic forcing (i.e., lower orography altitude). When the forcing is increased, the wave propagates more meridionally and more into the tropics. We find similar behavior in our simulations. When the westerlies are impinging on the plateau, the orographic downstream stationary waves propagate equatorward. As the plateau is moved to the south, the orographic forcing weakens and the propagation of the stationary waves becomes more zonal. Figures 3.13d–f present the quasigeostrophic eddy streamfunction and the horizontal Eliassen–Palm (EP) flux [(Plumb, 1985), Eq. (5.7) therein] at 250mb. Following Lutsko & Held (2016), we show the ratio of the meridional component to the zonal component of the EP flux at 250mb averaged over 25° to 45° N, 100° to 150° E (highlighted with green dashed lines in Figs. 3.13d–f) in Fig. 3.13g. As positioning of the westerlies changes from south of the plateau to the north, the direction of the horizontal wave propagation downstream of the plateau becomes more zonal, and the eddy streamfunction weakens (Figs. 3.13d–f), further indicating reduced orographic forcing as the jet shifts to north of the plateau.

Taken together, when the westerlies shift to the north of the plateau, orographic forcing on the westerlies weakens, leading to reduced cyclonic circulation downstream of the plateau. Weakening of the cyclonic circulation in turn weakens the northerlies downstream of the topography.

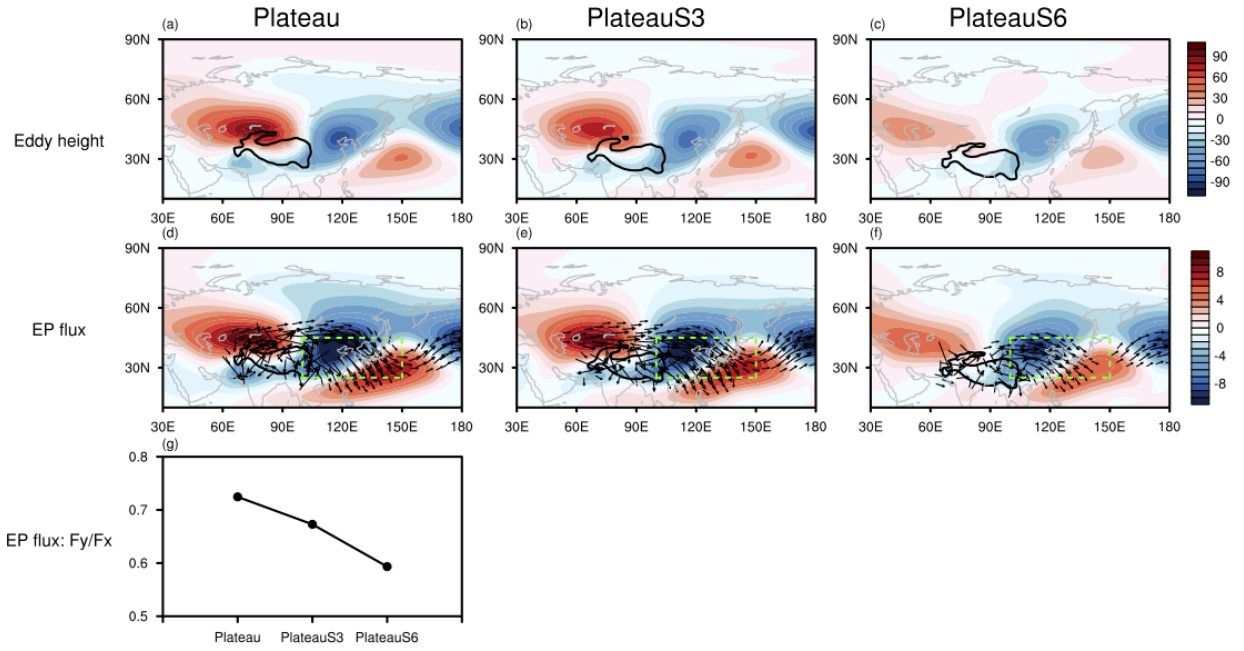

Figure 3.13: (top) Eddy geopotential height at 500 mb (m) and (bottom) horizontal EP flux (vectors; $m^2\,s^{-2}$) and quasigeostrophic eddy streamfunction (color shading; $10^6\,s^{-1}$) at 250 mb from the idealized simulations (a),(d) Plateau, (b),(e) PlateauS3, and (c),(f) PlateauS6. (g) The ratio of the meridional component of the EP flux to the zonal component of the EP flux at 250 mb averaged over 25° to 45° N, 100° to 150° E. Black solid lines in (a)–(f) denote imposed topography and indicate elevation of 2000 m. Green dashed lines in (d)–(f) denote the area used for the calculation of (g).

3.7.3 Weakening of the downstream cyclonic circulation in observations

Now we discuss to what extent the mechanism revealed in the dry dynamical core simulations is seen in the observed mei-yu termination. Resembling the dry dynamical core runs (Figs. 3.13a–c), Fig. 3.14 shows weakening of the cyclonic circulation over northeastern China from mei-yu to midsummer. Figure 3.15 shows Hovmöller diagrams of eddy geopo-

tential height z' at 200 and 500 mb averaged over 110° to 150° E (denoted by dashed lines in Fig. 3.14) for climatology of 1979–2007 (Figs. 3.15a,d), and for composites of high years (Figs. 3.15b,e) and low years (Figs. 3.15c,f) over 1979–2007. Here, the high and low years are selected based on the PC1 of July–August rainfall over East Asia (Chiang et al., 2017) (see section 3.4). The eddy geopotential height at 200 mb changes from negative values to positive values during mei-yu termination in all three cases, and indicates a transition from cyclonic to anticyclonic circulation in the upper troposphere (Figs. 3.15a–c). The anticyclonic circulation exists throughout the mid-summer stage, and reverts back to a cyclonic circulation when midsummer ends. In agreement with Fig. 3.14, the eddy geopotential height at 500mb also represents an abrupt weakening of the cyclonic circulation (Figs. 3.15d–f). These results support our interpretation that weakening of the tropospheric cyclonic circulation leads to disappearance of the northerlies.

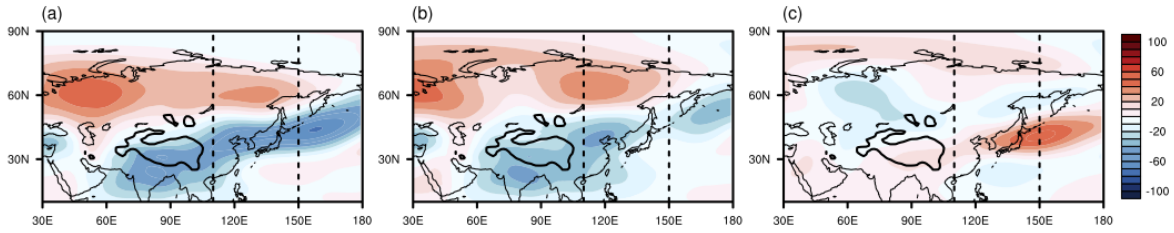

Figure 3.14: Eddy geopotential height at 500 mb (m) over 1979–2007 during (a) mei-yu, (b) midsummer, and (c) midsummer minus mei-yu. Timing of mei-yu and midsummer is determined by the SOM analysis. Dashed lines indicate the longitudinal range used for the zonal average shown in Fig. 3.15. Black contours indicate an elevation of 2000 m.

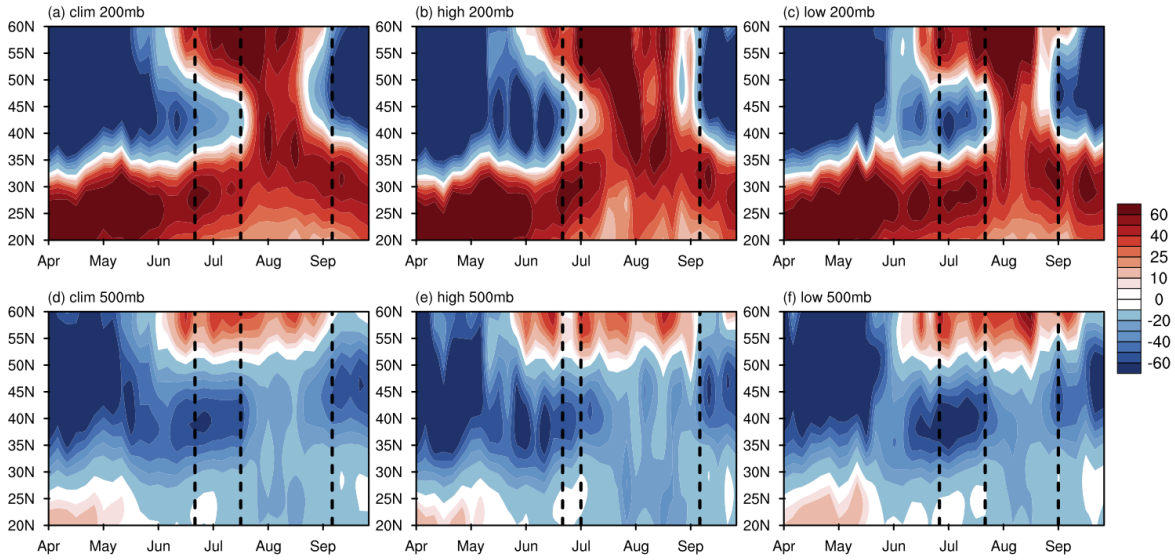

Figure 3.15: Hovmöller diagram of eddy geopotential height averaged over 110° to 150° E at (a)–(c) 200 mb and at (d)–(f) 500 mb for (left) 1979–2007 climatology, (center) high year climatology, and (right) low year climatology. Black dashed lines in (a)–(f) demarcate pre-mei-yu, mei-yu, midsummer, and end periods, respectively.

3.8 Summary

This study investigates how changes in the meridional position of the westerly jet impinging over the Tibetan Plateau affect termination of the mei-yu stage of the East Asian summer monsoon. Specifically, we ask whether there is a threshold in terms of the jet latitude over the Tibetan Plateau that controls the mei-yu termination.

In agreement with Kong et al. (2017) and Molnar et al. (2010), we show that the mei-yu termination in the climatology is accompanied by the northward migration of the jet axis away from the northern edge of the Tibetan Plateau at 40° N. Concurrently, tropospheric

northerlies over northeastern China weaken during the mei-yu and disappear when the mei-yu ends. Further examinations suggest that the close linkage between transit of jet axis beyond the northern edge of the plateau, weakening of downstream northerlies, and mei-yu termination also holds on interannual time scales. As westerlies exhibit large meridional excursions on synoptic time scales, we then examine whether the above connection holds on shorter (i.e., pentad) time scales. We found that the jet axis ranges between 38° to 41° N for mei-yu-like pentads, while midsummer-like pentads are associated with the jet axis between 40° to43° N. Furthermore, northeastern China (110° to 120° E, 35° to 40° N) exhibits strong northerly wind during mei-yu-like pentads, while the northerly wind almost disappears among midsummer-like pentads.

We argue that the reduction of the northerlies is causally linked to the demise of mei-yu through the following processes. First, reduction of the northerlies leads to weakening of the meridional contrast of equivalent potential temperature over central China, which is crucial for the maintenance of the mei-yu front (Li & Lu, 2017; Park et al., 2012). Furthermore, invoking the "ventilation effect" (Chou & Neelin, 2003), strong northerlies over northern China during the mei-yu limit the northward extension of the rainband by southward advection of low MSE air; when northerlies disappear, the ventilation effect is gone and rainfall extends to northeastern China in midsummer. Last, the disappearance of northerlies weakens the meridional wind convergence. Moisture budget analyses show that the significant reduction of total moisture flux convergence over central eastern China from mei-yu to midsummer is mainly due to weakening of meridional wind convergence.

We argue that weakening of orographic downstream northerlies is caused by reduced orographic forcing on the westerlies as the jet migrates beyond the plateau. To test this, we perform idealized simulations with CAM5 where the northern edge of the plateau is artificially extended northward, the idea being that orographic forcing should strengthen and thus the mei-yu should terminate later in such cases. The simulated results support our predictions. With the northern edge of the plateau extended north- ward, northerlies become more persistent, stronger, and the mei-yu-like (i.e., banded) rainfall regime becomes more pronounced over northeastern China. Several paleoclimate studies suggest that the uplift of the northern Tibetan Plateau intensifies the EASM (Baldwin & Vecchi, 2016; Tang et al., 2013; Zhang et al., 2012), which is qualitatively consistent with results from our wider plateau simulations. However, the mechanisms proposed by these studies are different from ours. Zhang et al. (2012) links the intensification of the EASM to westward extension of the western Pacific subtropical high with the uplift of the northern Tibetan Plateau, while Tang et al. (2013) and Baldwin & Vecchi (2016) invoke the thermal effect of the northern plateau on the EASM. Further studies are needed to elucidate how changes in the mechanical forcing of the plateau have contributed to the past evolution of the EASM.

To further explore the mechanical origins of the downstream circulation response to plateau topography, we employ a dry dynamical core with a plateau-like feature embedded in the core of the simulated westerlies. We artificially perturb the relative positioning between westerlies and the plateau by shifting the plateau meridionally. Similar to observations, we found that the orographic downstream northerlies weaken as positioning of the jet relative to

the plateau changes from south to north. These simulations highlight the importance of the mechanistic influence of the Tibetan Plateau on the downstream northerlies and hence on the termination of the mei-yu. This is in agreement with the results of Takahashi & Battisti (2007) (see Fig. 7 of Molnar et al. (2010)). They successfully simulated a mei-yu-like front in an aquaplanet configuration that excludes the land–ocean thermal contrast and retains the mechanical interplay between the westerly jet and the Tibetan Plateau. We interpret the weakening of the orographic downstream northerlies to reflect changes in the orographically forced stationary waves. As westerlies migrate beyond the plateau, the cyclonic circulation to the east of the plateau weakens. Additional diagnostics show that the quasigeostrophic eddy streamfunction is reduced and the propagation of the orographic downstream stationary waves becomes more zonal. These results suggest weakening of the orographic forcing on the westerlies when the westerlies are north of the plateau. Finally, we examine the observational data to see if the mechanisms inferred from the idealized simulations occur in the observed mei-yu termination. We find that mei-yu termination is indeed accompanied by a weakening of the cyclonic circulation at 500 mb downstream of the plateau, indicating weakening of the orographic forcing.

In short, the above findings suggest that the northern edge of the Tibetan Plateau at 40° N acts as a latitudinal threshold for jet position that triggers the termination of the mei-yu. The northerlies over northeastern China disappear as the jet axis over the plateau migrates north of 40° N, and which in turn shuts off the meridional circulation maintaining the mei-yu front and terminates the mei-yu. This view supports the speculation by Molnar et al. (2010), who argues for the crucial role of the mechanical effects of the Tibetan Plateau on the modulation of mei-yu.

Fundamental questions remain. Here we have only considered the role of the meridional position of the westerlies impinging over the plateau on the termination of the mei-yu. Although the results appear to support our speculation that 40° N is the threshold of jet latitude that terminates the mei-yu, other characteristics of the westerlies could play a role. Recent studies have proposed connections between rainfall over the Yangtze River basin with various characteristics of westerlies, such as the zonal variation of the jet center (Xie et al., 2015), the intensity of the jet (Wang & Zuo, 2016), and different configurations of the subtropical jet and polar front jet (Huang et al., 2014; Li & Zhang, 2014). Additionally, though this study focuses on the role of the mechanical interaction between the westerlies and the Tibetan Plateau on the termination of the mei-yu, we cannot yet exclude other interpretations such as the influence of midtropospheric warm advection (Kosaka et al., 2011; Kuwano-Yoshida et al., 2013; Sampe & Xie, 2010) and the role of surface heating over the Tibetan Plateau on East Asian summer rainfall (Wang et al., 2008a; Yanai & Wu, 2006). Finally, role of the adjacent ocean on the mei-yu merits further investigations. Recent studies suggest that variation of sea surface temperature over the East China Sea to the northwestern Pacific affect seasonal migration (Gan et al., 2019) and intensity (Kuwano-Yoshida et al., 2013) of the mei-yu–baiu rainband.

3.9 Acknowledgments

This work was supported by the National Science Foundation Grant AGS-1405479. The simulations in this study were conducted on the Yellowstone high-performance IBM cluster at NCAR. We thank Dr. Hisashi Nakamura and three anonymous reviewers for their careful reviews and insightful comments. We thank Leif M. Swenson for sharing codes of the SOMs, and Dr. Michael J. Herman for helpful discussions and for his constructive comments and edits on an earlier draft of this paper. WK thanks Dr. Peter H. Lauritzen for his help in the use of the NCAR Global Model Topography Generation Soft- ware. APHRODITE precipitation data were obtained from http://www.chikyu.ac.jp/precip/index.html, and we acknowledge the ECMWF for making the ERA- Interim data publicly available (http://apps.ecmwf.int/datasets/data/interim-full-moda/). Boundary topography and model output for the extended plateau simulations and the dry dynamical core simulations are archived and available at https://datadryad.org/stash/dataset/doi:10.6078/D1ZH51. Code for calculations of the three-dimensional Eliassen–Palm flux is obtained from http://www.atmos.rcast.u-tokyo.ac.jp/nishii/programs/index.html. Calculation and visualizations are based on the National Center for Atmospheric Research Command Language (NCL) (version 6.4.0), UCAR/NCAR/CISL/ TDD, http://dx.doi.org/10.5065/D6WD3XH5.

Chapter 4

Southward shift of westerlies intensifies the East Asian early summer rainband following an El Niño

4.1 Introduction

The mei-yu-baiu-changma rainband (mei-yu, hereafter) is the primary intraseasonal rainfall stage of the East Asian summer monsoon (EASM), and tends to intensify during the decaying phase of El Niño episodes (Chang et al., 2000; Huang & Wu, 1989; Shen & Lau, 1995; Wang et al., 2012). Previous work have focused on the intensification of the western Pacific subtropical anticyclone during that time, which enhances water vapor transport into East Asia and increases rainfall in the region. Several interpretations have been proposed to explain this enhancement. One view argues that the anomalous anticyclone over the western North Pacific occurs as a Rossby wave response (Gill, 1980) to the cold sea surface temperature (SST) anomalies over the western tropical Pacific during the El Niño developing phase. This anomalous anticyclone persists into the summer following El Niño due to positive feedback between surface wind, evaporation, and SST (wind-evaporation-SST feedback) (Wang & Zhang, 2002; Wang et al., 2000). An alternate view is the "Indian Ocean Capacitor" mechanism (Xie et al., 2009; Yang et al., 2007), which argues that the warming in the tropical Indian Ocean that peaks in the summer following an El Niño mediates the delayed effects of El Niño to East Asia summer climate. The Indian Ocean warming forces an equatorial Kelvin wave extending into the western Pacific, which then suppresses convection in the western North Pacific and establishes the anomalous anticyclone. Another school of thought challenges the "Indian Ocean Capacitor" mechanism and suggests the combination mode (C-mode) of the ENSO and annual cycle (Stuecker et al., 2013, 2014) is the primary driver for the development of the anomalous lower tropospheric anticyclone over the western North Pacific (Zhang et al., 2016, 2015). This view argues that the annual cycle plays an essential role in modulating East Asian climate via interactions with ENSO variability during the El Niño decaying phase.

We explore an alternative interpretation of the teleconnection between El Niño and the East Asian summer rainband by focusing on the role of the upper-tropospheric westerlies. Recent studies (Chen & Bordoni, 2014; Chiang et al., 2017; Kong & Chiang, 2019; Sampe & Xie, 2010) have shown that the westerlies impinging on the plateau plays a central role in the formation and maintenance of the East Asian rainband, from the spring rainfall over southeastern China (Park et al., 2012) to the pre-mei-yu and mei-yu stage during June and July (Chen & Bordoni, 2014; Chiang et al.; Kong & Chiang, 2019; Molnar et al., 2010; Sampe & Xie, 2010). Chiang et al. (2019) found that the East Asian rain band intensifies in June in the late 21st century under the RCP8.5 pathway emission scenario projections from the CESM large ensemble simulations (CESMLEN, hereafter) (Kay et al., 2014). They attribute this to tropical tropospheric warming, which sharpens the meridional temperature contrast over the subtropics and shifts the westerly jet southward. By separating the contributions of the SST warming and the direct effect of greenhouse gases (GHG), they found that the SST warming dominates the pronounced tropical upper tropospheric warming while the direct GHG forcing counters the influence of SST warming. In a similar vein, Zhou et al. (2019) suggest that the projected warming over eastern equatorial Pacific from the Climate Model Intercomparison Project Phase 5 (CMIP5) (Taylor et al., 2011) leads to southward displacement of westerlies and intensification of the early summer rainband. Both Zhou et al. (2019) and Chiang et al. (2019) point out a close connection between tropical oceanic warming, southward displacement of the jet, and intensification of East Asian summer rainband. However, both studies are based on model simulations of future projections, and the question remains whether the connection can be discerned in observations.

Here, El Niño provides a real-world test to the proposed linkage between tropical tropospheric temperature, westerlies, and the East Asian rainband. Warming in the eastern equatorial Pacific leads to uniform warming in the tropical troposphere (Chiang & Sobel, 2002; Chiang & Lintner, 2005), which sharpens the temperature gradient between the tropics and the subtropics and strengthens the westerlies impinging the Tibetan Plateau. This leads the westerlies to linger over the Plateau latitiudes for longer, inducing intense and persistent extratropical northerlies downstream of the plateau. The strengthening of the extratropical northerlies delays the seasonal transition of the East Asian summer rainfall, leading to an intensified rainband.

We will show that response of the atmospheric circulation and rainfall over East Asia to El Niño, from both observations and model simulations, support this hypothesis. We describe data and model simulations in section 4.2, and presents observational analysis in section 4.3. Section 4.4 shows results from a long-term pre-industrial control simulation. We summarize our main findings discuss remaining questions in section 4.5.

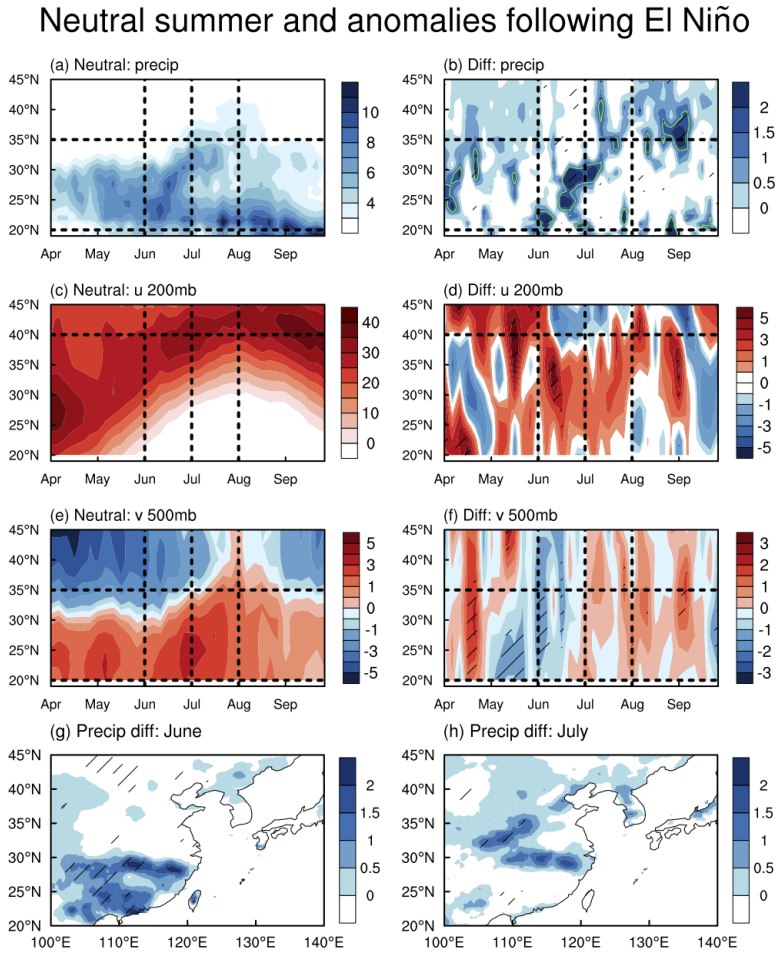

Figure 4.1: APHRODITE rain gauge data, NCEP1 200mb zonal wind, and 500mb meridional wind in decaying phase of El Niño events and the neutral summers. (a)-(b) Hovmöller diagram of rainfall over East China (105°E-120°E) for (a) neutral summers, and (b) the difference between the two categories (El Niño minus neutral), where the green solid contour highlights precipitation anomalies exceeding 1.5 mm d^{-1}. (c)-(d) Hovmöller diagram of 200mb zonal wind averaged in the Tibetan Plateau region (80°E-100°E) for (c) neutral summers, and (d) difference between the two categories. (e)-(f) Hovmöller diagram of 500mb meridional wind averaged in East China (105°E-120°E) for (e) neutral summers, and (f) difference between the two categories. (g)-(h) Precipitation of El Niño decaying phase minus neutral summers in (g) June and (h) July. Unit: mm d^{-1} for (a)-(b), (g)-(h); m s^{-1} for (c)-(f). The horizontal dashed lines in (a)-(b) and (e)-(f) denote south to central East China between 20°N and 35°N, and the horizontal dashed lines in (c)-(d) denote the approximate northern edge of the Tibetan Plateau. The vertical dashed lines in (a)-(f) highlight June and July. Hatched area in (b), (d), (f), and (h) indicates that the difference between the two categories exceeds statistical significance level at 90 %.

4.2 Data and methods

4.2.1 Rain Gauge and Reanalysis Data

Observed rain gauge data is from the APHRODITE daily product, APHRO_MA_025deg_V1101, at $0.25° \times 0.25°$ resolution (Yatagai et al., 2012). We also examined the precipitation rate from the NCEP/NCAR-1 reanalysis product and the CMAP (CPC Merged Analysis of Precipitation) precipitation dataset (Xie & Arkin, 1997). Historical SST is from the monthly 11adley Centre SST data set (HadISST1) (Rayner et al., 2003). We use daily and monthly zonal and meridional winds, geopotential height, air temperature, and specific humidity from the NCEP/NCAR Reanalysis-1 dataset (Kalnay et al., 1996). We identify the ENSO phase from the winter of 1950/51 to 2014/15 and focus on the behavior of the East Asian summer climate following El Niño peaks during 1951 to 2015.

4.2.2 Model Simulations

We examined 300-yr output from a fully-coupled pre-industrial control simulation with the Community Earth System Model version 1 (CESM1) (Hurrell et al., 2013), which has the same configuration with the CESM Large-Ensemble that is analyzed in Chiang et al. (2019). This allows us to directly compare the East Asian response to El Niño in this run with the East Asian response to RCP8.5 forcing in Chiang et al. (2019).

4.2.3 Definition of the ENSO phase

We define the ENSO phase based on the Oceanic Niño Index (referred to as ONI). The ONI is defined as the 3-month running means of SST anomalies in the Niño 3.4 region (5-5,120170). We first average the monthly SST anomalies over the Niño 3.4 region. We smooth the monthly Niño 3.4 SST index through a three-month running mean, and then average over December-February (DJF). We then identify the ENSO phase according to the value of the detrended and standardized DJF ONI. An El Niño event is defined when this value exceeds +0.75, and a La Niña event is defined when this value is less than -0.75; all other years are defined as neutral ENSO. We identified 13 El Niño events, 16 La Niña events, and 36 neutral ENSO events from 1950/51 to 2014/15 (Table C.1). We similarly identified 64 El Niño events, 73 La Niña events, and 163 neutral ENSO events from the CESM1 control simulation (not shown).

The conventional framework of examining the impacts of the ENSO usually compares responses to the warm and cold phase of the ENSO. However, previous work suggests the response of the East Asian summer climate to El Niño and La Niña is asymmetric (Hardiman et al., 2018). Thus, unlike the conventional framework, we compare the East Asian climate in the summer following an El Niño with that during neutral summer and use the former minus the latter to denote their differences. We use the two-tailed student's t-test to show the statistical significance of our results.

4.3 Observed responses during the summer following El Niño

The seasonal evolution of the East Asian summer monsoon rainfall in summers following an El Niño resembles those for neutral summers (Figure 4.1a), except for a pronounced rainfall intensification from June to mid-July over the south to central East China (Figures 4.1b, g, h). Relative to the amount received in neutral summer years, the intensification of June to July precipitation over south-central East China exceeds 1.5 mm/day (Figure 4.1b). The timing of the rainfall intensification co-incides with the pre-mei-yu and mei-yu stages in the climatology , and both rain stages are featured with banded precipitation (Chiang et al.; Day et al., 2018). Indeed, partitioning of the banded and local rainfall suggests that the rainfall intensification primarly arise from the banded precipitation, suggesting an enhancement in the large-scale convergence over the region during summers following El Niño (Day et al., 2018)(see Appendix C.1 and Figures C.1-C.2). We also examined the NCEP/NCAR-1 precipitation (Figure C.3); though NCEP/NCAR-1 does not assimilate observed precipitation (and is thus an entirely modeled quantity), it includes values over ocean and thus can show the rainfall intensification over a larger domain. It is also physically consistent with the NCEP/NCAR-1 circulation field and serves as a check of our interpretation. The response of the NCEP/NCAR-1 precipitation to El Niño is qualitatively similar to the APHRODITE rain gauge, with the rainfall intensification concentrating over south-central East China from June to July (Figure C.3). Similar analysis with the CMAP dataset further supports that the rainband intensification is a robust response during summers following El Niño, and that this intensification is strongest in June (Figure C.4).

In the following subsections, we will discuss the physical cause of the June and July intensification separately. In particular, we will show that the southward shift of westerlies is the reason for the June rainband intensification over East Asia.

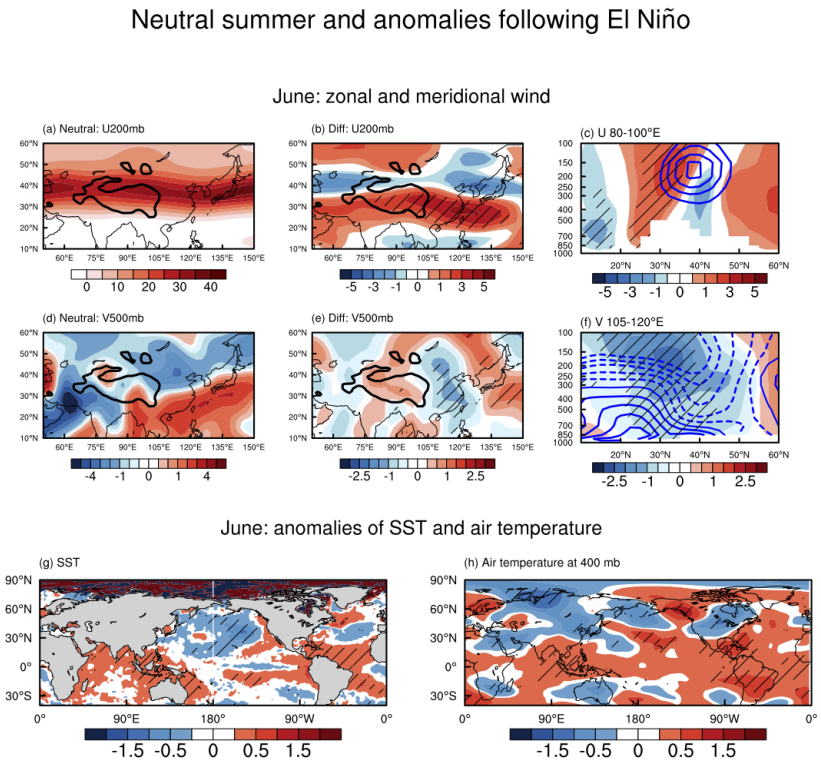

Figure 4.2: June zonal and meridional winds (unit: $\mathrm{m\,s^{-1}}$), sea surface temperature (SST) and air temperature (unit: °C). (a) 200 mb zonal winds in neutral summer, (b) anomalies of 200mb zonal wind during summers following El Niño (El Niño minus neutral summer), and (c) pressure-latitude cross section of zonal wind averaged in 80°E-100°E, where contours show values from neutral summer (contour interval $5\,\mathrm{m\,s^{-1}}$), and color shading show anomalies during summers following El Niño. (d) 500mb meridional winds in neutral summer, (e) anomalies of 500mb meridonal wind during summers following El Niño, and (f) pressure-latitude cross section of meridional wind averaged in 105°E-120°E, where contours show values from neutral summer (negative values are dashed, contour interval $1\ \mathrm{m\,s^{-1}}$), and color shading show anomalies during summers following El Niño. (g)-(h) Anomalies during El Niño decaying phase for (g) SST, and (h) air temperature at 400 mb. Hatched area indicates that the difference between the two categories exceeds statistical significance level at 90 %. The thick black contours in (a)-(b) and (d)-(e) indicate areas with elevation exceeding 2000 meters.

4.3.1 Southward shift of westerlies intensifies the rainband in June

There is a delayed northward migration of the westerlies across the Tibetan Plateau in June and July following an El Niño (Figures 4.1c-d). In particular for June, since the climatological westerlies reach the northern edge of the plateau (40° N), this delayed mi-

gration implies that the westerlies linger longer over the Plateau latitudes (Figures 4.2a-c). As suggested by Kong & Chiang (2019) and Chiang et al., this will lead to enhanced flow-orography interaction between the westerlies and the plateau, resulting in stronger extratropical northerlies downstream of the plateau; this is indeed observed in the 500 mb meridional wind response following an El Niño (Figures 4.1e-f and Figures 4.2d-f).

The synchronous changes in the June rainfall, westerlies, and northerlies of East Asia resemble the results of Chiang et al. (2019), who found similar responses of East Asian summer climate at the end of the 21st century in the RCP8.5 as simulated by the CESMLEN. They show that the root cause of the projected intensification of East Asian early summer rainband is the warmer tropical tropospheric temperatures resulting from tropical oceanic warming, that in turn strengthens the subtropical jet impinging on the Tibetan Plateau. A similar response occurs here, except that in our case the tropical tropospheric warming is driven by El Niño. In agreement with previous findings (Seager et al., 2003), there is a tropics-wide warming of the tropical troposphere and cooling in the mid-high latitudes over Eurasian continent. The atmospheric temperature gradient between the tropics and the extratropics thus sharpens over Eurasia (Figure 4.2h and Figure C.5a), and the westerly jet shifts to the south of its climatological position (Figures 4.2b-c). Consistent with the tropics-wide tropospheric warming, there is basinwide warming of the tropical SST in both the tropical Indian and Atlantic Oceans (Figure 4.2g).

Following Chiang et al. (2019), we employ a vertically integrated moisture budget analysis to diagnose the causes of the rainfall intensification in June (Appendix C.2 and Figure C.6). In agreement with changes of rainfall, there is enhanced moisture flux convergence over southeastern China (Figure C.6a), which is primarily contributed by changes of horizontal winds (Figure C.6c). Further decomposition suggest that changes in the convergence of meridional moisture flux (Figure C.6g) dominate the increases in the moisture flux convergence over southeastern China. In particular, changes in the meridional wind convergence appear to be the root cause (Figure C.6h). This is in agreement with the cause of the late 21st century rainband intensification as diagnosed in Chiang et al. (2019) in the CESMLEN RCP 8.5 simulation. Finally, the June rainfall intensification over western North Pacific (see Figure C.3 for the NCEP/NCAR-1 precipitation) also results from enhanced meridional moisture flux convergence (Figure C.6g), implying that the rainfall intensification over the ocean is part of a large-scale rainband intensification.

4.3.2 Rainband intensification in July

The proposed bridging effect by the westerlies between El Niño and East Asian rainband does not appear to operate for July. It is because that the tropospheric temperature response to El Niño gradually damps following an El Niño. Compared to June, the temperature contrast between the tropics and the subtropics is considerably reduced in July (Figure C.5b). Thus, though the westerlies over the Plateau latitudes also show southward shift during July following El Niño (Figure 4.1d), this perturbation is not strong enough to strengthen the orographic downstream northerlies as seen in June (cf. Figures C.7e-f and Figures 4.2e-f).

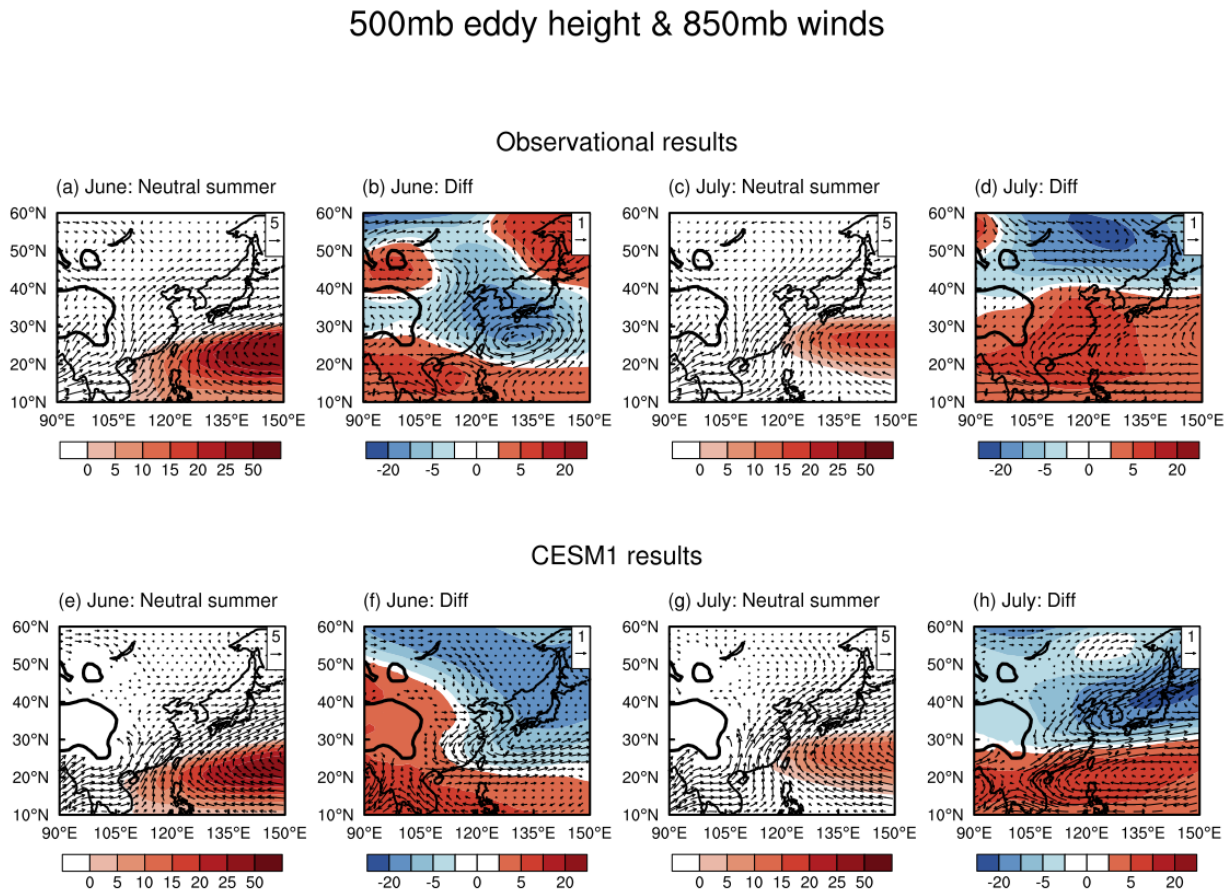

Figure 4.3: Eddy geopotential height at 500 mb (colors shading, unit: meters) and horizontal winds at 850 mb (vectors, unit: m/s) from (top) observational analysis and (bottom) CESM1 control run. (a)-(b) and (e)-(f) show results in June, and (c)-(d) and (g)-(h) show results in July. Results from neutral summers are shown in (a), (c), (e), and (g). Results from anomalies during summers following El Niño are shown in (b), (d), (f), and (h).

We attribute the rainfall intensification in July to an enhancement of the western Pacific subtropical high, which intensifies the monsoonal southwesterlies. Indeed, the moisture

budget analysis in July suggests that the zonal wind convergence from anomalous westerlies (not shown) and the meridional wind convergence from anomalous southerlies (Figures C.7f-g) dominate the moisture flux convergence in central East China. To further show this, we present the lower tropospheric winds (vectors) and the mid-tropospheric eddy geopotential height (shading) in Figures 4.3a-d. The eddy geopotential height, defined as the deviation of geopotential height from the regional averaged in 040,180-180, is a measure of the western Pacific subtropical high (He et al., 2015). In June, cyclonic circulation and northerlies anomalies dominate central-northern East China, while the intensification of the subtropical high is confined over the South China sea. In July, however, the enhancement of extratropical northerlies disappear and the anticyclonic anomalies dominate south to central China.

Taken together, the above observational analysis suggests that following El Niño, the East Asian summer rainband intensifies from June to July, with the most of the intensification occuring in June. The June rainband intensification results from enhanced extratropical northerlies, which is induced by the flow-orography interaction due to southward shift of westerlies. The effects of perturbation in westerlies on the rainband disappear in July, and during this time the enhancement of the western Pacific subtropical high presumably comes to play. However, it is worth noting that enhanced interaction between westerlies and the Tibetan Plateau appear to be a crucial factor for July rainband intensification during summers following extreme El Niño events (see discussions in section 4.5).

4.4 Results from CESM1 pre-industrial control simulation

We further examine the El Niño teleconnection to East Asia in a CESM1 pre-industrial control simulation that uses the same model configuration as analyzed in Chiang et al. (2019). The advantage of using this simulation is that there is a considerably larger sample of El Niño events to assess statistical significance, and furthermore the changes inferred here can be directly compared to the CESMLEN results in Chiang et al. (2019) given that the same model is used.

Similar to the observations, the East Asian rainband in the summer following El Niño in the CESM1 control run undergoes intensification in June and July (Figures 4.4a-b, g-h). This intensification is accompanied by the southward shift of westerlies over the Plateau, and enhanced extratropical northerlies downstream of it (Figures 4.4c-f and Figures C.9-C.10). The strong southward displacement in the westerlies following El Niño episodes persists into July in the model simulations, which differs from results in section 4.3 but resembles observed response to extreme El Niño (Appendix C.3 and Figures C.13-C.17). As a result, the extratropical northerly anomalies are strong in both months, and leads to intensified rainband in both June and July. We think that the persistence of the signal into July arises from the simulated El Niño magnitude being stronger and the decay from peak El Niño being more gradual than the observations (Figure C.11), resulting in a more persistent tropical SST and tropospheric warming in the summer following El Niño (Figure C.12).

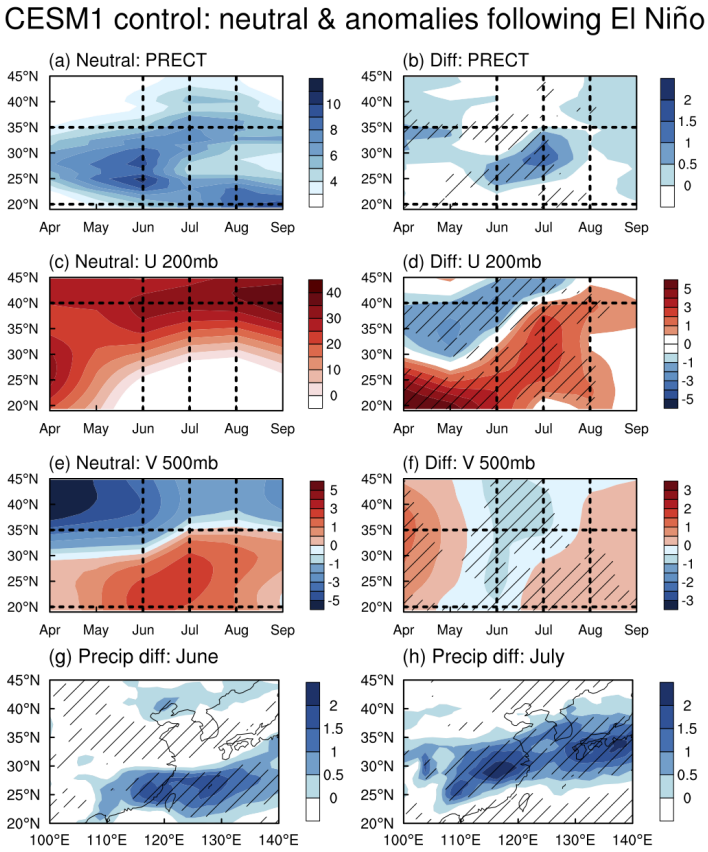

Figure 4.4: Total precipitation, 200 mb zonal wind, and 500 mb meridional wind from the CESM1 control run. (a)-(f) Hovmöller diagram of (a)-(b) total precipitation over East China (105°E-120°E), (c)-(d) 200 mb zonal wind over the plateau region (80°E-100°E), and (e)-(f) 500 mb meridional wind over East China (105°E-120°E). (a), (c), (e) show results from neutral summers, and (b), (d), (f) show anomalies during summers following El Niño. (g)-(h) show precipitation anomalies during summers following El Niño for (g) June and (h) July. Unit: $\mathrm{mm\,d^{-1}}$ for (a)-(b), (g)-(h); $\mathrm{m\,s^{-1}}$ for (c)-(f). The horizontal dashed lines in (a)-(b) and (e)-(f) denote south to central East China between 20°N and 35°N, and the horizontal dashed lines in (c)-(d) denote the approximate northern edge of the Tibetan Plateau. The vertical dashed lines in (a)-(f) highlight June and July. Hatched area indicates that the difference between the two categories exceeds statistical significance level at 90°.

The enhancement of both northerlies and southerlies results in enhancement of large-scale frontal convergence and explains why the July rainband intensification is so pronounced in the CESM1 simulation.

4.5 Summary and Discussion

We reveal a teleconnection mechanism between El Niño and the East Asian early summer rainband through the former's control on the westerlies impinging on the Tibetan Plateau. Both observational analysis and model simulations show that westerlies during the summer following El Niño are shifted southward, prolonging the westerlies' impinging on the Plateau. The resulting ororgraphic forcing leads to a strengthening of northerlies downstream of the Tibetan Plateau, and intensification of rainfall over the south to central East China. This mechanism is similar to ones proposed in recent studies that show a dynamical linkage between the latitude of westerlies impinging on the plateau and the timing and duration of East Asian summer rainfall (Chiang et al.; Kong & Chiang, 2019). In this instance, the southward shift of westerlies results from a sharpening of meridional temperature contrast at the subtropics, which is ultimately due to the warming response of the tropical troposphere to the warming in the eastern equatorial Pacific.

The similarity in the mechanism of rainband intensification found here, with that found in Chiang et al. (2019) for the intensification in the late 21st century from RCP 8.5 simulations, suggests that observed East Asian early summer rainband response to El Niño can be viewed as a modern-day analog to projected rainband changes under global warming. If this is indeed the case, then these observed instances can potentially be used to provide guidance on the nature of the future East Asian rainfall changes, in particular with changes to rainfall extremes. Notably, the CESMLEN projections suggest that East Asian summer rainfall extremes will double in the late 21st century (Chiang et al., 2019).

Recent studies suggest that ENSO possess rich diversity in the structure and warming magnitude of SST and remote impacts (Capotondi et al., 2014; Johnson, 2013; Takahashi et al., 2011). It thus merits future work to examine to what extent the proposed teleconnection would be enhanced or damped for different ENSO flavors. For instance, the East Asian summer rainband following three extreme El Niño (1982/83, 1986/87, and 1997/98) is significantly enhanced in both June and July (Appendix C.3 and Figures C.13-C.17); this differs from section 4.3 that suggest the rainband intensification occur mainly in June. Similar to the CESM1 results, tropical tropospheric warming following the three extreme El Niño is strong. The warming persists to July, resulting in intensified westerlies over the Tibetan Plateau latitude and enhanced orographic northerlies and frontal convergence. Further, given the asymmetric response of East Asian summer rainfall to El Niño and La Niña (Hardiman et al., 2018), it raises the question of whether the asymmetric response of East Asian summer rainfall arises from different responses in the westerlies to SST anomalies in the eastern equatorial Pacific. Another problem that we leave for future study is how our mechanism relates to previous studies that tie the teleconnection to the role of the western

Pacific subtropical high. One intriguing question in particular is how the enhancement of the western Pacific subtropical high and the northward shift of westerly jet are dynamically linked.

4.6 Acknowledgments

This work was supported by the National Science Foundation Grant AGS-1405479. We thank Jesse Day for sharing the banded and non-banded rainfall in APHRODITE: https://figshare.com/projects/Data_and_code_for_Changing_character_of_rainfall_in_eastern_China_1951-2007_/28563. We obtained the NCEP-NCAR1 dataset from https://www.esrl.noaa.gov/psd/data/gridded/data.ncep.reanalysis.htm. The NCEP-NCAR 1 precipitation rate is downloaded from the IRI/LDEO Climate Data Library. The CMAP Precipitation data is provided by the NOAA/OAR/ESRL PSL, Boulder, Colorado, USA, from their website at https://psl.noaa.gov/data/gridded/data.cmap.html. We thank the APHRODITE's Water Resources (https://www.chikyu.ac.jp/precip/english/) for providing the APHRODITE dataset. The HadISST dataset is obtained from https://www.metoffice.gov.uk/hadobs/hadisst/data/download.html. We thank the CESM Large Ensemble Community Project for making their model simulations publicly available at http://www.cesm.ucar.edu/projects/community-projects/LENS/data-sets.html. We would like to acknowledge high-performance computing support from Cheyenne (doi:10.5065/D6RX99HX) provided by NCAR's Computational and Information Systems Laboratory, sponsored by the National Science Foundation.

Chapter 5

Conclusion

5.1 Summary

The westerlies above the Asian continent experiences a northward migration from the south of the Tibetan Plateau to the north during the spring to summer seasonal transition. Meanwhile, to the east of the plateau, East Asian summer monsoonal rainfall exhibits a unique seasonality, featuring two abrupt jumps of the associated precipitation with three stationary periods in between. Though the synchronous relationship between the jet and the EASM precipitation has long been observed, whether and how they are dynamically linked remains poorly understood. This dissertation explored the role of westerlies impinging on the Tibetan Plateau in determining the seasonal transition of the EASM. Our findings during this adventure have been reported in Chapters 2 to 4 (Kong & Chiang, 2019; Kong et al., 2017; Kong & Chiang, 2020), each offering a new angle understanding the EASM under a specific scenario.

Chapter 2 explored changes of the EASM from the early to the late Holocene. Previous studies suggest that the lighter oxygen isotopic composition from speleothem records in East Asia indicates that the EASM was more intense during the early to mid-Holocene than today. We argue that viewing changes of the EASM across the Holocene only through its rainfall intensity is incomplete. And we tie the previously argued changes in the rainfall intensity to altered seasonality of the EASM during the Holocene. Our simulations suggest that the early to mid-Holocene featured a more rapid mei-yu onset and an advanced mei-yu termination, leading to a shorter mei-yu and prolonged midsummer stage. We find that the enhanced seasonality of the EASM during the early to mid-Holocene is accompanied by a northward displacement of the westerlies, suggesting that the latter might determined the former.

Chapter 3 examines the dynamical process causing the mei-yu termination. We invoked a linkage between the mei-yu termination and the weakening of the extratropical northerlies. The weakening of the northerlies reduces the large-scale meridional convergence, thus weakening the synoptic condition favorable for the mei-yu front formation. We tied the strength of the northerlies in northeastern China to the mechanical interaction between the westerly jet and the Tibetan Plateau. When the jet is impinging on the plateau, orographic

forced stationary waves present a cyclonic circulation downstream. The associated strong northerlies converge with monsoonal southerlies and maintain the mei-yu rainband. When the jet migrates to the north of the plateau, the orographic forcing is gone, and the downstream northerlies disappear. Thus mei-yu terminates. Therefore, we conclude that 40N is a latitudinal threshold for the jet transition, which marks the transition from mei-yu to midsummer.

Chapter 4 addresses why East Asian summer rainfall is usually more intense following El Niño. Unlike previous work arguing the role of an intensification of the western Pacific subtropical high, we focus on the role of the southward displacement of westerlies impinging on the Tibetan Plateau. The tropical tropospheric warming following El Niño sharpens the meridional temperature gradient between the tropics and the subtropics, causing a southward displacement and strengthening of the westerlies. The westerlies impinge over the plateau for longer, resulting in stronger northerlies in northeastern China and enhancement of the large-scale meridional convergence. Notably, this mechanism resembles the intensification of East Asian early summer rainband in future projections, suggesting that El Niño's impacts on the EASM are a present-day analog to future warming.

In sum, we presented various evidence supporting a dynamic linkage between the positioning of the westerlies relative to the Tibetan Plateau and the seasonal transition of the EASM. These findings suggest that understanding the behavior of the Asian westerlies is critical to interpret past variations of the EASM and to predict its future changes.

5.2 Future work

5.2.1 Westerly jet and the western Pacific subtropical high

The dissertation focuses on the role of orographic forcing on the westerly jet and resulting downstream northerly flow on the formation and maintenance of mei-yu. On the other hand, the western Pacific subtropical high has long been thought of as a primary driver of the mei-yu. Further, the subtropical high also experience a northward migration during the spring to summer seasonal transition (Figure 5.1). Is there a causal relationship between the northward jet shift across the plateau and the northward extension of the subtropical high? It is plausible as the subtropical high is a stationary wave (Miyasaka & Nakamura, 2005; Rodwell & Hoskins, 2001; Ting, 1994), and the main product of the jet-plateau interaction is orographic forced stationary waves. I hypothesize that the jet modulates the subtropical high's position through changes in the propagation of orographic forced stationary waves during the northward jet transition. Some preliminary exploration (not shown) suggests that the plateau's presence is crucial for the formation of subtropical high, indicating the interaction between the jet and the plateau may play a fundamental role in determining the subtropical high. More investigation is needed before we reach any affirmative conclusions.

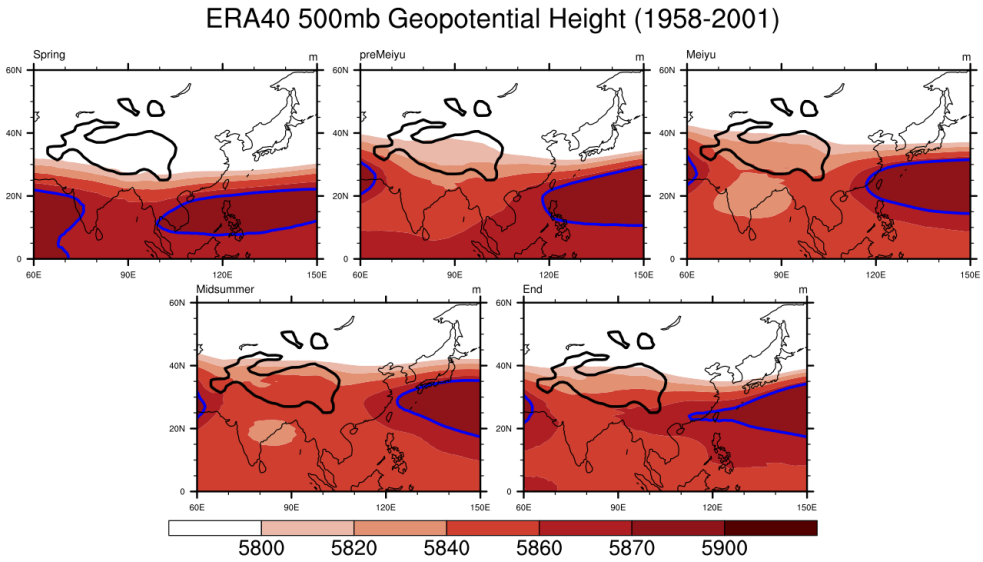

Figure 5.1: Climatology of 500 mb geopotential height averaged in each intraseasonal rain stage of the EASM. The timing of the rain stages were identified from the self-organizing map analysis of the APHRODITE from 1958 to 2001. The thick blue contours highlight the value of 5870 m, an approximation of the edge of the western Pacific subtropical high.

5.2.2 On the East Asian rainband

Role of northerlies versus quasi-geostrophic ascent

Chapter 3 suggests that the weakening of extratropical northerlies in northeastern China causes the mei-yu termination. And we tied the strength of the northerlies to orographic forced cyclonic circulation downstream of the plateau. We invoked the link between the northerlies and the mei-yu based on the reasoning that convergence between the cold, dry northerlies and the warm, moist monsoonal southerlies creates a favorable environment for the formation of the front. Recent studies suggest a close linkage between the quasi-geostrophic (QG) ascent embedded in atmospheric waves and East Asian precipitation, suggesting an alternative interpretation of linking the mei-yu to the westerlies (Cohen & Boos, 2017; Nie & Fan, 2019; Park et al., 2015). For example, Cohen & Boos (2017) suggest that enhancement of East Asian winter precipitation follows the ascent motion downstream of the cyclonic trough in orographically induced stationary waves. Focusing on synoptic scales, both Park et al. (2015) and Nie & Fan (2019) find an eastward propagation of transient eddies accompanied by QG ascent developing to the east of cyclonic circulations before the occurrence of peak rainfall in East China. On a side note, there are two precipitation zones in the summer Southern Hemisphere, the South Pacific convergence zone (SPCZ) and the South Atlantic convergence zone (SACZ), share similar features with the mei-yu (Kodama, 1992). And Wiel et al. (2015) suggests the QG ascent associated with atmospheric Rossby waves propagated to these regions is fundamental to the origin of the SPCZ and the SACZ. Thus, it merits future work to quantify the relation between the extratropical northerlies, the QG ascent ahead of the cyclonic circulation, and the mei-yu rainband.

More on the mei-yu rainband

More intriguing questions regarding the behavior of the mei-yu rainband remain. First, summer floods and droughts in central East China are closely tied to the length of the mei-yu season, which is collectively determined by the timing of its onset and termination. Take summer 2020 for example. Based on the report from Chinese meteorological service, this summer features an early mei-yu onset and a delayed mei-yu termination, bringing record-breaking catastrophic rainfall in central East China. Thus, insights on the prediction of these timings are crucial for the local summer rainfall forecast. We've shown that the mei-yu terminates when the westerly jet migrates off the northern edge of the plateau (chapter 3). However, it is unclear whether a quantitative relation between the positioning of jet and the mei-yu onset exists. In climatology, the mei-yu onset is accompanied by the westerly jet reaching the northern edge of the plateau, and the mei-yu termination occurs when the jet migrates away the plateau's northern edge (Chiang et al.; Kong & Chiang, 2019). It suggests the climatological mei-yu coincides with the westerly jet stays around the northern edge of the plateau. On synoptic timescale, however, the occurrence of the mei-yu rainband events is noisy; and the length of the mei-yu during each summer is determined by the number of days when the mei-yu rainband appear in central East China. It brings us to another question:

is the occurrence of the mei-yu rainband events on the year-to-year timescale determined by the frequency of jet lingering around the plateau's northern edge? If it is the case, what controls the frequency of the jet stay around that latitude?

Second, this dissertation explicitly focused on the East China sector of the EASM, with no discussions of the changma in Korea and baiu in Japan. Future work is required to examine the regional difference of the East Asian rainband and test whether the proposed relation between jet, northerlies, and the mei-yu over East China can be applied to understand changma and baiu. Further, resembling the SPCZ and the SACZ, the mei-yu-changma-baiu rainband as a whole feature a southwest to northeast diagonal tilt, and its length scale can span over 4000 km. How do the rainband's tilt and length scale vary, and what are the underlying mechanisms? These questions are particularly relevant to summer precipitation in the Korean Peninsula and Japan, as they locate at the tail of the rainband.

5.2.3 On the linear versus nonlinear orographic forcing and the jet

There are two possible routes when the atmospheric zonal flow encounters orography. The linear orographic forcing refers to a vertical deflection in which the flow climbs up and over the orography. In contrast, the nonlinear forcing indicates a horizontal deflection with the flow splits around the orography. Figure 5.2-5.3, adapted from Ringler & Cook (1997), illustrate the two responses. Both regimes lead to a cyclonic circulation to the east of the orography. However, the forced downstream stationary wave is more meridionally trapped in the linear regime while showing a preferentially equatorward propagation in the nonlinear regime. Chapter 3 tied the extratropical northerlies and to the orographically forced cyclonic circulation in northeastern China. However, we did not separate the effects of the linear versus nonlinear forcing on the northerlies. Related, it is unclear how these two regimes evolve during the northward jet transition across the plateau. Since the linearity of the orographic forced stationary waves tends to break down as the mountain height increases, I speculate that there is a transition from the nonlinear regime to the linear regime as the jet migrates from the plateau's peak to the plateau's northern edge. Our idealized simulations with the dry dynamical core support this speculation. As shown in Figure 3.12-3.13, the propagation of the gaussian mountain forced stationary waves become more zonal as the positioning of the jet shifts from the south of the mountain to the north. Further, the ambient atmospheric conditions (such as low level wind speed, meridional temperature gradient, and vertical wind shear) also affect the degree of linearity of the orographic forcing (Ringler & Cook, 1997). For example, Cook & Held (1988) found that the linearity increases with increasing the background meridional temperature gradient. Clarifications on these processes may help us gain a better understanding of the controlling factors of the latitude and the spatial length scale of the mei-yu rainband.

Another remaining problem, also related to the above discussion, is to explore how changes in the characteristics of the atmospheric westerlies affect its interaction with the plateau. We've been using the latitudes of the maximum upper tropospheric zonal wind at the plateau longitude to quantify the jet transition. However, the latitude of the upper tropo-

spheric jet core is an oversimplified metric, given that the westerly jet is a three-dimensional flow. Future investigations should consider these possible effects: the wind speed, the width, the structure (single versus double jet as discussed in Son et al. (2008)), and the nature of the jet (baroclinic subtropical jet versus barotropic eddy driven jet).

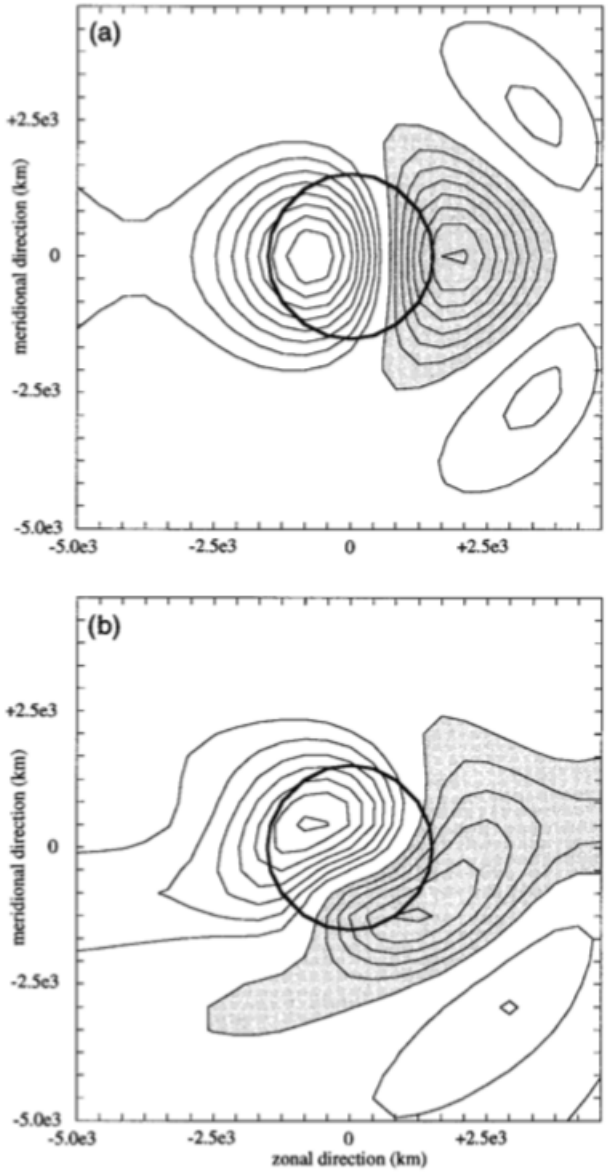

Figure 5.2: The (a) linear and (b) nonlinear respones to mechanical forcing at the surface in terms of eddy streamfunction. Half-width of the orography shown by dark circle. Negative values are shaded. Figure adapted from (Ringler & Cook, 1997).

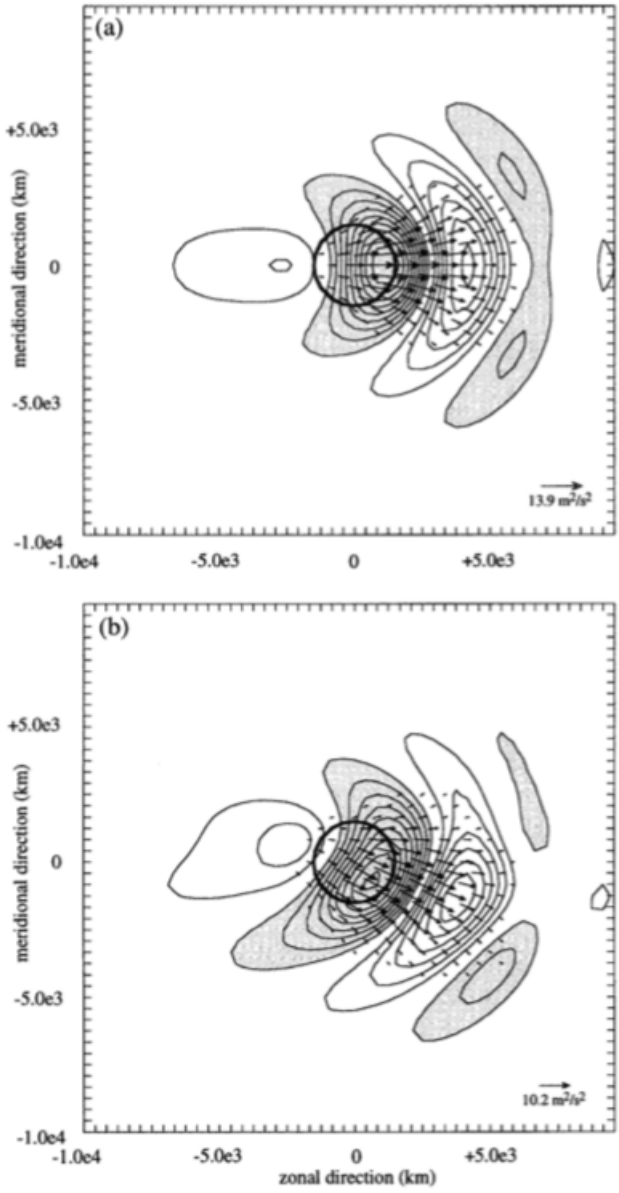

Figure 5.3: The (a) linear upper-level response and (b) the nonlinear upper-level response shown in terms of eddy streamfunction (contours) and horizontal wave fluxes (vectors). Negative values are shaded. respones to mechanical forcing at the surface in terms of eddy streamfunction. Half-width of the orography shown by dark circle. Negative values are dashed. Figure adapted from (Ringler & Cook, 1997).

5.2.4 Past climate change in East Asia

More lessons on how the East Asian climate works can be learned from past climates. Three particularly intriguing directions are suggested below.

Precipitation and $\delta^{18}O_c$ in the early to mid-Holocene

In chapter 2, we only incorporated the effects of orbital forcing to understand the evolution of the EASM across the Holocene. However, there was an extensive remnant of the Laurentide Ice Sheet (Peltier, 2004) and the Fennoscandian Ice Sheet (Stroeven et al., 2016) during the early Holocene. Contrary to the insolation forcing, the presence of the ice sheets could reduce atmospheric moisture content and strengthen the meridional temperature gradient and shift westerlies southward. Though the enhanced boreal summer insolation during the early Holocene may override the effects of the Laurentide and Fennoscandian Ice Sheets in East Asia (Zhang et al., 2020), a more rigorous investigation of their competing effects is needed.

For the interpretation of $\delta^{18}O_c$ in East Asia, increasing evidence (Battisti et al., 2014; Pausata et al., 2011) rejects the hypothesis that fluctuations of the $\delta^{18}O_c$ on geological scales reflect the local rainfall intensity. Further, Chiang et al. (2020) suggest a close association between the depletion (enrichment) of $\delta^{18}O_c$ in East Asia and enhanced (reduced) seasonality as well as a northward (southward) displacement of westerlies on the year-to-year timescale. Whether and how a northward shift in the Asian westerlies can lead to lighter isotopic composition in early to mid-Holocene needs further exploration.

Finally, recent studies suggest a northward and inland shift of precipitation under enhanced summer insolation (Battisti et al., 2014; Boos & Korty, 2016). Battisti et al. (2014) suggest that a shift of precipitation toward land under high insolation can be understood based on the coincidence of precipitation maxima and near-surface entropy maxima (Boos & Kuang, 2010; Privé & Plumb, 2007). Boos & Korty (2016) proposed a theory that high precipitation occurs over regions with energy flux potential divergent from the region; based on this theory, they predict northward and inland shift of precipitation under mid-Holocene insolation. These findings suggest a new interpretation of East Asian precipitation changes in early to mid-Holocene. It raises the question of whether the altered seasonality of jet transition and the rainfall transition are simply two independent responses to orbital forcing. I speculate that during the early Holocene, enhanced summer insolation brought more precipitation inland, while it is the perturbations in the jet latitudes that determined changes in the rainfall stages.

Mega-droughts during the last millennium

East Asia underwent several severe droughts episodes during the last millennium, some of them even last at centennial time scale (Cook et al., 2010). Previous findings suggest that the external forcings (such as ENSO, solar activity, and volcanic eruptions) are major culprits of the monsoon failures. The underlying mechanism, however, remains inconclusive. An

intriguing feature of these mega-droughts is that the leading mode of the tree-ring constructed rainfall distribution (Cook et al., 2010) resembles the "tripole" pattern seen in the EASM variability at interannual timescales (Hsu & Lin, 2007). It is worth exploring whether the mega-droughts resulted from altered seasonality of the EASM, and whether perturbations in westerlies play a role. Recent progress of the digitalization of climate database based on historical records (Wang et al., 2018), the Last Millennium Reanalysis (Tardif et al., 2019), and the CESM Last Millennium ensemble project (Otto-Bliesner et al., 2015) provide a good start to address these problems.

Uplift of the northern Tibetan Plateau

Chapter 3 proposed that the northern edge of the Tibetan Plateau is a latitude threshold that marks the transition from mei-yu to midsummer. Geological studies suggest that the northern part of the plateau started to rise around 10 Ma (An et al., 2001). Before that, the northern edge of the plateau was 3-4 degrees south of its present-day latitude. The EASM evolution during that time is thus an interesting test bed for our hypothesis of jet's control on the rainfall seasonality. Per our hypothesis (chapter 3), the mei-yu before 10 Ma should be shorter than today, because the jet transition should occur more rapidly across the plateau with reduced meridional extension. However, I also note that a significant challenge remains to test this hypothesis because of the lack of proxies back then.

Appendix A

Appendix to Chapter 2

A.1 The Seasonal Transition of EASM in the 6-ka and PI Simulations from PMIP3

The results of our analysis were derived solely from simulations of one atmospheric general circulation model (CAM5). To test our hypothesis using more realistic coupled model simulations, we analyze the standard preindustrial (PI) and mid-Holocene (6 ka) simulations from the PMIP3 models (Braconnot et al., 2012). Although the ensemble mean of the PI reproduces the spatial pattern of summer monsoonal rainfall (Zheng et al., 2013) at a gross level, GCMs generally fail to simulate the fine structure of the EASM seasonal evolution. Our own analysis reveals that only four models—CCSM4 (Gent et al., 2011), BCC-CSM1.1 (Wu et al., 2013), FGOALS-g2 (Li et al., 2013), and FGOALS-s2 (Bao et al., 2013)—out of the 13 that we analyze are able to simulate the seasonal transition of EASM in the PI simulation with fidelity (Figs. A.1e–h). Note that the timing of the mei-yu onset in these models is delayed compared with the present day (Fig. 2.1), and a disparity in the intensity and timing of the EASM is evident among the four models (Figs. A.1e–h). Basic information on the four models is listed in Table A.1.

Compared with PI, it is visually apparent in the precipitation field that the 6-ka simulations in each of these four models possess an earlier onset of mei-yu and mid-summer, and longer duration of midsummer stage (Figs. A.1a–d). The difference (6 ka minus PI) (Figs. A.1i–l) suggests a "wet north and dry south" pattern around late June and early July, indicating an earlier onset of mei-yu in 6 ka. The overall wet north and dry south pattern persists from late June to mid-September in CCSM4, BCC-CSM1.1, and FGOALS-g2 (Figs. A.1i–k), suggesting that the midsummer pattern starts earlier and persists longer over northern China in the 6-ka simulations. Note that for FGOALS-s2 the deficit in the July–August rainfall over northern China (Fig. A.1l) is mainly due to the reduced intensity of midsummer rainfall in 6 ka (Fig. A.1d). (Figure A.2) shows the zonal wind over East Asia in summer (JJA), based on the multimodel ensemble mean from the four models. All the model outputs are interpolated onto the same grid as CCSM4 using bilinear interpolation.

The 6-ka minus PI difference (color shading in Fig. A.2) features strengthened westerlies on the northern flank of the PI jet core (contour in Fig. A.2) and weakened westerlies on the southern flank of the PI jet core, suggesting an earlier northward shift of westerlies in the simulated mid-Holocene. These results further support our argument that a northward shift of the westerlies in the early to mid-Holocene led to an earlier seasonal transition of EASM during that time.

Table A.1: Basic information for the four PMIP3 models.(Expansions of acronyms are available online at http://www.ametsoc.org/PubsAcronymList).

Model	Atmospheric resolution (lat x lon)	Length of analyzed outputs (yr) 6ka, PI	References
BCC-CSM1.1	64 × 128	100, 100	Wu et al. (2013)
CCSM4	192 × 288	32, 20	Gent et al. (2011)
FGOALS-g2	60 × 128	30, 40	Li et al. (2013)
FGOALS-s2	108 × 128	50, 50	Bao et al. (2013)

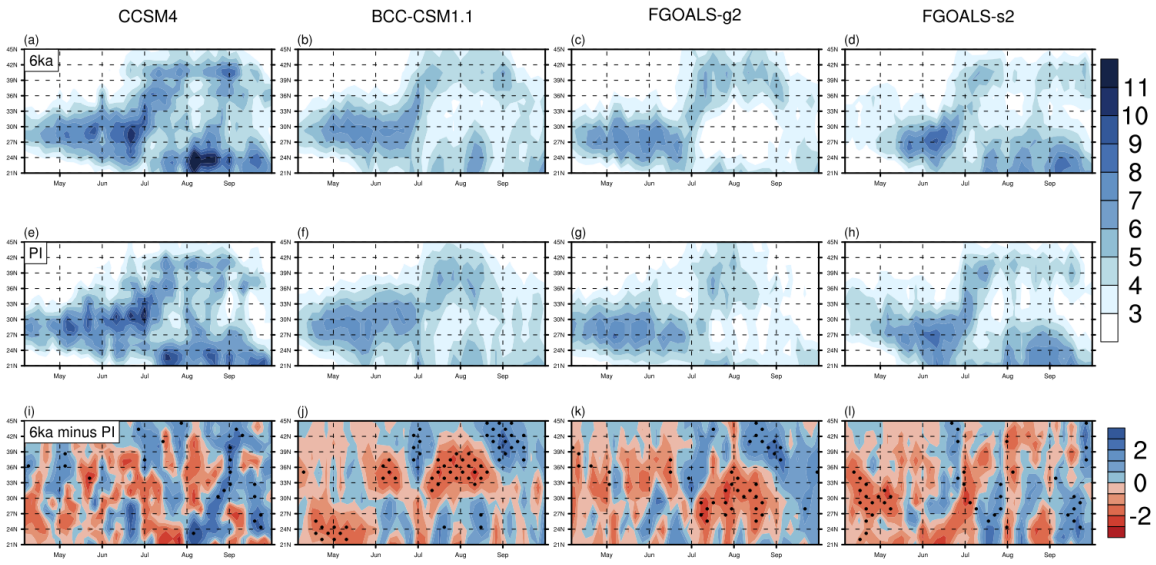

Figure A.1: Hovmöller diagram of precipitation (110°–120° E) from CCSM4, BCC-CSM1.1, FGOALS-g2, and FGOALS-s2, for (top) the 6-ka simulations and (middle) the PI simulations, and (bottom) 6 ka minus PI. Unit is $\mathrm{mm\,d^{-1}}$. The stippled areas indicate that the difference is statistically significant at the confidence level of 90 %.

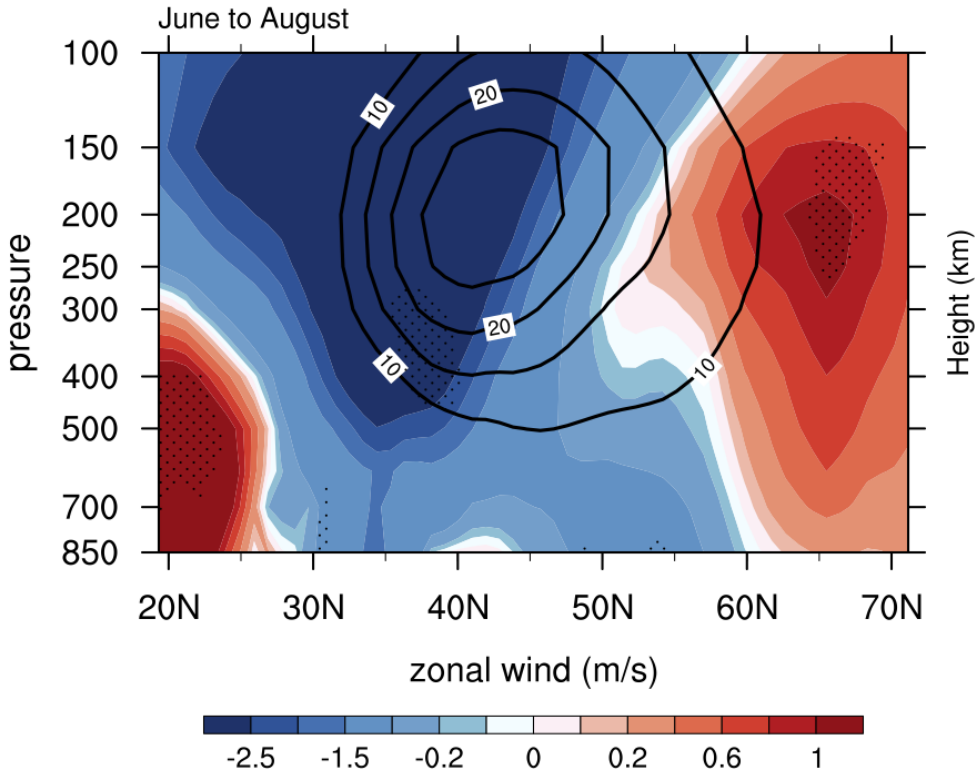

Figure A.2: JJA zonal wind (80°–120° E) from the multimodel ensemble mean of CCSM4, BCC-CSM1.1, FGOALS-g2, and FGOALS-s2 (contour: PI; shading: 6 ka minus PI; unit: $\mathrm{m\,s^{-1}}$). The stippled areas indicate that the difference is statistically significant at the confidence level of 90 %.

Appendix B

Appendix to Chapter 3

B.1 Topography for the Extended Plateau Simulations and the Leading EOF Mode of July-August Precipitation

Figure B.1 shows the boundary topography used in the extended plateau simulations, and Figure B.2 shows the leading EOF mode of July–August precipitation in East Asia.

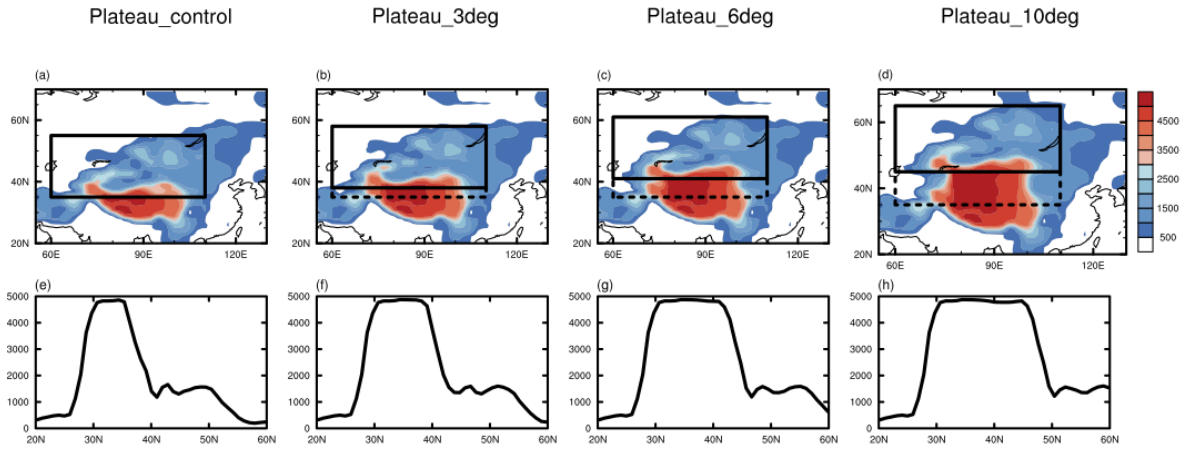

Figure B.1: Boundary topography (unit: meters) for (a),(e) the Plateau_control run and (b)–(d),(f)–(h) the extended plateau simulations. (top) The distribution of topography in East Asia, and (bottom) the vertical cross section of elevation averaged over 80°–100°E.

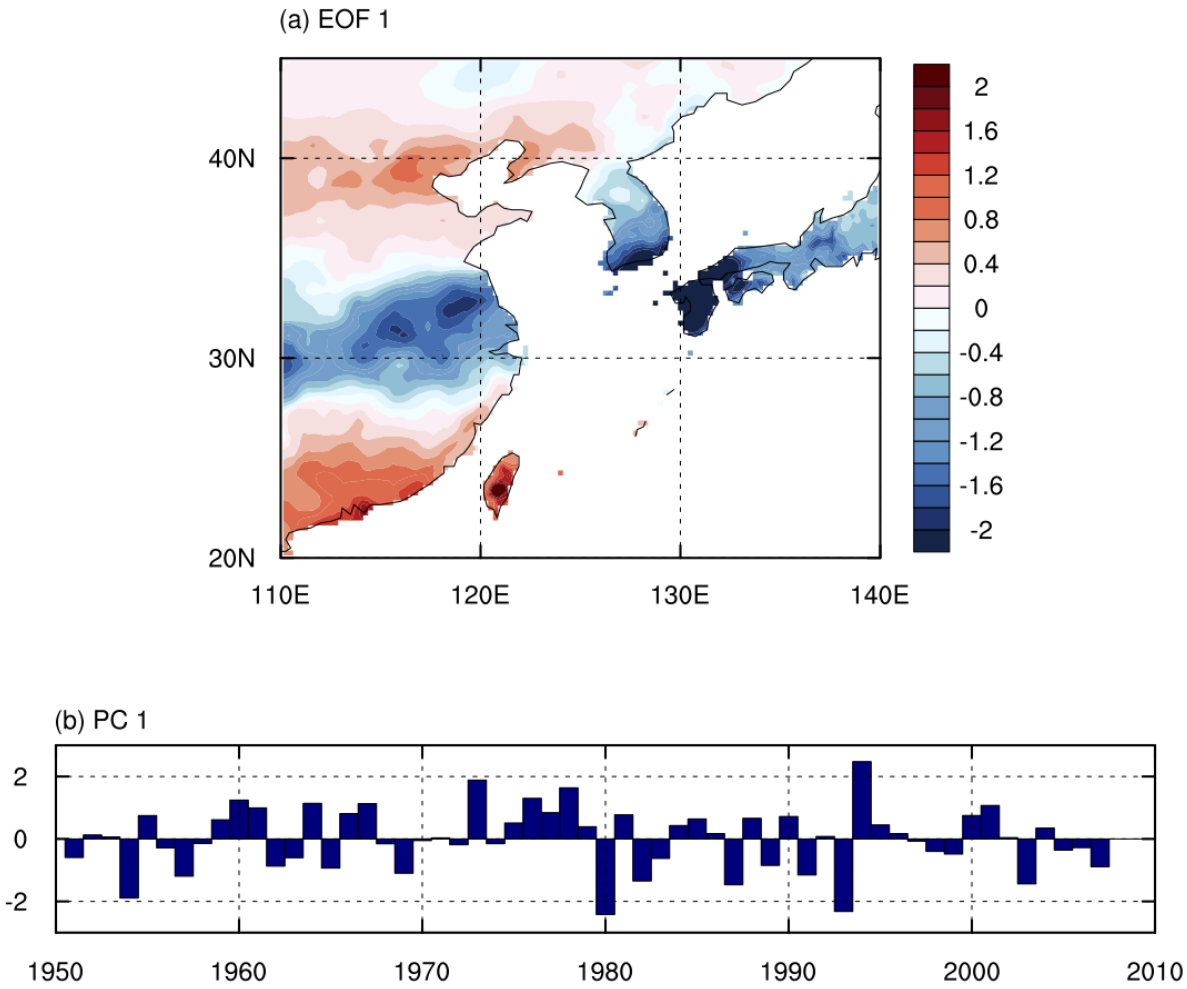

Figure B.2: The (a) first EOF and (b) principal component of July–August mean precipitation over East Asia (100°–145° E, 20°–45° N). The spatial pattern is the regression of the normalized PC1 onto the July–August rainfall anomaly (mm d^{-1} per standard deviation). The first mode is the well-known tripole pattern (Hsu & Lin, 2007) with reduced rainfall over central eastern China and Japan and increased rainfall over northeastern and southeastern China. We use the APHRODITE dataset spanning 1951–2007. The mode explains 17 7 of the total variance. Adopted from Chiang et al. (2017) and reproduced based on Figs. 1b and 1c of Chiang et al. (2017).

Appendix C

Appendix to Chapter 4

C.1 Banded and non-banded rainfall dataset

We employed a rainfall dataset derived by the Frontal Rain Event Detection Algorithm (Day et al., 2018), who partitioned East Asian summer rainfall into "banded" rainfall and "local" (or non-banded) rainfall. The "banded" rainfall is associated with large-scale convergence, while the "local" rainfall is driven by local buoyancy or topography. This dataset covers 1951 to 2007, and we examine the 33 neutral summers and 12 El Niño decaying summers during this period. Figure C.1 and C.2 present the composites of the raw precipitation, the primary rain band, the secondary rain band and the local rainfall. The reader is referred to Day et al. (2018) for further details about the dataset.

C.2 Moisture budget analysis

We write the changes (δ) of vertically integrated moisture flux convergence between summer following El Niño and neutral summer as follows,

$$\delta(\overline{P}-\overline{E}) = -\delta\{\overline{\langle\nabla\cdot(\mathbf{v}\cdot q)\rangle}\} = -\delta\{\langle\nabla\cdot(\overline{\mathbf{v}}\,\overline{q})\rangle\} - \delta(trans), \tag{C.1}$$

where δ indicates summer following El Niño minus neutral summer. Equation (C.1) can be written as below by further decomposition of the term $-\delta\{\overline{\langle\nabla\cdot(\mathbf{v}\cdot q)\rangle}\}$:

$$\underbrace{-\delta\{\overline{\langle\nabla\cdot(\mathbf{v}\cdot q)\rangle}\}}_{\text{A}} = \underbrace{-\langle\nabla\cdot(\overline{\mathbf{v}}\cdot\delta\overline{q})\rangle}_{\text{B}} \underbrace{-\langle\nabla\cdot(\delta\overline{\mathbf{v}}\cdot\overline{q})\rangle}_{\text{C}} \underbrace{-\langle\nabla\cdot(\delta\overline{\mathbf{v}}\cdot\delta\overline{q})\rangle}_{\text{D}} \underbrace{-\delta(trans)}_{\text{E}}, \tag{C.2}$$

where A indicates changes of vertically integrated moisture flux convergence, B is contribution by changes to the specific humidity, C is contribution by changes to the horizontal winds, D is contribution by changes to both specific humidity and horizontal winds, and E is contribution by submonthly transients. Note that variables without δ in B and C represent neutral summer.

C.3 East Asian rainband during summers following three extreme El Niño (1982/83, 1986/87, 1997/98)

We repeat the analysis in the main manuscript for summers following three extreme El Niño, i.e., 1982/83, 1986/87, and 1997/98; results are shown in Figures C.13-C.17. They suggest pronounced rainband intensification for both June and July following strong El Niño events. Further, the rainband intensification from both months are closely tied to the strengthening of westerlies over the Tibetan Plateau and the resulted enhancement of extratropical northerlies downstream of the plateau.

Table C.1: Classification of DJF ENSO phase from 1950/51 to 2014/15. Years indicated correspond to December (e.g., 1950 is December 1950 to February 1951).

Phase (No. of DJFs)	DJF years
El Niño (13)	1957, 1963, 1965, 1968, 1972, 1977, 1982, 1986, 1991, 1994, 1997, 2002, 2009
Neutral (36)	1951, 1952, 1953, 1954, 1956, 1958, 1959, 1960, 1961, 1962, 1964, 1966, 1967, 1969, 1971, 1974, 1976, 1978, 1979, 1980, 1981, 1985, 1987, 1989, 1990, 1992, 1993, 1995, 1996, 2001, 2003, 2004, 2006, 2012, 2013, 2014
La Niña (16)	1950, 1955, 1970, 1973, 1975, 1983, 1984, 1988, 1998, 1999, 2000, 2005, 2007, 2008, 2010, 2011

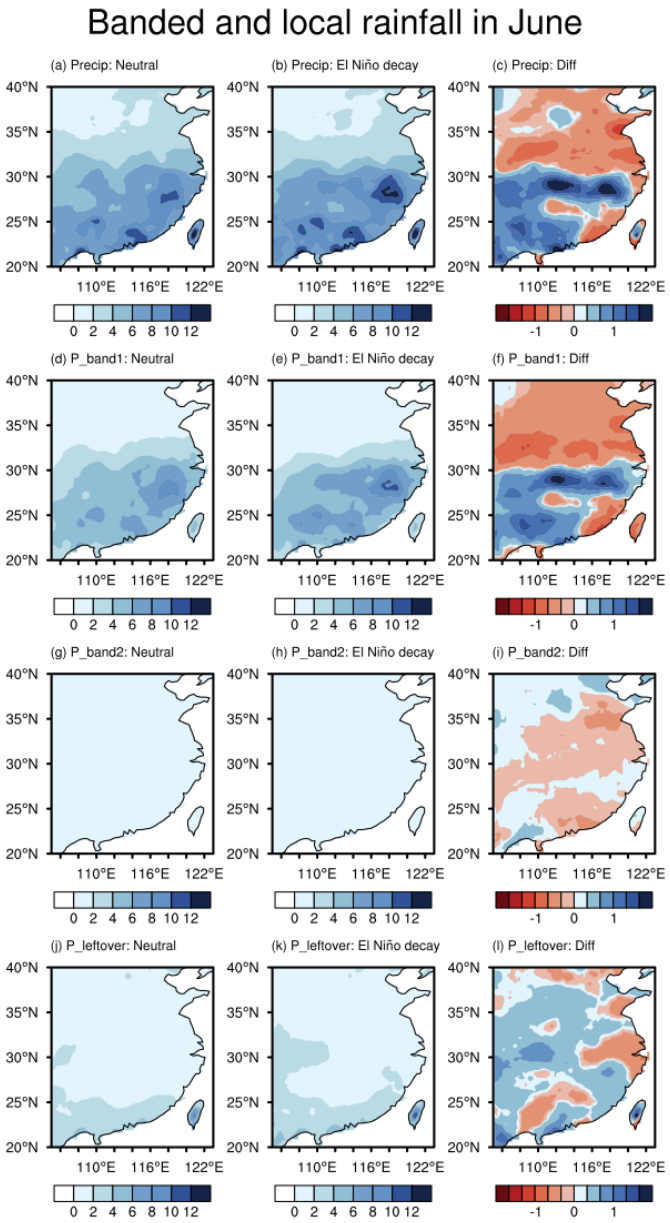

Figure C.1: Composites of the (the first row) total precipitation, (the second row) primary banded rainfall, (the third row) secondary banded rainfall, and (the fourth row) local rainfall in June. The left column shows results from neutral summer, the middle column shows results from the summer following El Niño, and the right column presents the latter minus the former. The dataset is from Day et al. (2018).

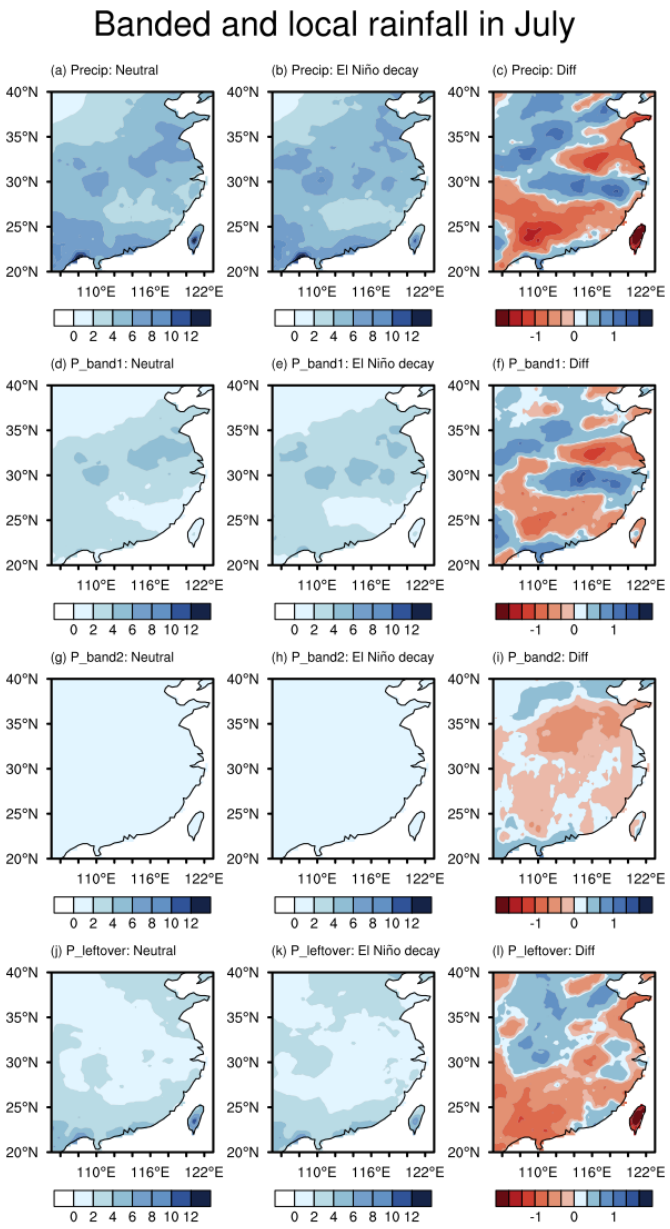

Figure C.2: Similar to Figure C.1, except for July.

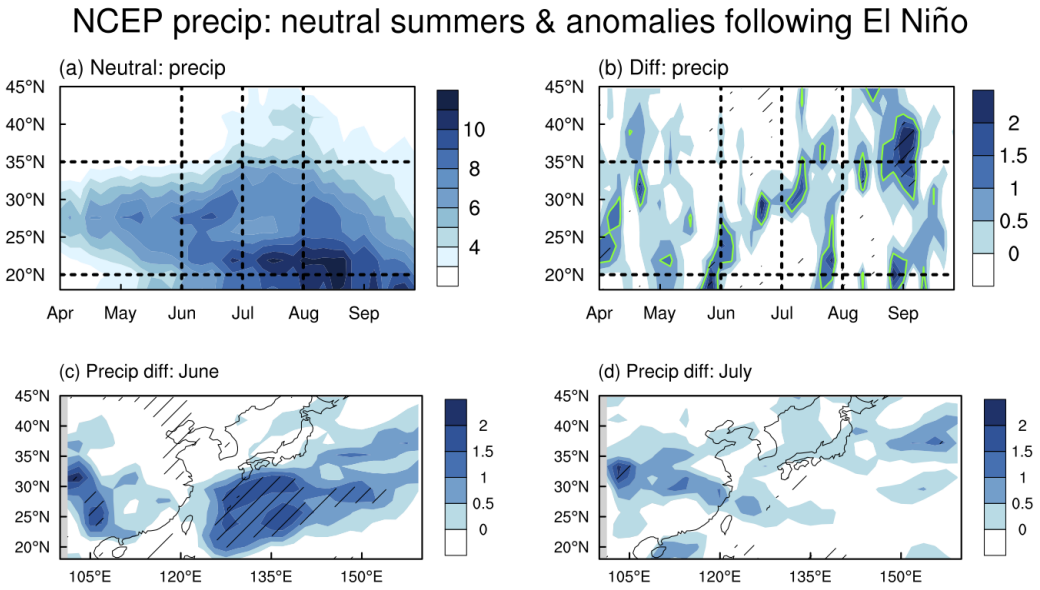

Figure C.3: Similar to the precipitation analysis as in Figure 4.1, but for the precipitation rate from the NCEP/NCAR-1 reanalysis product. This figure shows the NCEP/NCAR-1 precipitation from the same 13 El Niño events and 36 neutral ENSO events (identified from 1950/51 to 2014/15 based on section 2.3) analyzed in figure 1. (a)-(b) Hovmöller diagrams of precipitation in 105°E-125°E of (a) neutral summers and (b) anomalies during summers following El Niño. (c)-(d) Precipitation anomalies during summers following El Niño in (c) June and (d) July. Green contours in (b) highlights the precipitation anomalies exceeding $1\,\mathrm{mm\,d^{-1}}$. Hatched area indicates that difference between the two categories exceeds statistical significance level at 90 %.

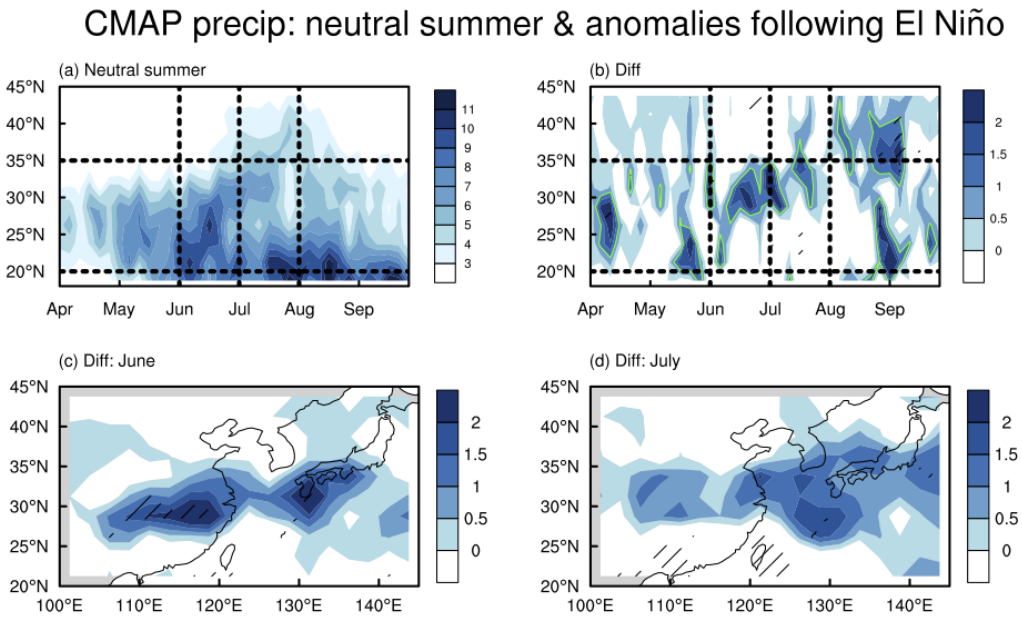

Figure C.4: Similar to Figure C.3, but for the CMAP (CPC Merged Analysis of Precipitation) precipitation dataset from 1979 to 2016. Note that the CMAP product does not cover period before 1979, so the results shown are based on 12 El Niño events and 12 neutral ENSO events identified from 1979/80 to 2015/16.

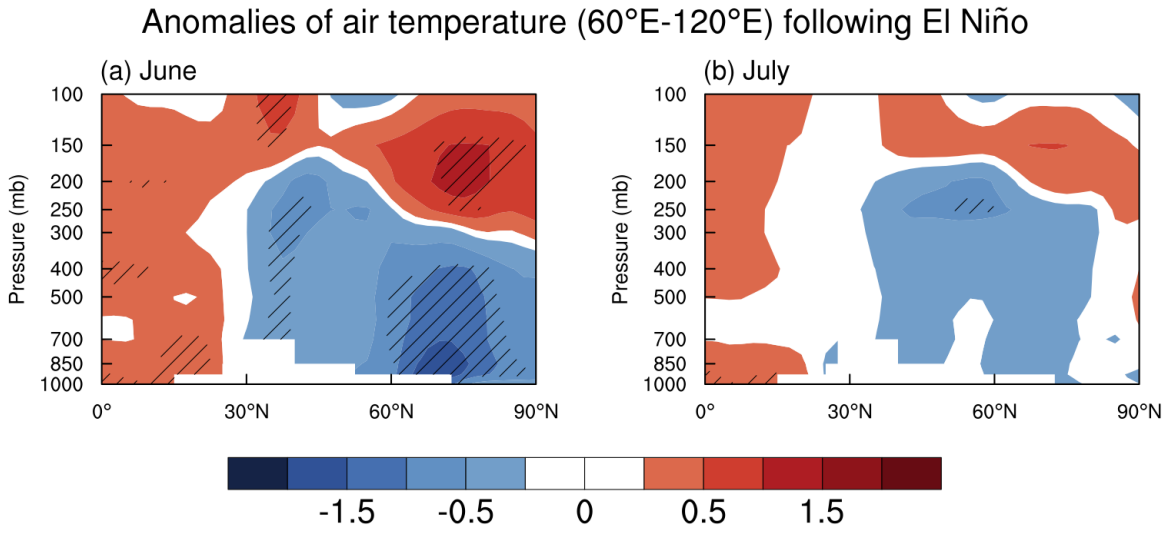

Figure C.5: Pressure-latitude cross section of air temperature anomalies averaged over 60°E-120°E, for (a) June and (b) July. Here, the temperature anomalies are calculated by subtracting values for the mean of neutral summers from the mean of summers following El Niño. Unit: °C. Hatched area indicates that difference between the two categories exceeds statistical significance level at 90.

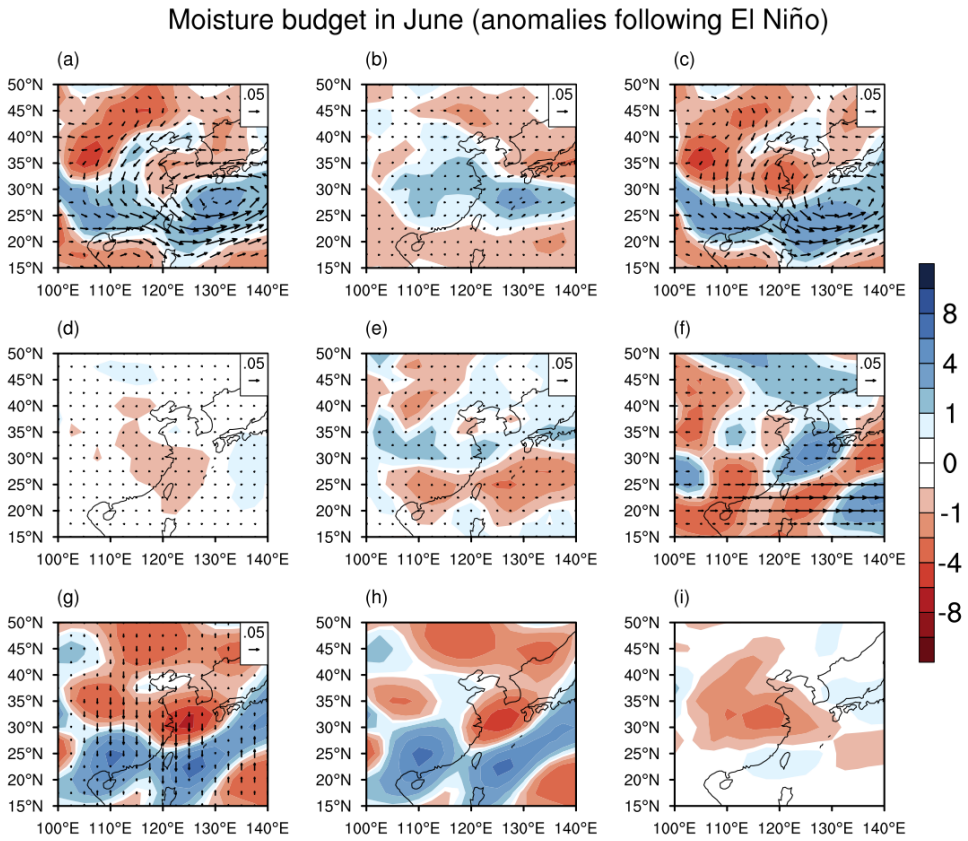

Figure C.6: Changes in the mass-weighted vertical integral (from 1000 to 300 mb) of moisture budget components in June between the summers following El Niño and neutral years (El Niño decay minus neutral). Vectors denote moisture fluxes ($m^2\,s^{-1}$), and color shadings denote moisture flux convergence (mm/d); cold color indicate convergence, and warm color indicates divergence). (a) Changes of moisture flux and its convergence. (b) Contributions by the changes of specific humidity. (c) Contributions by changes of horizontal winds. (d) Contributions by changes of both specific humidity and horizontal winds. (e) Contributions by changes of transients. (f) Contributions by changes to the zonal moisture flux and its convergence. (g) Contributions by changes to the meridional moisture flux and its convergence; (g) is contributed from two terms, with (h) showing the contributions by meridional wind convergence and (i) showing contributions by meridional advection of moisture.

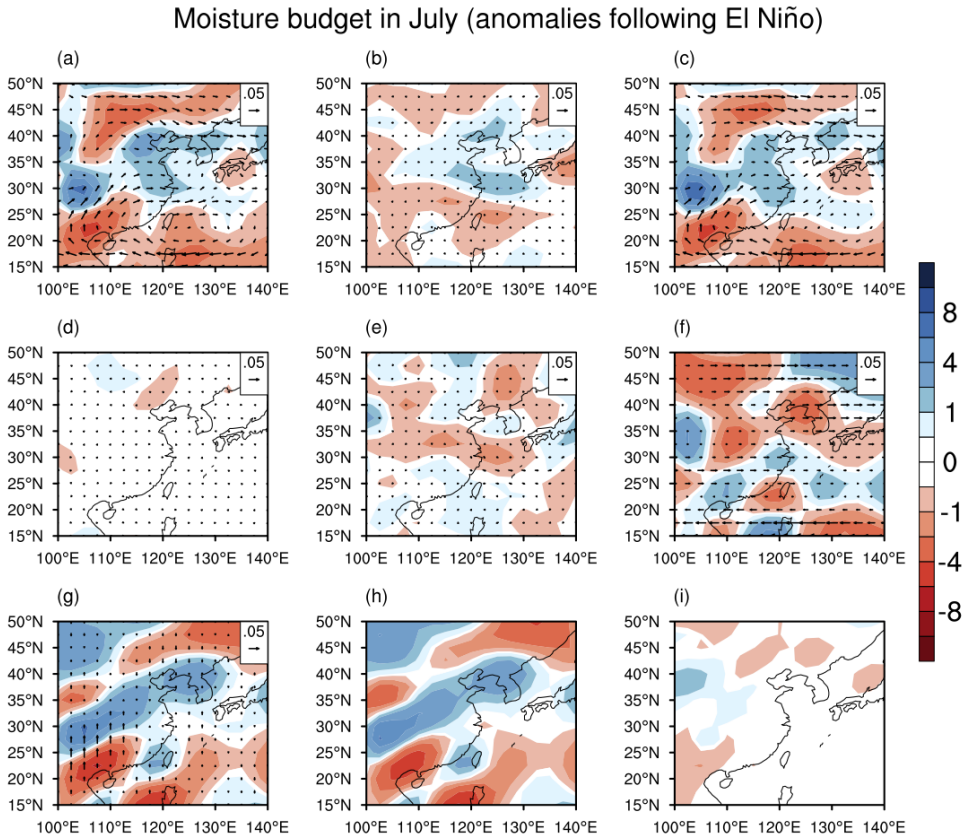

Figure C.7: Similar to Figure C.6, but for July.

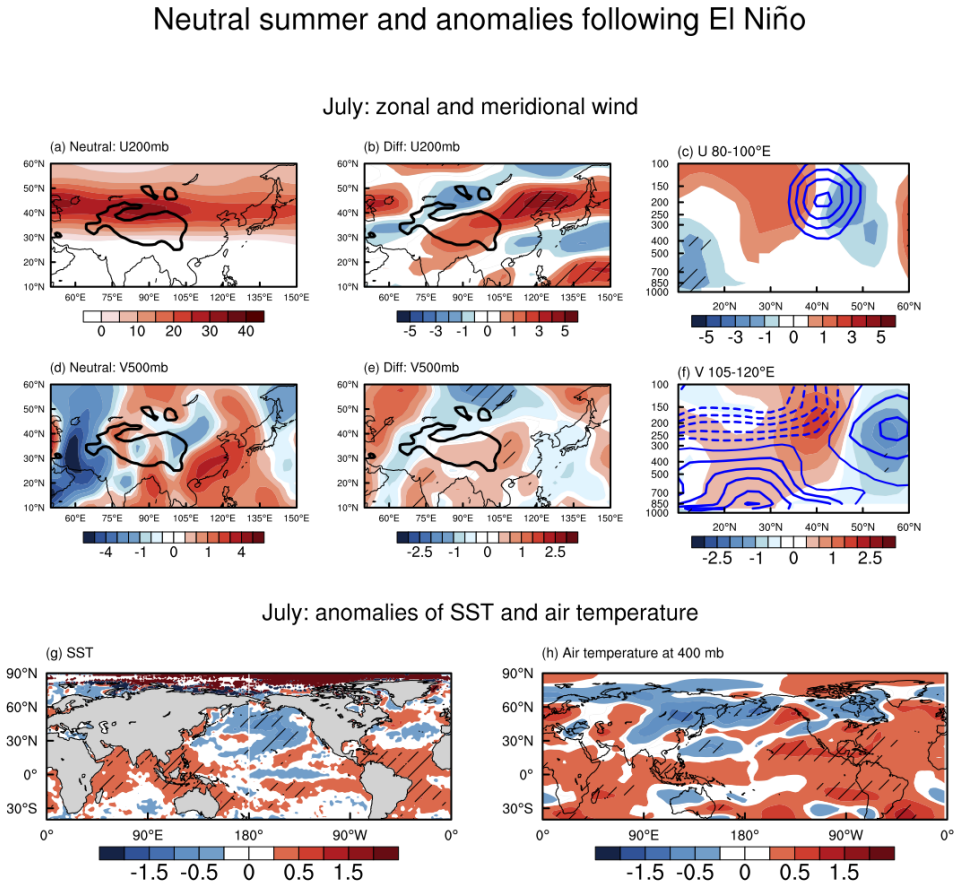

Figure C.8: Similar to Figure 4.2, but for July.

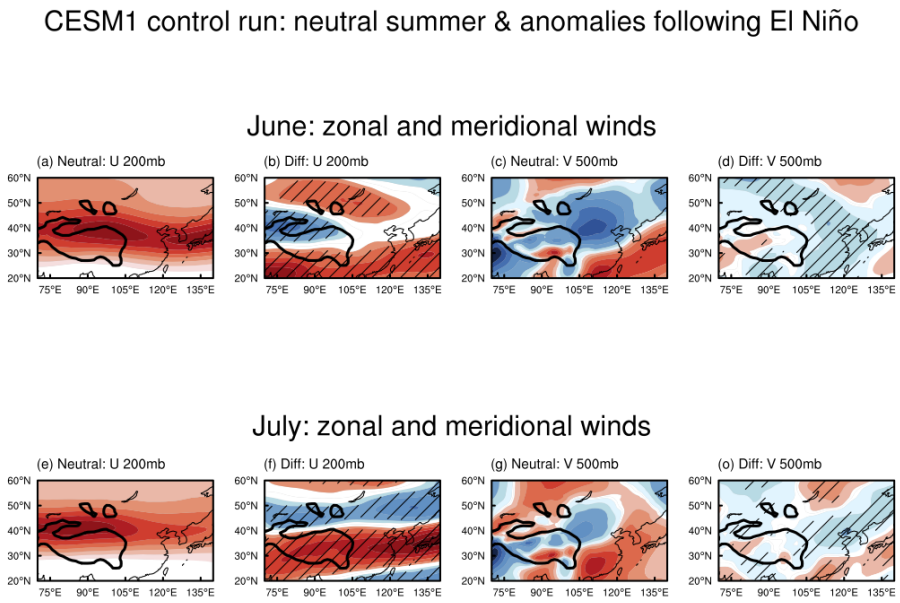

Figure C.9: Zonal and meridional winds in (top) June and (bottom) July from the CESM1 pre-industrial control run. (a)-(b) and (e)-(f) show zonal winds at 200 mb, and (c)-(d) and (g)-(h) show meridional winds at 500 mb. Results from neutral summers are shown in (a), (c), (e), and (g). Anomalies from summers following El Niño minus neutral summers are shown in (b), (d), (f), and (h). Hatched area indicates that difference between the two categories exceeds statistical significance level at 90 %. Units: $\mathrm{m\,s^{-1}}$. Black solid contours in these maps indicate areas where elevation exceeds 2000 meters.

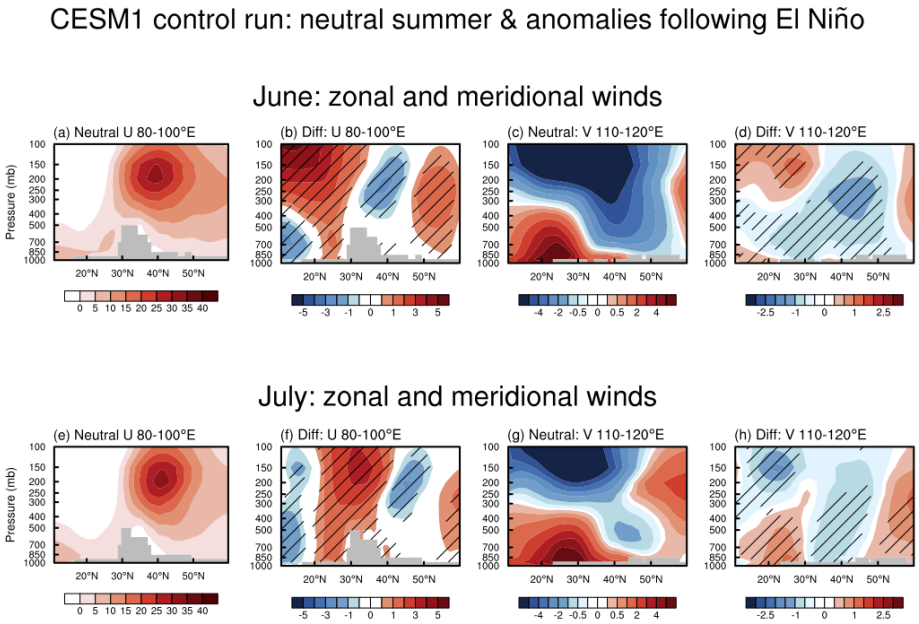

Figure C.10: Pressure-latitude cross section of zonal and meridional winds in (top) June and (bottom) July from the CESM1 pre-industrial control run. (a)-(b) and (e)-(f) show zonal winds averaged in 80°-100°E, and (c)-(d) and (g)-(h) show meridional winds averaged in 110°-120°E. Results from neutral summers are shown in (a), (c), (e), and (g). Anomalies from summers following El Niño minus neutral summers are shown in (b), (d), (f), and (h). Hatched area indicates that difference between the two categories exceeds statistical significance level at 90. Units: $\mathrm{m\,s^{-1}}$.

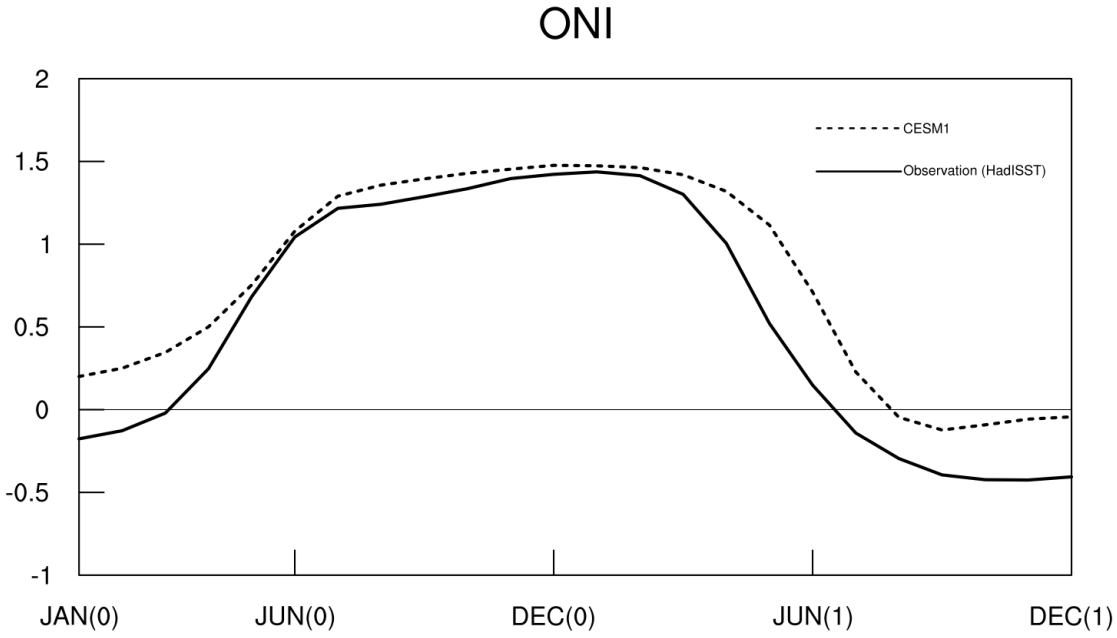

Figure C.11: Composite seasonal evolution of El Niño episodes from the HadISST (solid line) and the CESM1 control run (dashed line). Here, the El Niño episodes are the same as analyzed elsewhere in the main manuscript. The x-axis denotes the timing of the seasonal cycle, where "0" denotes the El Niño developing phase and "1" denotes the El Niño decaying phase. The y-axis denotes the monthly value of ONI, which is shown in the solid and dashed lines.

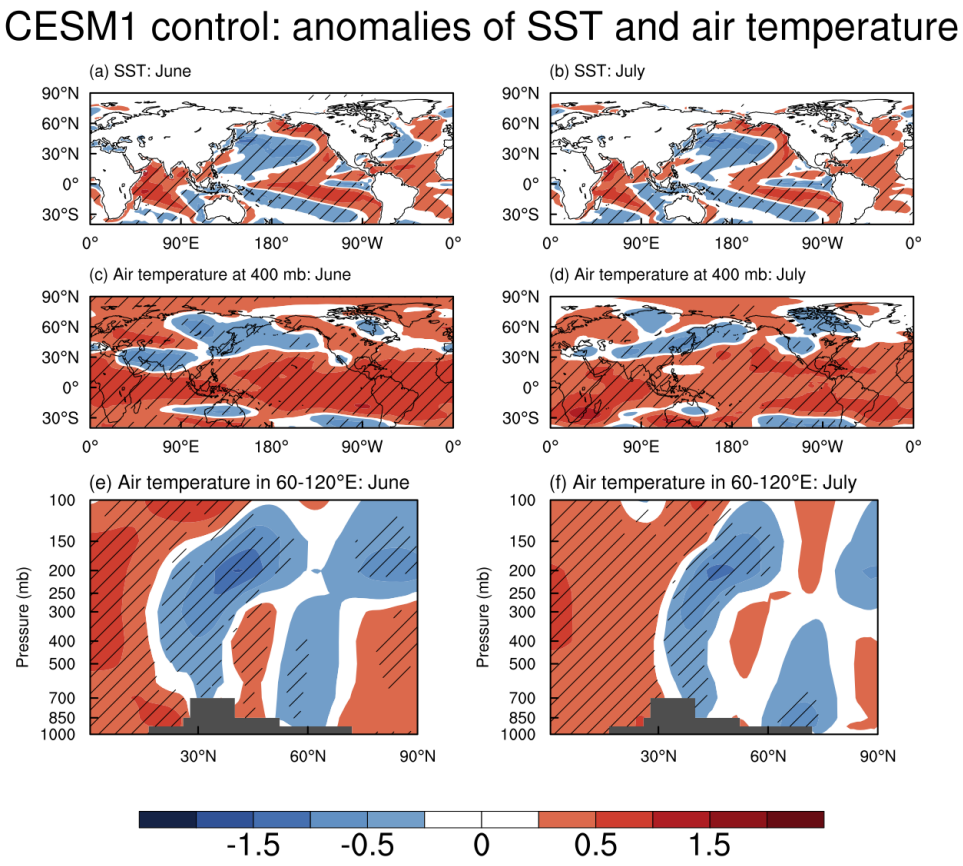

Figure C.12: Sea surface temperature (SST) and air temperature anomalies from summers following El Niño minus neutral summers in (a), (c), (e) June, and (b), (d), (f) July. Results are from the CESM1 fully coupled pre-industrial simulation. (a)-(b) SST, (c)-(d) air temperature at 400 mb, and (e)-(f) air temperature averaged in 60°-120°E. Unit: °C. Hatched area indicates that difference between the two categories exceeds statistical significance level at 90 %.

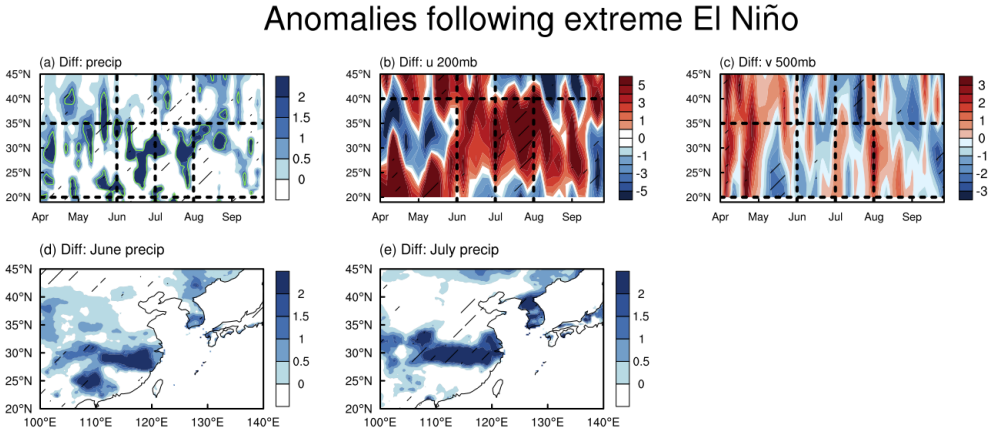

Figure C.13: Anomalies of the APHRODITE rain gauge (unit: $\mathrm{mm\,d^{-1}}$), upper tropospheric zonal wind and mid-tropospheric meridional wind (unit: $\mathrm{m\,s^{-1}}$) from summers following three extreme El Niño (1982/83, 1986/87, and 1997/98) minus neutral summers. (a)-(c) Hovmöller diagram of (a) precipitation averaged in 105°-120°E, (b) 200mb zonal wind averaged in 80°-100°E, and (c) 500mb meridional wind averaged in 105°-120°E. (d)-(e) Precipitation anomalies in (d) June and (e) July. Hatched area indicates that difference between the two categories exceeds statistical significance level at 90 %.

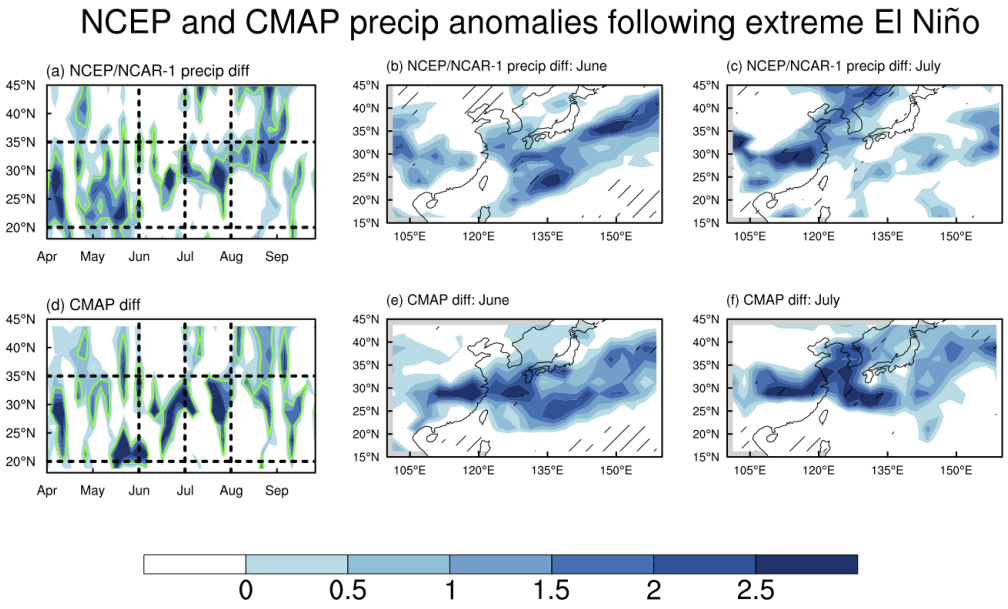

Figure C.14: Anomalies of the NCEP/NCAR-1 precipitation and the CMAP product during summers following three extreme El Niño (1982/83, 1986/87, and 1997/98) (unit: $\mathrm{mm\,d^{-1}}$). (a) and (d) present hovmöller diagram of precipitation anomalies averaged in 105°-120°E, where the green contour highlights anomalies exceeding $1\,\mathrm{mm\,d^{-1}}$. (b) and (e) show precipitation anomalies in June, and (c) and (f) show precipitation anomalies in July. The anomalies are calculated by subtracting composites of summers following the three extreme El Niño from neutral summers. Note that we used the 36 neutral summers identified from section 4.2.3 for the NCEP/NCAR-1 precipitation calculation, and we used 12 neutral summers identified during 1979/80 to 2015/16 for the CMAP calculation. Hatched area indicates that difference between the two categories exceeds statistical significance level at 90 %.

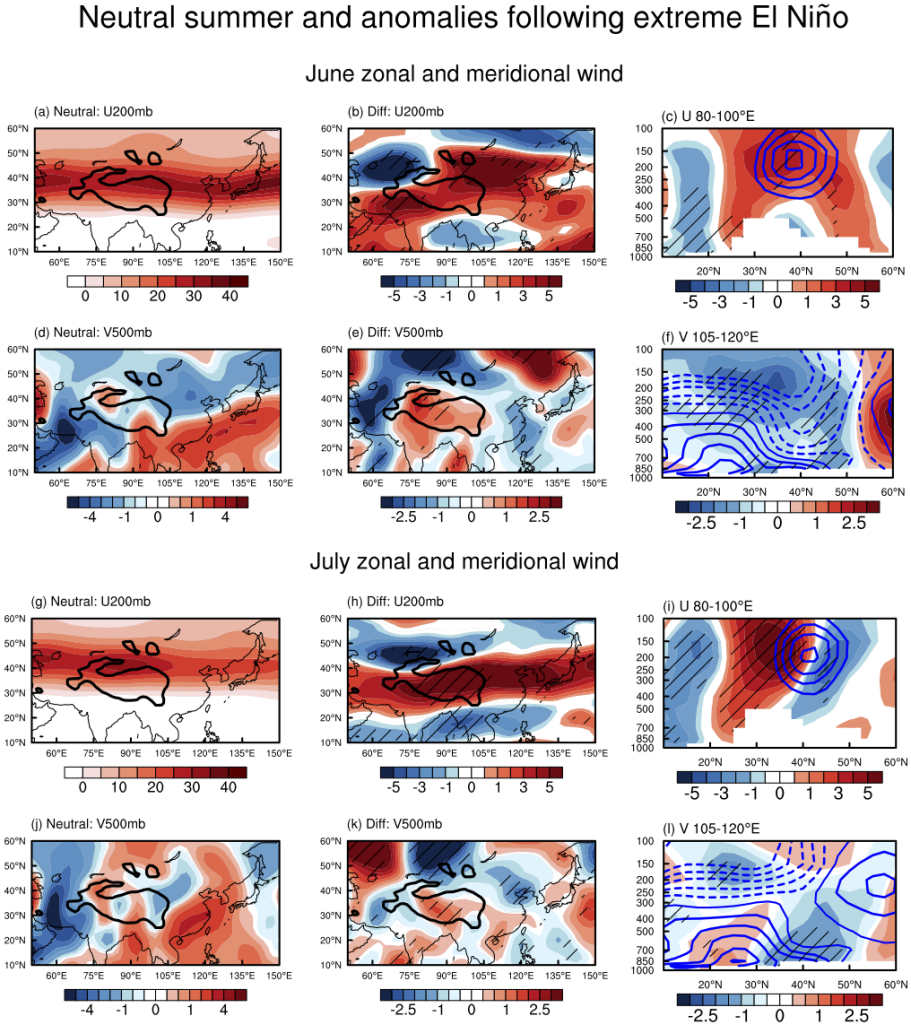

Figure C.15: Similar to Figures 4.2a-f, but for June and July zonal and meridional winds during neutral summers and anomalies following the three extreme El Niño (1982/83, 1986/87, and 1997/98).

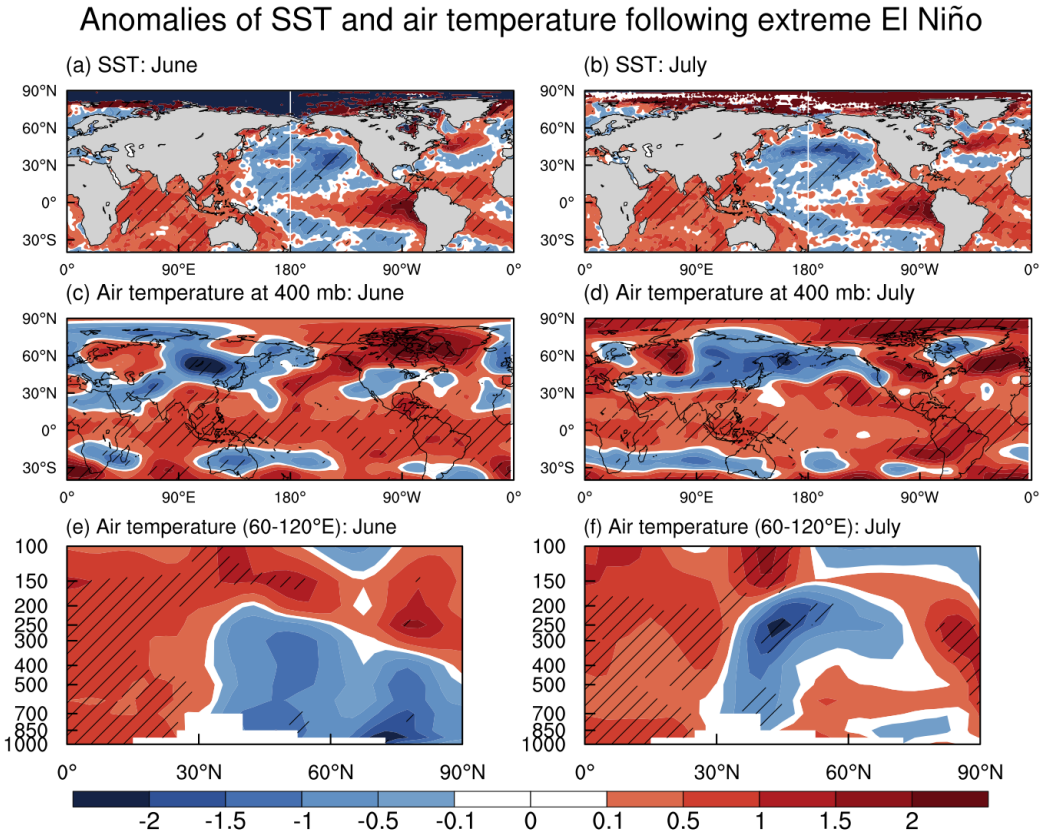

Figure C.16: Sea surface temperature (SST) and air temperature anomalies from summers following three extreme El Niño (1982/83, 1986/87, and 1997/98) minus neutral summers in (a), (c), (e) June, and (b), (d), (f) July. (a)-(b) SST, (c)-(d) air temperature at 400 mb, and (e)-(f) air temperature averaged in 60°-120°E. Unit: °C. Hatched area indicates that difference between the two categories exceeds statistical significance level at 90 %.

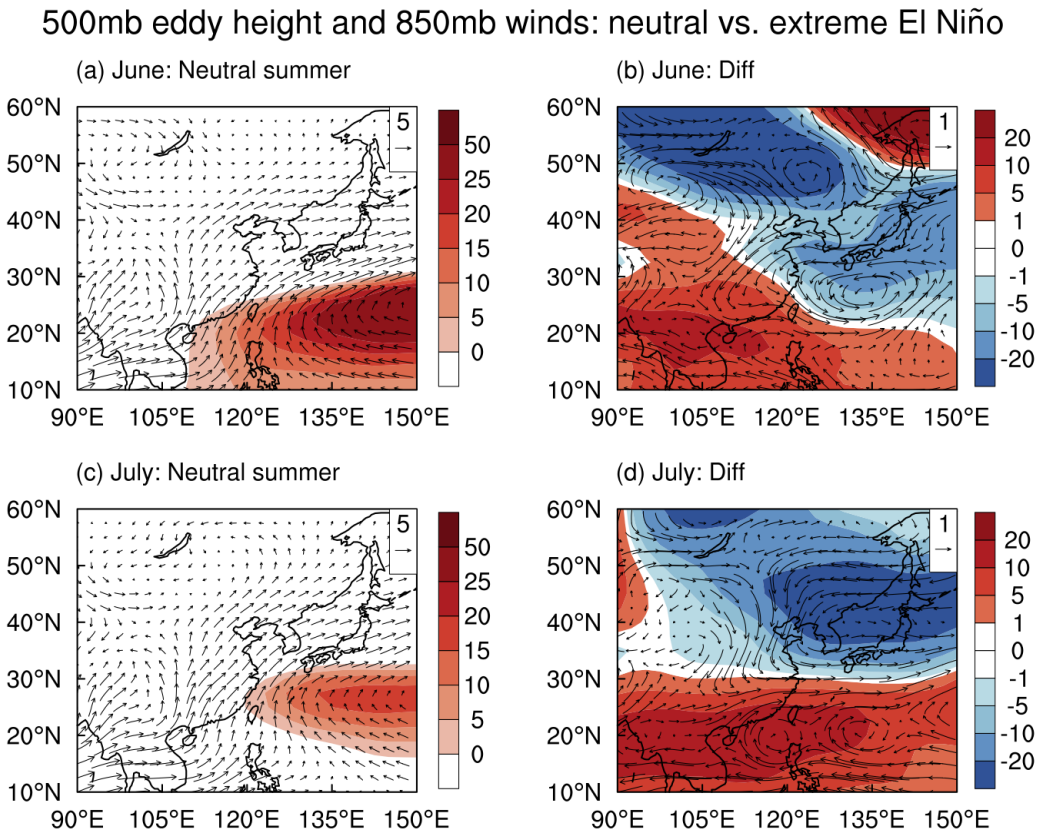

Figure C.17: Eddy geopotential height at 500 mb (colors shading, unit: meters) and horizontal winds at 850 mb (vectors, unit: $\mathrm{m\,s^{-1}}$) during (a)-(b) June and (c)-(d) July. (a) and (c) show results from neutral summers, and (b) and (d) show results from anomalies during summers following the three extreme El Niño (1982/83, 1986/87, and 1997/98).

Bibliography

An, Z., Colman, S. M., Zhou, W., Li, X., Brown, E. T., Jull, A. J. T., Cai, Y., Huang, Y., Lu, X., Chang, H., Song, Y., Sun, Y., Xu, H., Liu, W., Jin, Z., Liu, X., Cheng, P., Liu, Y., Ai, L., Li, X., Liu, X., Yan, L., Shi, Z., Wang, X., Wu, F., Qiang, X., Dong, J., Lu, F., & Xu, X. (2012). Interplay between the Westerlies and Asian monsoon recorded in Lake Qinghai sediments since 32 ka. *Scientific Reports*, *2*.

An, Z., Kutzbach, J. E., Prell, W. L., & Porter, S. C. (2001). Evolution of Asian monsoons and phased uplift of the Himalaya–Tibetan plateau since Late Miocene times. *Nature*, *411*(6833), 62–66.

An, Z., Porter, S. C., Kutzbach, J. E., Xihao, W., Suming, W., Xiaodong, L., Xiaoqiang, L., & Weijian, Z. (2000). Asynchronous Holocene optimum of the East Asian monsoon. *Quaternary Science Reviews*, *19*(8), 743–762.

Baldwin, J., & Vecchi, G. (2016). Influence of the Tian Shan on Arid Extratropical Asia. *Journal of Climate*, *29*(16), 5741–5762.

Bao, M., & Wallace, J. M. (2015). Cluster Analysis of Northern Hemisphere Wintertime 500-hPa Flow Regimes during 1920–2014. *Journal of the Atmospheric Sciences*, *72*(9), 3597–3608.

Bao, Q., Lin, P., Zhou, T., Liu, Y., Yu, Y., Wu, G., He, B., He, J., Li, L., Li, J., , Y. L., , H. L., , F. Q., , Z. S., , B. W. , J. W. , P. W., , X. W., , Z. W., , B. W. , T. W., , Y. X., , H. Y., , W. Z. , W. Z., & , L. Z. (2013). The Flexible Global Ocean-Atmosphere-Land system model, Spectral Version 2: FGOALS-s2. *Advances in Atmospheric Sciences*, *30*(3), 561–576.

Battisti, D. S., Ding, Q., & Roe, G. H. (2014). Coherent pan-Asian climatic and isotopic response to orbital forcing of tropical insolation. *Journal of Geophysical Research: Atmospheres*, *119*(21), 11,997–12,020.

Berger, A., Loutre, M.-F., & Tricot, C. (1993). Insolation and Earth's orbital periods. *Journal of Geophysical Research: Atmospheres*, *98*(D6), 10341–10362.

Bolin, B. (1950). On the Influence of the Earth's Orography on the General Character of the Westerlies. *Tellus*, *2*(3), 184–195.

Boos, W. R., & Korty, R. L. (2016). Regional energy budget control of the intertropical convergence zone and application to mid-Holocene rainfall. *Nature Geoscience*, *9*(12), 892–897.

Boos, W. R., & Kuang, Z. (2010). Dominant control of the South Asian monsoon by

orographic insulation versus plateau heating. *Nature*, *463*(7278), 218–222.

Braconnot, P., Harrison, S. P., Kageyama, M., Bartlein, P. J., Masson-Delmotte, V., Abe-Ouchi, A., Otto-Bliesner, B., & Zhao, Y. (2012). Evaluation of climate models using palaeoclimatic data. *Nature Climate Change*, *2*(6), 417–424.

Broccoli, A. J., & Manabe, S. (1992). The Effects of Orography on Midlatitude Northern Hemisphere Dry Climates. *Journal of Climate*, *5*(11), 1181–1201.

Capotondi, A., Wittenberg, A. T., Newman, M., Di Lorenzo, E., Yu, J.-Y., Braconnot, P., Cole, J., Dewitte, B., Giese, B., Guilyardi, E., Jin, F.-F., Karnauskas, K., Kirtman, B., Lee, T., Schneider, N., Xue, Y., & Yeh, S.-W. (2014). Understanding ENSO Diversity. *Bulletin of the American Meteorological Society*, *96*(6), 921–938. Publisher: American Meteorological Society.

Chang, C.-H., & Johnson, N. C. (2015). The continuum of wintertime Southern Hemisphere atmospheric teleconnection patterns. *Journal of Climate*.

Chang, C.-P., Zhang, Y., & Li, T. (2000). Interannual and Interdecadal Variations of the East Asian Summer Monsoon and Tropical Pacific SSTs. Part I: Roles of the Subtropical Ridge. *Journal of Climate*, *13*(24), 4310–4325.

Charney, J. G., & Eliassen, A. (1949). A Numerical Method for Predicting the Perturbations of the Middle Latitude Westerlies. *Tellus*, *1*(2), 38–54.

Chattopadhyay, R., Sahai, A. K., & Goswami, B. N. (2008). Objective Identification of Nonlinear Convectively Coupled Phases of Monsoon Intraseasonal Oscillation: Implications for Prediction. *Journal of the Atmospheric Sciences*, *65*(5), 1549–1569.

Chen, J., & Bordoni, S. (2014). Orographic Effects of the Tibetan Plateau on the East Asian Summer Monsoon: An Energetic Perspective. *Journal of Climate*, *27*(8), 3052–3072.

Chen, J., & Bordoni, S. (2016). Early Summer Response of the East Asian Summer Monsoon to Atmospheric CO2 Forcing and Subsequent Sea Surface Warming. *Journal of Climate*, *29*(15), 5431–5446.

Chen, S.-J., Kuo, Y.-H., Wang, W., Tao, Z.-Y., & Cui, B. (1998). A Modeling Case Study of Heavy Rainstorms along the Mei-Yu Front. *Monthly Weather Review*, *126*(9), 2330–2351.

Chen, T.-J. G., & Chang, C.-P. (1980). The Structure and Vorticity Budget of an Early Summer Monsoon Trough (Mei-Yu) over Southeastern China and Japan. *Monthly Weather Review*, *108*(7), 942–953.

Chiang, J. C., Fung, I. Y., Wu, C.-H., Cai, Y., Edman, J. P., Liu, Y., Day, J. A., Bhattacharya, T., Mondal, Y., & Labrousse, C. A. (2015). Role of seasonal transitions and westerly jets in East Asian paleoclimate. *Quaternary Science Reviews*, *108*, 111–129.

Chiang, J. C. H., Fischer, J., Kong, W., & Herman, M. J. (2019). Intensification of the Pre-Meiyu Rainband in the Late 21st Century. *Geophysical Research Letters*, *46*(13), 7536–7545.

Chiang, J. C. H., Herman, M. J., Yoshimura, K., & Fung, I. Y. (2020). Enriched East Asian oxygen isotope of precipitation indicates reduced summer seasonality in regional climate and westerlies. *Proceedings of the National Academy of Sciences*, (p. 201922602).

Chiang, J. C. H., Kong, W., Wu, C.-H., & Battisti, D. S. (????). Origins of the East Asian Summer Monsoon Seasonality. *J. Climate*.

Chiang, J. C. H., & Lintner, B. R. (2005). Mechanisms of Remote Tropical Surface Warming during El Niño. *Journal of Climate*, *18*(20), 4130–4149.

Chiang, J. C. H., & Sobel, A. H. (2002). Tropical Tropospheric Temperature Variations Caused by ENSO and Their Influence on the Remote Tropical Climate. *Journal of Climate*, *15*(18), 2616–2631.

Chiang, J. C. H., Swenson, L. M., & Kong, W. (2017). Role of seasonal transitions and the westerlies in the interannual variability of the East Asian summer monsoon precipitation. *Geophysical Research Letters*, *44*(8), 2017GL072739.

Chou, C., & Neelin, J. D. (2003). Mechanisms Limiting the Northward Extent of the Northern Summer Monsoons over North America, Asia, and Africa. *Journal of Climate*, *16*(3), 406–425.

Chu, J.-E., Hameed, S. N., & Ha, K.-J. (2012). Nonlinear, Intraseasonal Phases of the East Asian Summer Monsoon: Extraction and Analysis Using Self-Organizing Maps. *Journal of Climate*, *25*(20), 6975–6988.

Cohen, N. Y., & Boos, W. R. (2017). The influence of orographic Rossby and gravity waves on rainfall. *Quarterly Journal of the Royal Meteorological Society*, *143*(703), 845–851.

Colman, R. A., Moise, A. F., & Hanson, L. I. (2011). Tropical Australian climate and the Australian monsoon as simulated by 23 CMIP3 models. *Journal of Geophysical Research: Atmospheres*, *116*(D10). _eprint: https://agupubs.onlinelibrary.wiley.com/doi/pdf/10.1029/2010JD015149.

Cook, E. R., Anchukaitis, K. J., Buckley, B. M., D'Arrigo, R. D., Jacoby, G. C., & Wright, W. E. (2010). Asian Monsoon Failure and Megadrought During the Last Millennium. *Science*, *328*(5977), 486–489.

Cook, K. H., & Held, I. M. (1988). Stationary Waves of the Ice Age Climate. *Journal of Climate*, *1*(8), 807–819. Publisher: American Meteorological Society.

Cook, K. H., & Held, I. M. (1992). The Stationary Response to Large-Scale Orography in a General Circulation Model and a Linear Model. *Journal of the Atmospheric Sciences*, *49*(6), 525–539.

Dansgaard, W. (1964). Stable isotopes in precipitation. *Tellus*, *16*(4), 436–468.

Dash, S. K. (2005). Monsoons and Monsoon Climate. In J. E. Oliver (Ed.) *Encyclopedia of World Climatology*, (pp. 509–516). Dordrecht: Springer Netherlands.

Day, J. A., Fung, I., & Liu, W. (2018). Changing character of rainfall in eastern China, 1951–2007. *Proceedings of the National Academy of Sciences*, (p. 201715386).

Dee, D. P., Uppala, S. M., Simmons, A. J., Berrisford, P., Poli, P., Kobayashi, S., Andrae, U., Balmaseda, M. A., Balsamo, G., Bauer, P., Bechtold, P., Beljaars, A. C. M., van de Berg, L., Bidlot, J., Bormann, N., Delsol, C., Dragani, R., Fuentes, M., Geer, A. J., Haimberger, L., Healy, S. B., Hersbach, H., Hólm, E. V., Isaksen, L., Kållberg, P., Köhler, M., Matricardi, M., McNally, A. P., Monge-Sanz, B. M., Morcrette, J.-J., Park, B.-K., Peubey, C., de Rosnay, P., Tavolato, C., Thépaut, J.-N., & Vitart, F. (2011). The ERA-Interim reanalysis: configuration and performance of the data assimilation system. *Quarterly Journal of the Royal Meteorological Society*, *137*(656), 553–597.

Ding, R., Li, J., Wang, S., & Ren, F. (????). Decadal change of the spring dust storm in

northwest China and the associated atmospheric circulation. *Geophysical Research Letters*, *32*.

Ding, Y. (1992). Summer Monsoon Rainfalls in China. *Journal of the Meteorological Society of Japan. Ser. II*, *70*(1B), 373–396.

Ding, Y., & Chan, J. C. L. (2005). The East Asian summer monsoon: an overview. *Meteorology and Atmospheric Physics*, *89*(1-4), 117–142.

Douglas, M. W., Maddox, R. A., Howard, K., & Reyes, S. (1993). The Mexican Monsoon. *Journal of Climate*, *6*(8), 1665–1677. Publisher: American Meteorological Society.

Enomoto, T., Hoskins, B. J., & Matsuda, Y. (2003). The formation mechanism of the Bonin high in August. *Quarterly Journal of the Royal Meteorological Society*, *129*(587), 157–178.

Flohn, H. (1957). Large-scale aspects of the "summer monsoon" in South and East Asia. *J. Meteor. Soc. Japan*, *75*, 180–186.

Gadgil, S. (2003). The Indian Monsoon and Its Variability. *Annual Review of Earth and Planetary Sciences*, *31*(1), 429–467. _eprint: https://doi.org/10.1146/annurev.earth.31.100901.141251.

Gan, B., Kwon, Y.-O., Joyce, T. M., Chen, K., & Wu, L. (2019). Influence of the Kuroshio Interannual Variability on the Summertime Precipitation over the East China Sea and Adjacent Area. *Journal of Climate*, *32*(8), 2185–2205.

Gan, M. A., Kousky, V. E., & Ropelewski, C. F. (2004). The South America Monsoon Circulation and Its Relationship to Rainfall over West-Central Brazil. *Journal of Climate*, *17*(1), 47–66. Publisher: American Meteorological Society.

Gent, P. R., Danabasoglu, G., Donner, L. J., Holland, M. M., Hunke, E. C., Jayne, S. R., Lawrence, D. M., Neale, R. B., Rasch, P. J., Vertenstein, M., Worley, P. H., Yang, Z.-L., & Zhang, M. (2011). The Community Climate System Model Version 4. *Journal of Climate*, *24*(19), 4973–4991.

Gill, A. E. (1980). Some simple solutions for heat-induced tropical circulation. *Quarterly Journal of the Royal Meteorological Society*, *106*(449), 447–462.

Gong, D.-Y., & Ho, C.-H. (2002). Shift in the summer rainfall over the Yangtze River valley in the late 1970s. *Geophysical Research Letters*, *29*(10), 78–1.

Gutzler, D. S. (2004). An Index of Interannual Precipitation Variability in the Core of the North American Monsoon Region. *Journal of Climate*, *17*(22), 4473–4480. Publisher: American Meteorological Society.

Hahn, D. G., & Manabe, S. (1975). The Role of Mountains in the South Asian Monsoon Circulation. *Journal of the Atmospheric Sciences*, *32*(8), 1515–1541.

Halley, E. (1687). An historical account of the trade winds, and monsoons, observable in the seas between and near the Tropicks, with an attempt to assign the physical cause of the said winds. *Philosophical Transactions of the Royal Society of London*, *16*(183), 153–168. Publisher: Royal Society.

Han, Z., & Zhou, T. (2012). Assessing the quality of APHRODITE high-resolution daily precipitation dataset over contiguous China. *Chinese Journal of Atmospheric Sciences (in Chinese)*, *36*(2), 361–373.

Hardiman, S. C., Dunstone, N. J., Scaife, A. A., Bett, P. E., Li, C., Lu, B., Ren, H.-L.,

Smith, D. M., & Stephan, C. C. (2018). The asymmetric response of Yangtze river basin summer rainfall to El Niño/La Niña. *Environmental Research Letters*, *13*(2), 024015.

He, C., Zhou, T., Lin, A., Wu, B., Gu, D., Li, C., & Zheng, B. (2015). Enhanced or Weakened Western North Pacific Subtropical High under Global Warming? *Scientific Reports*, *5*(1), 1–7. Number: 1 Publisher: Nature Publishing Group.

Held, I. M. (1983). Stationary and quasi-stationary eddies in the extratropical troposphere: Theory. Large-Scale Dynamical Processes in The Atmosphere. In *Large-Scale Dynamic Processes in the Atmosphere*, (pp. 127–168).

Held, I. M., & Suarez, M. J. (1994). A Proposal for the Intercomparison of the Dynamical Cores of Atmospheric General Circulation Models. *Bulletin of the American Meteorological Society*, *75*(10), 1825–1830.

Hong, X., & Lu, R. (2016). The Meridional Displacement of the Summer Asian Jet, Silk Road Pattern, and Tropical SST Anomalies. *Journal of Climate*, *29*(10), 3753–3766.

Hong, X., Lu, R., & Li, S. (2017). Asymmetric Relationship between the Meridional Displacement of the Asian Westerly Jet and the Silk Road Pattern. *Advances in Atmospheric Sciences*.

Hoskins, B. J., & Ambrizzi, T. (1993). Rossby Wave Propagation on a Realistic Longitudinally Varying Flow. *Journal of the Atmospheric Sciences*, *50*(12), 1661–1671.

Hoskins, B. J., & Karoly, D. J. (1981). The Steady Linear Response of a Spherical Atmosphere to Thermal and Orographic Forcing. *Journal of the Atmospheric Sciences*, *38*(6), 1179–1196.

Hsu, H.-H., & Lin, S.-M. (2007). Asymmetry of the Tripole Rainfall Pattern during the East Asian Summer. *Journal of Climate*, *20*(17), 4443–4458.

Huang, D.-Q., Zhu, J., Zhang, Y.-C., & Huang, A.-N. (2014). The Different Configurations of the East Asian Polar Front Jet and Subtropical Jet and the Associated Rainfall Anomalies over Eastern China in Summer. *Journal of Climate*, *27*(21), 8205–8220.

Huang, R., & Wu, Y. (1989). The influence of ENSO on the summer climate change in China and its mechanism. *Advances in Atmospheric Sciences*, *6*(1), 21–32.

Huffman, G. J., Bolvin, D. T., Nelkin, E., Wolff, D. B., Adler, R. F., Gu, G., Hong, Y., Bowman, K. P., & Stocker, E. F. (2007). The TRMM Multisatellite Precipitation Analysis (TMPA): Quasi-Global, Multiyear, Combined-Sensor Precipitation Estimates at Fine Scales.

Hurrell, J. W., Hack, J. J., Shea, D., Caron, J. M., & Rosinski, J. (2008). A New Sea Surface Temperature and Sea Ice Boundary Dataset for the Community Atmosphere Model. *Journal of Climate*, *21*(19), 5145–5153.

Hurrell, J. W., Holland, M. M., Gent, P. R., Ghan, S., Kay, J. E., Kushner, P. J., Lamarque, J.-F., Large, W. G., Lawrence, D., Lindsay, K., Lipscomb, W. H., Long, M. C., Mahowald, N., Marsh, D. R., Neale, R. B., Rasch, P., Vavrus, S., Vertenstein, M., Bader, D., Collins, W. D., Hack, J. J., Kiehl, J., & Marshall, S. (2013). The Community Earth System Model: A Framework for Collaborative Research. *Bulletin of the American Meteorological Society*, *94*(9), 1339–1360.

Iskandar, I. (2009). VARIABILITY OF SATELLITE-OBSERVED SEA SURFACE HEIGHT

IN THE TROPICAL INDIAN OCEAN: COMPARISON OF EOF AND SOM ANALYSIS. *MAKARA SAINS*, *13*(2), 173–179.

Janowiak, J. E. (1988). An Investigation of Interannual Rainfall Variability in Africa. *Journal of Climate*, *1*(3), 240–255. Publisher: American Meteorological Society.

Jin, L., Schneider, B., Park, W., Latif, M., Khon, V., & Zhang, X. (2014). The spatial-temporal patterns of Asian summer monsoon precipitation in response to Holocene insolation change: a model-data synthesis. *Quaternary Science Reviews*, *85*, 47–62.

Johnson, N. C. (2013). How Many ENSO Flavors Can We Distinguish?*. *Journal of Climate*, *26*(13), 4816–4827.

Johnson, N. C., Collins, D. C., Feldstein, S. B., L'Heureux, M. L., & Riddle, E. E. (2013). Skillful Wintertime North American Temperature Forecasts out to 4 Weeks Based on the State of ENSO and the MJO. *Weather and Forecasting*, *29*(1), 23–38.

Johnson, N. C., Feldstein, S. B., & Tremblay, B. (2008). The Continuum of Northern Hemisphere Teleconnection Patterns and a Description of the NAO Shift with the Use of Self-Organizing Maps. *Journal of Climate*, *21*(23), 6354–6371.

Kalnay, E., Kanamitsu, M., Kistler, R., Collins, W., Deaven, D., Gandin, L., Iredell, M., Saha, S., White, G., Woollen, J., Zhu, Y., Leetmaa, A., Reynolds, R., Chelliah, M., Ebisuzaki, W., Higgins, W., Janowiak, J., Mo, K. C., Ropelewski, C., Wang, J., Jenne, R., & Joseph, D. (1996). The NCEP/NCAR 40-Year Reanalysis Project. *Bulletin of the American Meteorological Society*, *77*(3), 437–471.

Kay, J. E., Deser, C., Phillips, A., Mai, A., Hannay, C., Strand, G., Arblaster, J. M., Bates, S. C., Danabasoglu, G., Edwards, J., Holland, M., Kushner, P., Lamarque, J.-F., Lawrence, D., Lindsay, K., Middleton, A., Munoz, E., Neale, R., Oleson, K., Polvani, L., & Vertenstein, M. (2014). The Community Earth System Model (CESM) Large Ensemble Project: A Community Resource for Studying Climate Change in the Presence of Internal Climate Variability. *Bulletin of the American Meteorological Society*, *96*(8), 1333–1349.

Kitoh, A. (2004). Effects of Mountain Uplift on East Asian Summer Climate Investigated by a Coupled Atmosphere–Ocean GCM. *Journal of Climate*, *17*(4), 783–802.

Kodama, Y. (1992). Large-Scale Common Features of Subtropical Precipitation Zones (the Baiu Frontal Zone, the SPCZ, and the SACZ) Part I: Characteristics of Subtropical Frontal Zones. *Journal of the Meteorological Society of Japan. Ser. II*, *70*(4), 813–836.

Kohonen, T. (2001). *Self-Organizing Maps*. Springer, 3rd ed.

Kohonen, T., Hynninen, J., Kangas, J., & Laaksonen, J. (1996). SOM_pak: The self-organizing maps program package. Tech. Rep. A31, Helsinki University of Technology, Faculty of Information Technology, Laboratory of Computer and Information Science.

Kong, W., & Chiang, J. C. H. (2019). Interaction of the Westerlies with the Tibetan Plateau in Determining the Mei-Yu Termination. *Journal of Climate*, *33*(1), 339–363. Publisher: American Meteorological Society.

Kong, W., & Chiang, J. C. H. (2020). Southward shift of westerlies intensifies the East Asian early summer rainband following El Niño. *Revised for Geophysical Research Letters*.

Kong, W., Swenson, L. M., & Chiang, J. C. H. (2017). Seasonal Transitions and the Westerly Jet in the Holocene East Asian Summer Monsoon. *Journal of Climate*, *30*(9), 3343–3365.

Kosaka, Y., & Nakamura, H. (2006). Structure and dynamics of the summertime Pacific–Japan teleconnection pattern. *Quarterly Journal of the Royal Meteorological Society*, *132*(619), 2009–2030.

Kosaka, Y., & Nakamura, H. (2010). Mechanisms of Meridional Teleconnection Observed between a Summer Monsoon System and a Subtropical Anticyclone. Part I: The Pacific–Japan Pattern. *Journal of Climate*, *23*(19), 5085–5108. Publisher: American Meteorological Society.

Kosaka, Y., Nakamura, H., Watanabe, M., & Kimoto, M. (2009). Analysis on the Dynamics of a Wave-like Teleconnection Pattern along the Summertime Asian Jet Based on a Reanalysis Dataset and Climate Model Simulations. . *2*, *87*(3), 561–580.

Kosaka, Y., Xie, S.-P., & Nakamura, H. (2011). Dynamics of Interannual Variability in Summer Precipitation over East Asia. *Journal of Climate*, *24*(20), 5435–5453.

Kurosaki, Y., & Mikami, M. (2003). Recent frequent dust events and their relation to surface wind in East Asia. *Geophysical Research Letters*, *30*(14), 1736.

Kuwano-Yoshida, A., Taguchi, B., & Xie, S.-P. (2013). Baiu Rainband Termination in Atmospheric and Coupled Atmosphere–Ocean Models. *Journal of Climate*, *26*(24), 10111–10124.

Kwon, M., Jhun, J.-G., & Ha, K.-J. (2007). Decadal change in east Asian summer monsoon circulation in the mid-1990s. *Geophysical Research Letters*, *34*(21), L21706.

Lau, N.-C. (1988). Variability of the Observed Midlatitude Storm Tracks in Relation to Low-Frequency Changes in the Circulation Pattern. *Journal of the Atmospheric Sciences*, *45*(19), 2718–2743.

Lauritzen, P. H., Bacmeister, J. T., Callaghan, P. F., & Taylor, M. A. (2015). NCAR global model topography generation software for unstructured grids. *Geoscientific Model Development Discussions*, *8*(6), 4623–4651.

Li, C., & Yanai, M. (1996). The Onset and Interannual Variability of the Asian Summer Monsoon in Relation to Land–Sea Thermal Contrast. *Journal of Climate*, *9*(2), 358–375.

Li, L., Lin, P., Yu, Y., Wang, B., Zhou, T., Liu, L., Liu, J., Bao, Q., Xu, S., Huang, W., , K. X. , Y. P. , L. D. , S. S. , Y. L., , N. H. , M. L., , W. S., , X. S., , W. Z., , B. W. , M. S., , H. L., , X. Z., , G. W., , W. X. , X. H., , G. Y., , Z. S., & , F. Q. (2013). The flexible global ocean-atmosphere-land system model, Grid-point Version 2: FGOALS-g2. *Advances in Atmospheric Sciences*, *30*(3), 543–560.

Li, L., & Zhang, Y. (2014). Effects of Different Configurations of the East Asian Subtropical and Polar Front Jets on Precipitation during the Mei-Yu Season. *Journal of Climate*, *27*(17), 6660–6672.

Li, X., & Lu, R. (2017). Extratropical Factors Affecting the Variability in Summer Precipitation over the Yangtze River Basin, China. *Journal of Climate*, *30*(20), 8357–8374.

Liang, X.-Z., & Wang, W.-C. (1998). Associations between China monsoon rainfall and tropospheric jets. *Quarterly Journal of the Royal Meteorological Society*, *124*(552), 2597–2623.

Lin, G.-F., & Chen, L.-H. (2006). Identification of homogeneous regions for regional frequency analysis using the self-organizing map. *Journal of Hydrology*, *324*(1–4), 1–9.

Liu, Y., Hoskins, B., & Blackburn, M. (2007). Impact of Tibetan Orography and Heating on the Summer Flow over Asia. . *2*, *85B*, 1–19.

Liu, Y., Weisberg, R. H., & Mooers, C. N. K. (2006). Performance evaluation of the self-organizing map for feature extraction. *Journal of Geophysical Research: Oceans*, *111*(C5), C05018.

Lutsko, N. J., & Held, I. M. (2016). The Response of an Idealized Atmosphere to Orographic Forcing: Zonal versus Meridional Propagation. *Journal of the Atmospheric Sciences*, *73*(9), 3701–3718.

Maher, B. A. (2008). Holocene variability of the East Asian summer monsoon from Chinese cave records: a re-assessment. *The Holocene; London*, *18*(6), 861–866. Num Pages: 6 Place: London, United Kingdom, London Publisher: Sage Publications Ltd.

Manabe, S., & Terpstra, T. B. (1974). The Effects of Mountains on the General Circulation of the Atmosphere as Identified by Numerical Experiments. *Journal of the Atmospheric Sciences*, *31*(1), 3–42.

McHugh, M. J. (2004). Near-Surface Zonal Flow and East African Precipitation Receipt during Austral Summer. *Journal of Climate*, *17*(20), 4070–4079. Publisher: American Meteorological Society.

Miyasaka, T., & Nakamura, H. (2005). Structure and Formation Mechanisms of the Northern Hemisphere Summertime Subtropical Highs. *Journal of Climate*, *18*(23), 5046–5065. Publisher: American Meteorological Society.

Molnar, P., Boos, W. R., & Battisti, D. S. (2010). Orographic Controls on Climate and Paleoclimate of Asia: Thermal and Mechanical Roles for the Tibetan Plateau. *Annual Review of Earth and Planetary Sciences*, *38*(1), 77–102.

Murakami, T. (1951). On the Study of the Change of the Upper Westerlies in the Last Stage of Baiu Season (Rainy Season in Japan). *Journal of the Meteorological Society of Japan. Ser. II*, *29*(5), 162–175.

Nagashima, K., Tada, R., Tani, A., Sun, Y., Isozaki, Y., Toyoda, S., & Hasegawa, H. (2011). Millennial-scale oscillations of the westerly jet path during the last glacial period. *Journal of Asian Earth Sciences*, *40*(6), 1214–1220.

Nagashima, K., Tada, R., & Toyoda, S. (2013). Westerly jet-East Asian summer monsoon connection during the Holocene: WESTERLY JET-ASIAN MONSOON CONNECTION. *Geochemistry, Geophysics, Geosystems*, (pp. n/a–n/a).

Neale, R. B., Gettelman, A., Park, S., Conley, A. J., Kinnison, D., Marsh, D., Smith, A. K., Vitt, F., Morrison, H., Cameron-smith, P., Collins, W. D., Iacono, M. J., Easter, R. C., Liu, X., Taylor, M. A., Chen, C.-c., Lauritzen, P. H., Williamson, D. L., Garcia, R., Lamarque, J.-f., Mills, M., Tilmes, S., Ghan, S. J., Rasch, P. J., & Meteorology, M. (2010). Description of the NCAR Community Atmosphere Model (CAM 5.0), Tech. Note NCAR/TN-486+STR, Natl. Cent. for Atmos. In *6of7 ZHAO ET AL.: AEROSOL FIE SIMULATED BY CAMS L08806*, (pp. 2009–038451).

Nie, J., & Fan, B. (2019). Roles of Dynamic Forcings and Diabatic Heating in Summer Extreme Precipitation in East China and the Southeastern United States. *Journal of Climate*, *32*(18), 5815–5831. Publisher: American Meteorological Society.

Ninomiya, K. (1984). Characteristics of Baiu front as a predominant subtropical front in the summer northern hemisphere. *Journal of the Meteorological Society of Japan*, *62*(6), 880–894.

Ninomiya, K. (2000). Large- and Meso--scale Characteristics of Meiyu/Baiu Front Associated with Intense Rainfalls in 1-10 July 1991. *Journal of the Meteorological Society of Japan. Ser. II*, *78*(2), 141–157.

Ninomiya, K., & Shibagaki, Y. (2007). Multi-Scale Features of the Meiyu-Baiu Front and Associated Precipitation Systems. *Journal of the Meteorological Society of Japan. Ser. II*, *85B*, 103–122.

Nitta, T. (1987). Convective activities in the tropical western Pacific and their impact on the northern hemisphere summer circulation. *Journal of the Meteorological Society of Japan*, *65*(3), 373–390.

Otto-Bliesner, B. L., Brady, E. C., Fasullo, J., Jahn, A., Landrum, L., Stevenson, S., Rosenbloom, N., Mai, A., & Strand, G. (2015). Climate Variability and Change since 850 CE: An Ensemble Approach with the Community Earth System Model. *Bulletin of the American Meteorological Society*, *97*(5), 735–754.

Park, H.-S., Chiang, J. C. H., & Bordoni, S. (2012). The Mechanical Impact of the Tibetan Plateau on the Seasonal Evolution of the South Asian Monsoon. *Journal of Climate*, *25*(7), 2394–2407.

Park, H.-S., Lintner, B. R., Boos, W. R., & Seo, K.-H. (2015). The Effect of Midlatitude Transient Eddies on Monsoonal Southerlies over Eastern China. *Journal of Climate*, *28*(21), 8450–8465.

Pausata, F. S. R., Battisti, D. S., Nisancioglu, K. H., & Bitz, C. M. (2011). Chinese stalagmite 18O controlled by changes in the Indian monsoon during a simulated Heinrich event. *Nature Geoscience*, *4*(7), 474–480.

Peltier, W. (2004). GLOBAL GLACIAL ISOSTASY AND THE SURFACE OF THE ICE-AGE EARTH: The ICE-5G (VM2) Model and GRACE. *Annual Review of Earth and Planetary Sciences*, *32*(1), 111–149. Publisher: Annual Reviews.

Plumb, R. A. (1985). On the Three-Dimensional Propagation of Stationary Waves. *Journal of the Atmospheric Sciences*, *42*(3), 217–229.

Privé, N. C., & Plumb, R. A. (2007). Monsoon Dynamics with Interactive Forcing. Part II: Impact of Eddies and Asymmetric Geometries. *Journal of the Atmospheric Sciences*, *64*(5), 1431–1442. Publisher: American Meteorological Society.

Rayner, N. A., Parker, D. E., Horton, E. B., Folland, C. K., Alexander, L. V., Rowell, D. P., Kent, E. C., & Kaplan, A. (2003). Global analyses of sea surface temperature, sea ice, and night marine air temperature since the late nineteenth century. *Journal of Geophysical Research: Atmospheres*, *108*(D14).

Ringler, T. D., & Cook, K. H. (1997). Factors Controlling Nonlinearity in Mechanically Forced Stationary Waves over Orography. *Journal of the Atmospheric Sciences*, *54*(22), 2612–2629. Publisher: American Meteorological Society.

Rodwell, M. J., & Hoskins, B. J. (2001). Subtropical Anticyclones and Summer Monsoons. *Journal of Climate*, *14*(15), 3192–3211.

Roe, G. (2009). On the interpretation of Chinese loess as a paleoclimate indicator. *Quaternary Research*, *71*(2), 150–161.

Sampe, T., & Xie, S.-P. (2010). Large-Scale Dynamics of the Meiyu-Baiu Rainband: Environmental Forcing by the Westerly Jet*. *Journal of Climate*, *23*(1), 113–134.

Schiemann, R., Lüthi, D., & Schär, C. (2009). Seasonality and Interannual Variability of the Westerly Jet in the Tibetan Plateau Region*. *Journal of Climate*, *22*(11), 2940–2957.

Seager, R., Harnik, N., Kushnir, Y., Robinson, W., & Miller, J. (2003). Mechanisms of Hemispherically Symmetric Climate Variability. *Journal of Climate*, *16*(18), 2960–2978.

Seager, R., & Henderson, N. (2013). Diagnostic Computation of Moisture Budgets in the ERA-Interim Reanalysis with Reference to Analysis of CMIP-Archived Atmospheric Model Data. *Journal of Climate*, *26*(20), 7876–7901.

Seo, K.-H., Son, J.-H., Lee, J.-Y., & Park, H.-S. (2015). Northern East Asian Monsoon Precipitation Revealed by Airmass Variability and Its Prediction. *Journal of Climate*, *28*(15), 6221–6233.

Shaw, T. A., & Pauluis, O. (2012). Tropical and Subtropical Meridional Latent Heat Transports by Disturbances to the Zonal Mean and Their Role in the General Circulation. *Journal of the Atmospheric Sciences*, *69*(6), 1872–1889.

Shen, S., & Lau, K.-M. (1995). Biennial Oscillation Associated with the East Asian Summer Monsoon and Tropical Sea Surface Temperatures. *Journal of the Meteorological Society of Japan. Ser. II*, *73*(1), 105–124.

Shi, Z. (2016). Response of Asian summer monsoon duration to orbital forcing under glacial and interglacial conditions: Implication for precipitation variability in geological records. *Quaternary Science Reviews*, *139*, 30–42.

Solidoro, C., Bandelj, V., Barbieri, P., Cossarini, G., & Fonda Umani, S. (2007). Understanding dynamic of biogeochemical properties in the northern Adriatic Sea by using self-organizing maps and k-means clustering. *Journal of Geophysical Research: Oceans*, *112*(C7), C07S90.

Son, J.-H., Seo, K.-H., & Wang, B. (2019). Dynamical Control of the Tibetan Plateau on the East Asian Summer Monsoon. *Geophysical Research Letters*, *0*(0).

Son, S.-W., Lee, S., Feldstein, S. B., & Ten Hoeve, J. E. (2008). Time Scale and Feedback of Zonal-Mean-Flow Variability. *Journal of the Atmospheric Sciences*, *65*(3), 935–952. Publisher: American Meteorological Society.

Staff Members of the Section of Synoptic and Dynamic Meteorology, P. I. o. G. a. M., Academia Sinica (1957). On the General Circulation over Eastern Asia (I). *Tellus*, *9*(4), 432–446.

Staff Members of the Section of Synoptic and Dynamic Meteorology, P. I. o. G. a. M., Academia Sinica (1958a). On the General Circulation over Eastern Asia (II). *Tellus*, *10*(1), 58–75.

Staff Members of the Section of Synoptic and Dynamic Meteorology, P. I. o. G. a. M., Academia Sinica (1958b). On the General Circulation over Eastern Asia (III). *Tellus*, *10*(3), 299–312.

Stroeven, A. P., Hättestrand, C., Kleman, J., Heyman, J., Fabel, D., Fredin, O., Goodfellow,

B. W., Harbor, J. M., Jansen, J. D., Olsen, L., Caffee, M. W., Fink, D., Lundqvist, J., Rosqvist, G. C., Strömberg, B., & Jansson, K. N. (2016). Deglaciation of Fennoscandia. *Quaternary Science Reviews*, *147*, 91–121.

Stuecker, M. F., Jin, F.-F., Timmermann, A., & McGregor, S. (2014). Combination Mode Dynamics of the Anomalous Northwest Pacific Anticyclone. *Journal of Climate*, *28*(3), 1093–1111.

Stuecker, M. F., Timmermann, A., Jin, F.-F., McGregor, S., & Ren, H.-L. (2013). A combination mode of the annual cycle and the El Niño/Southern Oscillation. *Nature Geoscience*, *6*(7), 540–544.

Suzuki, S.-i., & Hoskins, B. (2009). The large-scale circulation change at the end of the Baiu season in Japan as seen in ERA40 data.

Takahashi, K., & Battisti, D. S. (2007). Processes Controlling the Mean Tropical Pacific Precipitation Pattern. Part II: The SPCZ and the Southeast Pacific Dry Zone. *Journal of Climate*, *20*(23), 5696–5706.

Takahashi, K., Montecinos, A., Goubanova, K., & Dewitte, B. (2011). ENSO regimes: Reinterpreting the canonical and Modoki El Niño. *Geophysical Research Letters*, *38*(10). _eprint: https://agupubs.onlinelibrary.wiley.com/doi/pdf/10.1029/2011GL047364.

Tang, H., Micheels, A., Eronen, J. T., Ahrens, B., & Fortelius, M. (2013). Asynchronous responses of East Asian and Indian summer monsoons to mountain uplift shown by regional climate modelling experiments. *Climate Dynamics*, *40*(5), 1531–1549.

Tao, S., & Chen, L. (1987). A review of recent research on the East Asian summer monsoon in China. In *C.-P. Chang and T. N. Krishnamurti (eds): Monsoon Meteorology*, (pp. 60–92). London: Oxford University Press.

Tardif, R., Hakim, G. J., Perkins, W. A., Horlick, K. A., Erb, M. P., Emile-Geay, J., Anderson, D. M., Steig, E. J., & Noone, D. (2019). Last Millennium Reanalysis with an expanded proxy database and seasonal proxy modeling. *Climate of the Past*, *15*(4), 1251–1273. Publisher: Copernicus GmbH.

Taylor, K. E., Stouffer, R. J., & Meehl, G. A. (2011). An Overview of CMIP5 and the Experiment Design. *Bulletin of the American Meteorological Society*, *93*(4), 485–498. Publisher: American Meteorological Society.

Thompson, D. W. J., & Birner, T. (2012). On the Linkages between the Tropospheric Isentropic Slope and Eddy Fluxes of Heat during Northern Hemisphere Winter. *Journal of the Atmospheric Sciences*, *69*(6), 1811–1823.

Ting, M. (1994). Maintenance of Northern Summer Stationary Waves in a GCM. *Journal of the Atmospheric Sciences*, *51*(22), 3286–3308.

Tomita, T., Yamaura, T., & Hashimoto, T. (2011). Interannual Variability of the Baiu Season near Japan Evaluated from the Equivalent Potential Temperature. *Journal of the Meteorological Society of Japan. Ser. II*, *89*(5), 517–537.

Vertenstein, M., Craig, T., Middleton, A., Feddema, D., & Fischer, C. (2011). CESM1.0.4 User's Guide.

Wang, B., Bao, Q., Hoskins, B. J., & Liu, Y. (2008a). Tibetan Plateau warming and precipitation changes in East Asia. *Geophysical Research Letters*, *35*(14).

Wang, B., & Ding, Q. (2008). Global monsoon: Dominant mode of annual variation in the tropics. *Dynamics of Atmospheres and Oceans*, *44*(3), 165–183.

Wang, B., & Fan, Z. (1999). Choice of South Asian Summer Monsoon Indices. *Bulletin of the American Meteorological Society*, *80*(4), 629–638. Publisher: American Meteorological Society.

Wang, B., & LinHo (2002). Rainy Season of the Asian–Pacific Summer Monsoon*. *Journal of Climate*, *15*(4), 386–398.

Wang, B., Wu, R., & Fu, X. (2000). Pacific–East Asian Teleconnection: How Does ENSO Affect East Asian Climate? *Journal of Climate*, *13*(9), 1517–1536. Publisher: American Meteorological Society.

Wang, B., Xiang, B., & Lee, J.-Y. (2013). Subtropical High predictability establishes a promising way for monsoon and tropical storm predictions. *Proceedings of the National Academy of Sciences*, *110*(8), 2718–2722. Publisher: National Academy of Sciences Section: Physical Sciences.

Wang, B., & Zhang, Q. (2002). Pacific–East Asian Teleconnection. Part II: How the Philippine Sea Anomalous Anticyclone is Established during El Niño Development. *Journal of Climate*, *15*(22), 3252–3265.

Wang, L., Xu, P., Chen, W., & Liu, Y. (2017). Interdecadal Variations of the Silk Road Pattern. *Journal of Climate*, *30*(24), 9915–9932. Publisher: American Meteorological Society.

Wang, P. K., Lin, K.-H. E., Liao, Y.-C., Liao, H.-M., Lin, Y.-S., Hsu, C.-T., Hsu, S.-M., Wan, C.-W., Lee, S.-Y., Fan, I.-C., Tan, P.-H., & Ting, T.-T. (2018). Construction of the REACHES climate database based on historical documents of China. *Scientific Data*, *5*(1), 180288. Number: 1 Publisher: Nature Publishing Group.

Wang, S., & Zuo, H. (2016). Effect of the East Asian Westerly Jet's Intensity on Summer Rainfall in the Yangtze River Valley and Its Mechanism. *Journal of Climate*, *29*(7), 2395–2406.

Wang, X., Wang, D., Zhou, W., & Li, C. (2012). Interdecadal modulation of the influence of La Niña events on mei-yu rainfall over the Yangtze River valley. *Advances in Atmospheric Sciences*, *29*(1), 157–168.

Wang, Y., Cheng, H., Edwards, R. L., He, Y., Kong, X., An, Z., Wu, J., Kelly, M. J., Dykoski, C. A., & Li, X. (2005). The Holocene Asian Monsoon: Links to Solar Changes and North Atlantic Climate. *Science*, *308*(5723), 854–857.

Wang, Y., Cheng, H., Edwards, R. L., Kong, X., Shao, X., Chen, S., Wu, J., Jiang, X., Wang, X., & An, Z. (2008b). Millennial- and orbital-scale changes in the East Asian monsoon over the past 224,000 years. *Nature*, *451*(7182), 1090–1093.

Wang, Y. J., Cheng, H., Edwards, R. L., An, Z. S., Wu, J. Y., Shen, C.-C., & Dorale, J. A. (2001). A High-Resolution Absolute-Dated Late Pleistocene Monsoon Record from Hulu Cave, China. *Science*, *294*(5550), 2345–2348.

Webster, P. J., Magaña, V. O., Palmer, T. N., Shukla, J., Tomas, R. A., Yanai, M., & Yasunari, T. (1998). Monsoons: Processes, predictability, and the prospects for prediction. *Journal of Geophysical Research: Oceans*, *103*(C7), 14451–14510. _eprint:

https://agupubs.onlinelibrary.wiley.com/doi/pdf/10.1029/97JC02719.

Wiel, K. v. d., Matthews, A. J., Stevens, D. P., & Joshi, M. M. (2015). A dynamical framework for the origin of the diagonal South Pacific and South Atlantic Convergence Zones. *Quarterly Journal of the Royal Meteorological Society*, *141*(691), 1997–2010. _eprint: https://rmets.onlinelibrary.wiley.com/doi/pdf/10.1002/qj.2508.

Wong, K. C., Liu, S., Turner, A. G., & Schiemann, R. K. (2018). Different Asian Monsoon Rainfall Responses to Idealized Orography Sensitivity Experiments in the HadGEM3-GA6 and FGOALS-FAMIL Global Climate Models. *Advances in Atmospheric Sciences*, *35*(8), 1049–1062.

Wu, G., Liu, Y., He, B., Bao, Q., Duan, A., & Jin, F.-F. (2012). Thermal Controls on the Asian Summer Monsoon. *Scientific Reports*, *2*, 404.

Wu, G., Liu, Y., Zhang, Q., Duan, A., Wang, T., Wan, R., Liu, X., Li, W., Wang, Z., & Liang, X. (2007). The Influence of Mechanical and Thermal Forcing by the Tibetan Plateau on Asian Climate. *Journal of Hydrometeorology*, *8*(4), 770–789.

Wu, T., Li, W., Ji, J., Xin, X., Li, L., Wang, Z., Zhang, Y., Li, J., Zhang, F., Wei, M., Shi, X., Wu, F., Zhang, L., Chu, M., Jie, W., Liu, Y., Wang, F., Liu, X., Li, Q., Dong, M., Liang, X., Gao, Y., & Zhang, J. (2013). Global carbon budgets simulated by the Beijing Climate Center Climate System Model for the last century. *Journal of Geophysical Research: Atmospheres*, *118*(10), 4326–4347.

Xie, P., & Arkin, P. A. (1997). Global Precipitation: A 17-Year Monthly Analysis Based on Gauge Observations, Satellite Estimates, and Numerical Model Outputs. *Bulletin of the American Meteorological Society*, *78*(11), 2539–2558.

Xie, S.-P., Hu, K., Hafner, J., Tokinaga, H., Du, Y., Huang, G., & Sampe, T. (2009). Indian Ocean Capacitor Effect on Indo–Western Pacific Climate during the Summer following El Niño. *Journal of Climate*, *22*(3), 730–747.

Xie, Z., Du, Y., & Yang, S. (2015). Zonal Extension and Retraction of the Subtropical Westerly Jet Stream and Evolution of Precipitation over East Asia and the Western Pacific. *Journal of Climate*, *28*(17), 6783–6798.

Xu, W., & Zipser, E. J. (2010). Diurnal Variations of Precipitation, Deep Convection, and Lightning over and East of the Eastern Tibetan Plateau. *Journal of Climate*, *24*(2), 448–465.

Yanai, M., & Wu, G.-X. (2006). Effects of the Tibetan Plateau. In *The Asian Monsoon*, Springer Praxis Books, (pp. 513–549). Springer, Berlin, Heidelberg.

Yang, J., Liu, Q., Xie, S.-P., Liu, Z., & Wu, L. (2007). Impact of the Indian Ocean SST basin mode on the Asian summer monsoon. *Geophysical Research Letters*, *34*(2).

Yatagai, A., Arakawa, O., Kamiguchi, K., Kawamoto, H., Nodzu, M. I., & Hamada, A. (2009). A 44-Year Daily Gridded Precipitation Dataset for Asia Based on a Dense Network of Rain Gauges. *Sola*, *5*, 137–140.

Yatagai, A., Kamiguchi, K., Arakawa, O., Hamada, A., Yasutomi, N., & Kitoh, A. (2012). APHRODITE: Constructing a Long-Term Daily Gridded Precipitation Dataset for Asia Based on a Dense Network of Rain Gauges. *Bulletin of the American Meteorological Society*, *93*(9), 1401–1415.

Yeh, T. C., Dao, S. Y., & Li, M. T. (1959). The abrupt change of circulation over the Northern Hemisphere during June and October. In *The Atmosphere and the Sea in Motion*, (pp. 249–267). Rockefeller Institute Press.

Zhang, G. J., & McFarlane, N. A. (1995). Sensitivity of climate simulations to the parameterization of cumulus convection in the Canadian climate centre general circulation model. *Atmosphere-Ocean*, *33*(3), 407–446.

Zhang, R., Jiang, D., Liu, X., & Tian, Z. (2012). Modeling the climate effects of different subregional uplifts within the Himalaya-Tibetan Plateau on Asian summer monsoon evolution. *Chinese Science Bulletin*, *57*(35), 4617–4626.

Zhang, W., Jin, F.-F., Stuecker, M. F., Wittenberg, A. T., Timmermann, A., Ren, H.-L., Kug, J.-S., Cai, W., & Cane, M. (2016). Unraveling El Niño's impact on the East Asian Monsoon and Yangtze River summer flooding. *Geophysical Research Letters*, *43*(21), 2016GL071190.

Zhang, W., Li, H., Stuecker, M. F., Jin, F.-F., & Turner, A. G. (2015). A New Understanding of El Niño's Impact over East Asia: Dominance of the ENSO Combination Mode. *Journal of Climate*, *29*(12), 4347–4359.

Zhang, Y., Renssen, H., Seppä, H., Valdes, P. J., & Li, J. (2020). Spatial contrasts of the Holocene hydroclimate trend between North and East Asia. *Quaternary Science Reviews*, *227*, 106036.

Zheng, W., Wu, B., He, J., & Yu, Y. (2013). The East Asian Summer Monsoon at mid-Holocene: results from PMIP3 simulations. *Clim. Past*, *9*(1), 453–466.

Zhou, W., Xie, S.-P., & Yang, D. (2019). Enhanced equatorial warming causes deep-tropical contraction and subtropical monsoon shift. *Nature Climate Change*, *9*(11), 834–839.

Zhu, Y., Wang, H., Zhou, W., & Ma, J. (2011). Recent changes in the summer precipitation pattern in East China and the background circulation. *Climate Dynamics*, *36*(7-8), 1463–1473.